RICE UNIVERSITY

Magnetic Control in Crystal Growth from a Melt

by

Yue Huang

A Thesis Submitted
in Partial Fulfillment of the
Requirements for the Degree

Doctor of Philosophy

Approved, Thesis Committee:

Brent C. Houchens, Chair
Assistant Professor of Mechanical
Engineering and Materials Science

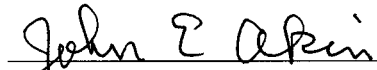

John E. Akin
Professor of Mechanical Engineering and
Materials Science

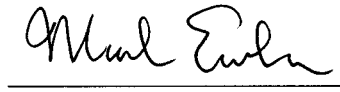

Mark P. Embree
Professor of Computational and Applied
Mathematics

Houston, Texas

March, 2012

ABSTRACT

Magnetic Control in Crystal Growth from a Melt

by

Yue Huang

Control of bulk melt crystal growth techniques is desirable for producing semiconductors with the highest purity and ternary alloys with tunable electrical properties. Because these molten materials are electrically conducting, external magnetic fields are often employed to regulate the flow in the melt. However, complicated by the coupled flow, thermal, electromagnetic and chemical physics, such magnetic control is typically empirical or even an educated guess. Two magnetic flow control mechanisms: flow damping by steady magnetic fields, and flow stirring by alternating magnetic fields, are investigated numerically.

Magnetic damping during optically-heated float-zone crystal growth is modeled using a spectral collocation method. The Marangoni convection at the free melt-gas interface is suppressed when exposed to a steady axial magnetic field, measured by the Hartmann number Ha. As a result, detrimental flow instabilities are suppressed, and an almost quiescent region forms in the interior, ideal for single crystal growth. Using normal mode linear stability analyses, dominant flow instabilities are determined in a range applicable to experiments (up to $Ha = 300$ for $Pr = 0.02$, and up to $Ha = 500$ for $Pr = 0.001$). The hydrodynamic nature of the instability for small Prandtl number Pr liquid bridges is confirmed by energy analyses.

Magnetic stirring is modeled for melt crystal growth in an ampule exposed to a

transverse rotating magnetic field. Decoupled from the flow field at small magnetic Reynolds number, the electromagnetic field is first solved via finite element analysis. The flow field is then solved using the spectral element method. At low to moderate AC frequencies (up to a few kHz), the electromagnetic body force is dominant in the azimuthal direction, which stirs a steady axisymmetric flow primarily in the azimuthal direction. A weaker secondary flow develops in the meridional plane. However, at high AC frequencies (on the order of 10 kHz and higher), only the flow within a skin depth is directly stirred due to the magnetic shielding effect.

By regulating the flow in the melt, magnetic control can improve grown-crystal properties in new materials, and achieve economically viable growth rates for production of novel crystalline semiconductors.

Acknowledgments

This dissertation would not have been possible without the close guidance from my doctoral advisor and dissertation committee chair, Professor Brent C. Houchens. I would like to express my sincerest appreciation for his excellent mentoring for my graduate study at Rice University, his inspiring advice on my research and his continuous support for my career advancement.

My genuine gratitude also goes to the other dissertation committee members, Professor John E. Akin and Professor Mark P. Embree for their insightful suggestions on my work and their invaluable lectures.

I feel grateful to have worked in a group with exceptional individuals. Kenneth E. Davis provided me with innumerable help through his impressive work. I have always been supported and encouraged by other group members including Han Li, Dr. Paul M. Boyle, Stephanie E. Tritchler, Zhao (Chad) Kong and Andres J. Goza.

I would like to thank the Department of Mechanical Engineering & Materials Science at Rice University for assisting my graduate study and research throughout. I appreciate the U.S. Air Force Office of Scientific Research for providing research funding. I would also like to acknowledge support from the Nettie S. Autrey Graduate Fellowship and the National Science Foundation for a travel grant to attend the 5^{th} Conference of the International Marangoni Association.

Finally, I owe my deepest gratitude to my parents, Shangwen Huang and Qian Liao, for their unconditional support and encouragement for my study and life.

Contents

Chapter 1

Crystal Growth Overview

Processed by humans as early as 1500BC in crystallization of salt and sugar, crystals, particularly semiconductors, remain essential elements to many modern technologies. For example, the rapid advancing information technology industry is based on silicon, which is cost-effective and scalable in production, and abundant in the Earth's crust. Transistors made from gallium arsenide (GaAs) function at radio-frequency, allowing applications such as microwave frequency integrated circuits, monolithic microwave integrated circuits, infrared light-emitting diodes, laser diodes, solar cells and optical windows. Cadmium mercury telluride (HgCdTe) is the only common material that detects infrared radiation in both of the accessible atmospheric windows, and is extensively used for night vision in military technology. Inorganic crystal scintillators, such as alkali metal halides with activator dopants, are used as detectors in high-energy particle physics experiments, security applications and medical imaging [Capper, 2005].

Crystal growth is the crystallization process of "arranging atoms, ions, molecules or molecular assemblies into regular three-dimensional periodic arrays" [Dhanaraj et al., 2010]. Deficiencies generated during crystal growth greatly affect structural, chemical, electronic and scattering properties of single crystals. These defects range from atomic-size vacancies, interstitial impurity atoms (or dopants, introduced intentionally), one-dimensional dislocations, two-dimensional defects such as grain boundaries, to three-dimensional defects such as second-phases and inclusions. The adverse effects on device quality of selected defects in melt-grown crystals are summarized in Section 6.1

of [Dhanaraj et al., 2010].

Therefore, one primary goal of crystal growers is often to minimize defects and to enhance homogeneities. Thus a variety of crystal growth methods have been developed taking into account chemical, thermodynamic, kinetic and economic considerations. Several methods are summarized in Table 1.1.

In addition, the advancement of space technology offers the crystal growth community the opportunity to explore new growth conditions in microgravity. Intrinsic physics under terrestrial conditions such as natural convection, hydrostatic pressure and sedimentation are absent, resulting in different flow dynamics during growth from melt, solution and vapor. For example, the free surface of an optically-heated float-zone melt is of barrel shape in microgravity, but sags down under terrestrial conditions (Figure 1.1). According to [Capper, 2005], "the very first [microgravity crystal growth] experiments were performed during the 3^{rd} and 4^{th} Skylab missions operated by NASA in 1973 and 1974... About one hundred and fifty bulk crystal-growth experiments have been performed under microgravity conditions [as of 2005]." Among them, Chapter 17 of Capper's book lists all well-documented microgravity experiments categorized under the Bridgman method, float-zone method, growth from solution, and growth from vapor.

1.1 Melt Growth Techniques

This work primarily focuses on *crystal growth from a melt*, also referred to as *melt growth* methods. These are among the most popular crystal growth methods due to their relatively high growth rates, earning them the term *bulk growth*, especially as compared to slow vapor growth methods. Bulk growth methods produce the most economically viable crystals, allowing the technology associated with the specialized

Table 1.1 : Classification of crystal growth processes with examples of processes listed in *italics*. Thermal and mechanical inputs are listed above and below the arrows, respectively, when required [Byrappa and Pushcharovsky, 1992]; reprinted with permission.

Method	Input(s)		Output(s)
1. Solid → Solid	Solid	$\xrightarrow[\text{deformation}]{\text{heating}}$	Solid
	Devitrification, Strain annealing, Polymorphic phase change,		
	Precipitation from solid solution		
2. Liquid → Solid			
(i) Melt growth	Molten material	$\xrightarrow{\text{cooling}}$	Crystal
	Bridgman-Stockbarger, Kyropoulos,Czochralski, Zoning, Verneuil		
(ii) Flux growth	Solid(s) + Flux Agent(s)	$\xrightarrow{\text{cooling}}$	Crystal(s)
(iii) Solution growth	Solid(s) + Solvent	$\xrightarrow{T<T_{melt}}$	Crystal(s)
	Evaporation, Slow cooling, Boiling solutions		
(iv) Hydrothermal	Solid(s) + Solvents	$\xrightarrow[\text{high P}]{\text{high T}}$	Crystal(s)
growth	*Hydrothermal sintering, Hydrothermal reactions,*		
	Normal temperature gradient, Reversed temperature gradient		
(v) Gel growth	Solution + Gel medium	$\xrightarrow{T<T_{melt}}$	Crystal
	Reaction, Complex decomplex, Chemical reduction,		
	Solubility reduction, Counter-flow diffusion		
3. Gas → Solid	Vapor(s)	→	Solid
	Sublimation-condensation, Sputtering, Epitaxial processes,		
	Ion-implantation		

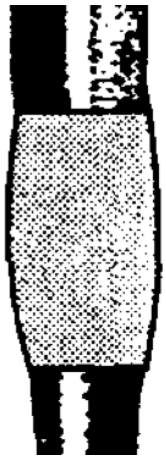

(a) Barrel shape in microgravity (depicted from experiment video)

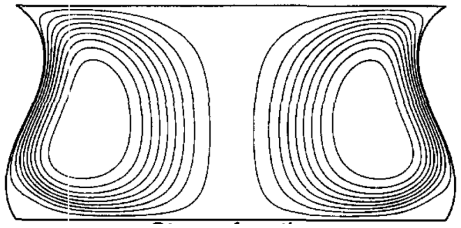

(b) Sagging in $1g$ (numerical simulation, with stream function contours on the cross-sectional plane)

Figure 1.1 : Free surface shapes of float-zone in microgravity [Martinez and Eyer, 1986] and $1g$ [Shyy and Rao, 1995], respectively; reprinted with permission.

material properties to transfer to industrial and consumer products. Bulk melt growth methods involve a controlled phase change from liquid to solid at the melting point or solidus of the material. Melt growth "requires that the material melts without decomposition, has no polymorphic transitions, and exhibits low chemical activity" [Dhanaraj et al., 2010]. Melt growth is often used to obtain elemental semiconductors and metals, oxides, halides, chalcogenides, *etc.* at relatively high growth rates. Alloy semiconductors are often more difficult to grow from a melt due to segregation and buoyancy, be it thermally or compositionally driven.

It is worth to mention that, although not the focus of this work, the *Czochralski*

technique[1] is the dominant melt crystal growth technique in commercial production of a wide range of compound semiconductors, metals, oxides and halides. In Czochralski growth the material is melted in a crucible. A seed crystal is dipped into the melt, then slowly lifted from the melt free surface, allowing single-crystallization onto the seed, with predetermined orientation. The lifting rates (from a few tenths of a millimeter per hour to tens of centimeters per hour) vary among materials and the grown crystal size. Grown crystals with diameters up to 30 mm are common. The Czochralski technique is popular in bulk crystal growth due to its high production rate, large volume of grown crystals, *etc.*, and absence of disadvantages inherent in alternative melt growth techniques. For example, during Czochralski growth the crystal grower is able to see the growth process within the chamber. Also, because the grown crystal rod does not contact the crucible during the cooling process after the growth, the thermal stresses (due to different thermal expansion rates of the crystal and the crucible) are minimized. Interested readers are referred to books such as [Davis, 1993, Capper, 2005] for detailed discussions about the Czochralski technique.

1.1.1 Float-zone Crystal Growth

During *float-zone crystal growth processes* (also referred to as *floating zone*), the molten material does not touch any container surface. Therefore float-zone growth is used to produce crystals with the highest purity and minimum cracks due to thermal strain induced during cooling.[2] In floating zone processes the feed material is heated above its melting point, forming a molten zone (the *float-zone* or the *liquid bridge* in

[1] named after the Polish chemist, *Jan Czochralski* (1885 - 1953).

[2] In the most common bulk crystal growth techniques, such as *Bridgman* and *Czochralski*, molten crystal materials are contained in crucibles or ampules and are processed in furnaces above the melting temperatures of the constituents. At such high temperatures, small amount of material from

Section 3.1). A free surface is maintained such that the melt does not come into contact with any container. By pulling at a very slow rate, the melt then re-solidifies, in theory, into a single crystal at the liquid-solid interface (the crystallization front) of the grown crystal. Float-zone processes are often conducted in an inert gas environment to avoid unwanted oxidation from the atmosphere, as the melting point of the material typically ranges from 500°C to over 1000°C.

Two heating methods are commonly used in float-zone crystal growth processes. The most common type of float-zone growth is via radio frequency (RF) induced heating from an external coil. In RF float-zone the melt region is severely necked down[3] and the free surface is held in place by a combination of surface tension and electromagnetic body forces. Figure 1.2 shows an experimental setup of RF float-zone [Dold, 2004]. Feed material is passed through a ring-shaped coil in which a strong radio-frequency alternating electric current runs (for example, the experiment in Figure 1.2 was powered by a 600kHz generator). A strong eddy current is induced within the crystal rod. This eddy current generates excessive heat, which melts the local crystal sample, and subsequently develops a liquid bridge. For a comparison between the radiation-heated and RF-heated float-zone crystal growth processes, refer to [Dold, 2004].

Here the focus is on a second float-zone method, the optically-heated float-zone. As Figure 1.3 shows, in an optically-heated float-zone, a polycrystalline feed rod is processed through an optical furnace. Here a double-ellipsoidal mirror furnace is

---

the container are inevitably dissolved into the melt as contaminants. For example, oxygen is a typical and often unwanted contaminant resulting in growth in an ampule. Furthermore, due to the different thermal expansion coefficients of the grown crystal and the ampule, stress induced cracks are difficult to avoid when crystal ingots in ampules are cooled to room temperature.

[3] Some literature refers to this method as the *needle-eye technique.*

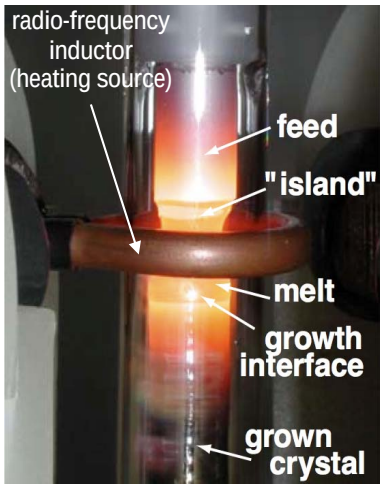

Figure 1.2 : Radio-frequency heating by ring-shaped inductor [Dold, 2004]; reprinted with permission.

depicted, where heating lamps are located at the foci of both ellipsoids. The crystal rod, located at the common focus of both ellipsoids, is heated to develop a molten float-zone. The float-zone (labeled Z in Figure 1.3) is confined between the feed rod and the seed rod by surface tension alone. The length of the molten zone is determined by the heating power and heat distribution. Among its many advantages, the ellipsoid mirror furnace is favorable for crystal growth in space vehicles due to its compact size, low weight and minimal power consumption. For example, using a mono-ellipsoid mirror furnace Eyer *et al.* grew a phosphorus-doped silicon crystal, 8 mm in diameter and 10 mm in length, during the 6 minute weightless phase of a rocket flight [Eyer et al., 1985].

The focused heating on the free surface results in important physics in the float-zone, namely the *Marangoni convection*[4]. The free surface temperature varies from

[4] The Marangoni effect and the Marangoni number are named after the Italian physicist *Carlo Giuseppe Matteo Marangoni* (1840 – 1925). Marangoni studied at the University of Pavia and

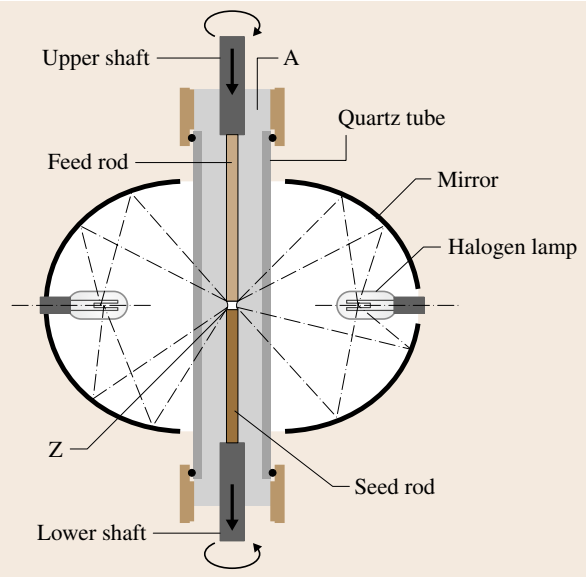

Figure 1.3 : Schematic diagram of optically-heated floating zone crystal growth where Z indicates the float-zone region [Dhanaraj et al., 2010]; reprinted with permission.

a minimum at the melting and solidification fronts to a maximum value at the half-length of the float-zone. Because the surface tension is a function of temperature, this temperature difference drives a flow along the free surface.[5] For most molten semiconductors and liquid metals, the surface tension decreases as temperature rises. Therefore fluid is pulled from the middle of the float-zone, where the surface tension

published his dissertation entitled "Sull' espansione delle gocce liquide" (On the Expansion of Liquid Droplets) in 1865. In June 2010, the 5th Conference of the International Marangoni Association was hosted in Florence, Italy, where Marangoni first worked at the Museo di Fisica (Museum of Physics) and later at the Liceo Dante, where he held a position of high school physics teacher for 45 years, until retirement in 1916.

[5]In fact a sufficiently large temperature gradient at the growth interface is necessary to avoid onset of the morphological instability at the solidification front [Davis, 1993]. Therefore the melt must be heated to a certain extent above its melting point, thus Marangoni convection is inevitable.

is weaker, toward the two ends, where the surface tension is stronger. Then the fluid circulates back through the interior of the float-zone. Marangoni convection describes flow driven by a surface tension gradient. In the optically-heated float-zone process, the surface tension gradient results from the temperature difference, therefore it is also called specifically the *thermocapillary effect*.

The stability of the flow in the molten zone is crucial for successful crystal growth. The crystal growth community has been exploring various techniques to, among other issues, maintain the molten zone without it spilling or freezing, damp convection in the melt and regulate the shape of the growth front. For electrically conducting float-zones, such as molten semiconductors and liquid metals, external steady magnetic fields have been employed to suppress flow instabilities. This is the main subject of Chapter 3. In addition, the feed rod and seed rod are often rotated either in the same direction or in the opposite directions - see [Kahouadji et al., 2011] for a recent study on how rotation speed affects the flow instability in the melt. [Shen et al., 1996] demonstrated the use of high frequency vibrations to suppress flow convection and improve microstructure uniformity. [Lappa, 2005b] reviewed these strategies for convection control in an optically-heated float-zone and also investigated impacts of ambient gas flow control.

Crystals grown using the float-zone method are of high quality but small volume, therefore float-zone experiments are primarily conducted for new materials research. Figure 1.4 shows three GaSb single crystals grown using the float-zone method. Crystal samples labeled FR15 and FR9 were grown in an ellipsoid-paraboloid mirror furnace under microgravity on Spacehab-4 during the STS-77 Space Shuttle flight.[6] The

[6] Sample FR15 was grown during the "night" with no crew activity in the Spacehab module, therefore only a few movements of the zone were observed. Sample FR9 was grown during crew

advantages of conducting float-zone crystal growth under microgravity are twofold. First, the hydrostatic pressure, which greatly limits the diameter and length of the liquid bridge under terrestrial conditions, is eliminated. Second, buoyant convection is also eliminated, allowing for ease of study of the thermocapillary flow, which is a higher-order effect in a terrestrial gravitation field. The rightmost GaSb single crystal sample in Figure 1.4 was grown in $1g$ with the maximum possible growth diameter that can be sustained without spilling [Cröll et al., 1998a].

Figure 1.4 : GaSb single crystals grown using the float-zone method during the Spacehab-4 mission (left and center) and under gravity (right) [Cröll et al., 1998a]; reprinted with permission.

activities, for which significant vibrations were shown in the video record. The axial translation rate (*i.e.* the growth rate) was 6 millimeters per hour [Cröll et al., 1998a].

1.1.2 Bridgman Crystal Growth

The *Bridgman technique*[7] (also referred to as the *Bridgman-Stockbarger*[8] *method*) is a melt growth process contained in an ampule or crucible. Bridgman is used for single element growth and purification, and for binary (or ternary) semiconductor crystal growth of two (or three) group III/V elements.

The Bridgman technique can be carried out in either vertical (Figure 1.5) or horizontal (Figure 1.6) configurations. Independent of orientation, the crystal is grown from the melt in a similar process. Take binary or ternary crystal growth as an example. First, the binary or ternary polycrystalline raw materials (the charge) are combined in the desired proportion and sealed in an ampule. Then the entire ampule is heated above the melting point of the crystal material to ensure complete melting. The melt is maintained for several hours for thorough mixing through convection and diffusion. After that, the ampule is translated through the furnace very slowly (typically 0.5 - 3 mm/hour [Dhanaraj et al., 2010]), allowing the mixture to re-solidify into a binary or ternary crystal, starting from one end of the ampule. After solidification of the entire melt, the grown crystal is slowly cooled to room temperature (typically 10 - 50°C/hour [Dhanaraj et al., 2010]) to avoid thermal shock within the solid ingot. The melting and re-solidification process may be repeated for better uniformity.

The primary advantage of the vertical Bridgman technique is the circular cross-sectional shape of the grown crystal, as opposed to the 'D' shape cross-section that results from horizontal Bridgman growth. Circular wafers are favorable substrates for large-scale epitaxial growth and device fabrication. The primary advantage of the horizontal Bridgman technique is high crystalline quality. The thermal stresses are

[7] Named after the American physicist *Percy Williams Bridgman* (1882 - 1961).

[8] Named after the American physicist *Donald C. Stockbarger* (1895 - 1952).

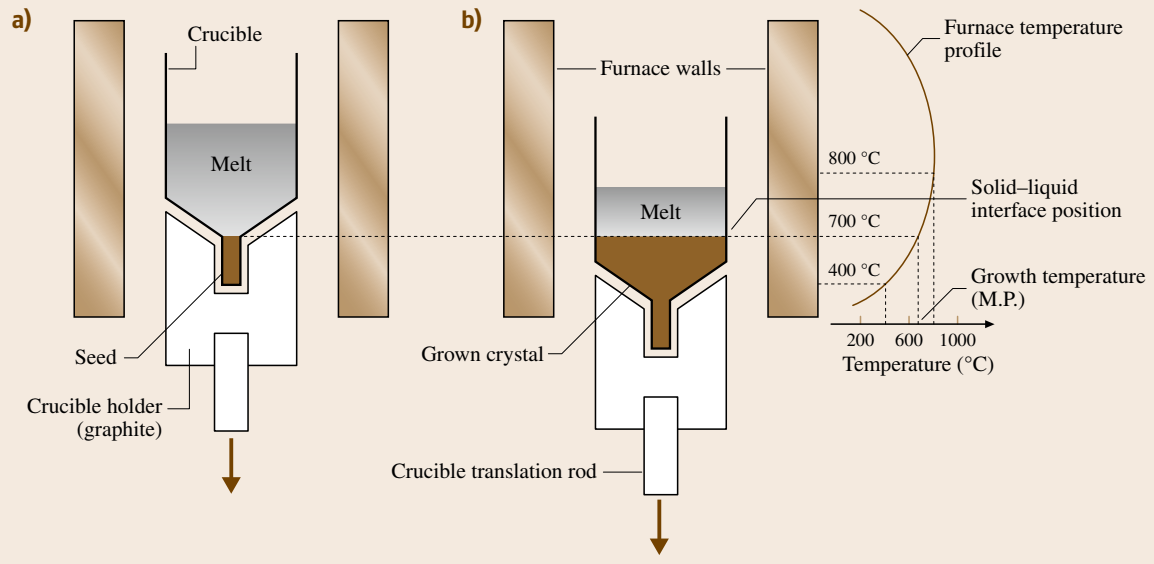

Figure 1.5 : Schematic diagram of a vertical Bridgman crystal growth process in a single-zone furnace: a) at the beginning of the experiment and b) with partially grown crystal [Dhanaraj et al., 2010]; reprinted with permission.

smaller because of the empty space at the top of the ampule.

From the periodic table, *ternary compounds*, some of which can be treated as *pseudobinary*, or *tertiary compounds* (or *alloys*) may consist of either two group III elements and one group V element to form ternaries such as $Ga_{1-x}In_xAs$, or one group III element and two group V elements to form ternaries such as $InP_{1-y}As_y$, where x and y are the mole percentages between 0 and 1, respectively. Varying the alloy composition (x or y) of many ternary alloys allows the lattice parameter and bandgap energy to be tuned. The bandgap for some ternary alloys, such as $Ga_{1-x}In_xSb$, varies continuously, and usually nonlinearly, with composition. This is very desirable for producing substrate materials with specified lattice parameters, and electronic and optoelectronic devices tuned to specific bandgap operation.

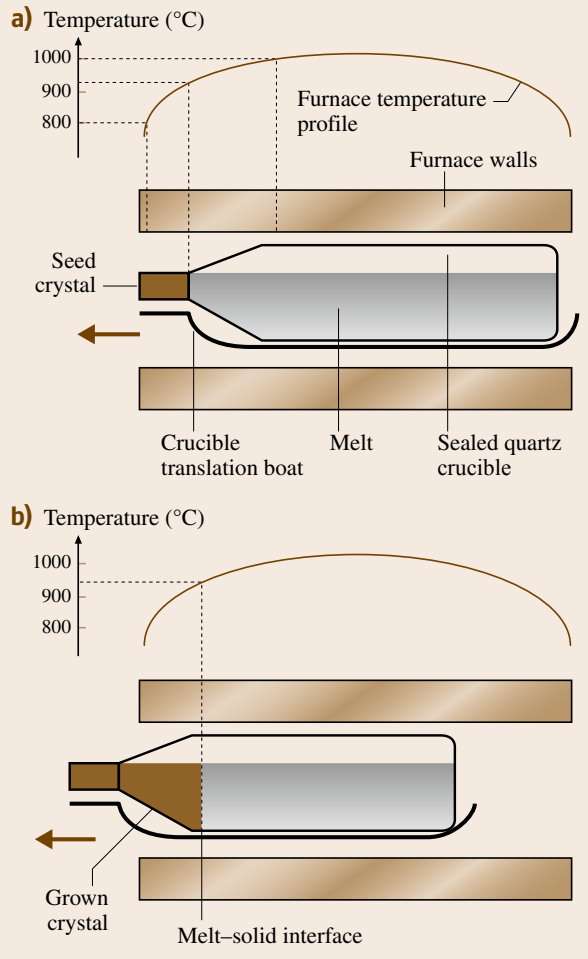

Figure 1.6 : Schematic diagram of a horizontal Bridgman crystal growth process in a single-zone furnace: a) at the beginning of the experiment and b) with partially grown crystal [Dhanaraj et al., 2010]; reprinted with permission.

However, Bridgman growth exhibits several deficiencies when applied to binary and ternary semiconductor growth. The element composition along the length of a Bridgman-grown ternary semiconductor is often inconsistent due to the inherent segregation of many ternary alloys (discussed in Section 1.1.3). In comparison, the *traveling heater method* is able to replenish preferentially solidified constituent element(s) to improve compositional uniformity along the length of the grown crystal.

1.1.3 Traveling Heater Method

The traveling heater method can also be carried out in horizontal and vertical configurations. Using the *horizontal traveling heater method*, constituents are melted and re-solidified in an ampule (Figure 1.7) similar to the horizontal Bridgman method. However, only a section of the charge is melted at any instance. As the heater traverses the length of the ampule, feed material melts at the one edge of the molten zone and re-solidifies into grown crystal at the other. This way, a molten zone is maintained and translates with the movement of the heater. The molten zone allows binary or ternary elements to thoroughly mix through diffusion and convection before crystallization, and allows replenishment of favorably solidified constituents from the feed material.

The traveling heater method is especially promising for producing ternary semiconductor alloys with uniform composition. This challenge in the bulk growth of many such ternary alloys can be best described using a pseudo-binary phase diagram. For example, the ternary $Ga_{1-x}In_xSb$ behaves as GaSb and InSb binaries.[9] The phase di-

[9] The complete $(Ga_{1-x}In_x)_{1-y}Sb_y$ phase diagram is three-dimensional and the liquidus varies with both x and y. Figure 1.8 is a slice of the three-dimensional phase diagram assuming $y = 0.5$ (*i.e.* the atomic percentage of Ga and In combined is 50% and the atomic percentage of Sb is 50%).

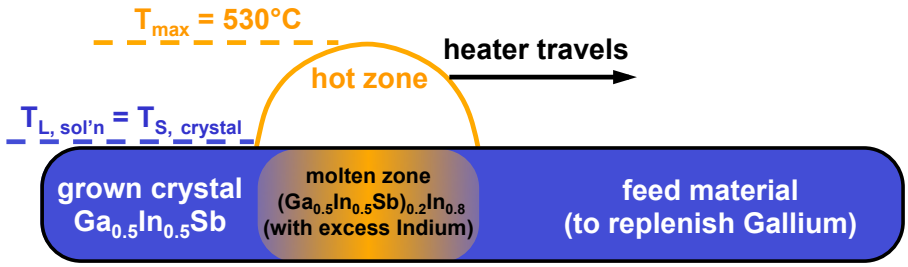

Figure 1.7 : Schematic diagram of a horizontal traveling heater method to grow a GaInSb crystal with excess In as a solvent [Houchens et al., 2009].

agram of $Ga_{1-x}In_xSb$ (Figure 1.8) predicts that, at some growth temperature, Indium is preferentially rejected back into the melt while Gallium preferentially crystallizes. Therefore, the molten zone will contain more and more Indium as it translates, if the feed has a uniform GaInSb composition. Due to this variation of ternary composition in the melt, initially more Gallium solidifies into the head of the crystal. Eventually, the melt becomes Gallium-depleted, resulting in an Indium-rich tail. As a result, the ternary composition along the length of the grown crystal will not be uniform.

This same limitation of non-uniform composition also presents in the Bridgman method. During $Ga_{1-x}In_xSb$ growth, the molten zone becomes an Indium-rich (and Gallium-deficient) solution. The consequence is a highly non-uniform elemental composition throughout the grown crystal, as shown in Figure 1.9a. This diagram shows that Gallium was strongly depleted at the end of the growth process.

However, during the traveling heater method, deficient element(s) can be replenished by the feed material to achieve uniformity throughout in grown ternary alloys. Furthermore, excess of one element, here Indium, can be used as a solvent to place the melt into a favorable region on the ternary phase diagram. For example, a targeted $Ga_{0.5}In_{0.5}Sb$ crystal was grown at Hanscom Air Force Base through the use of excess

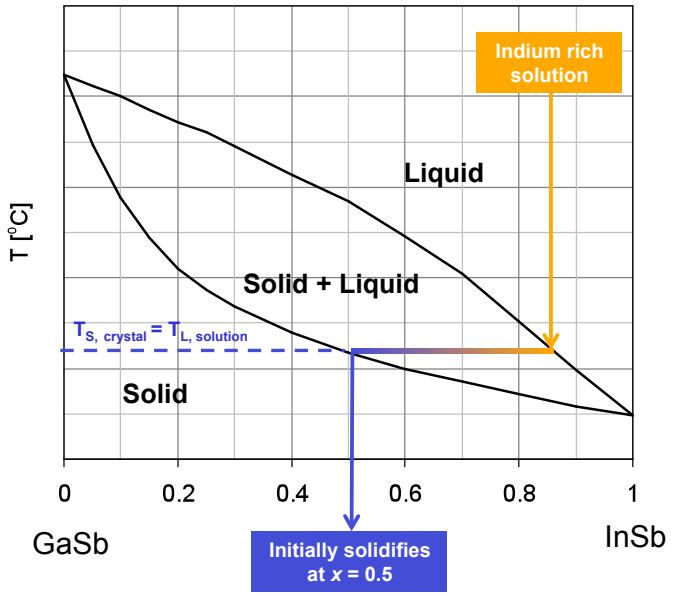

Figure 1.8 : $Ga_{1-x}In_xSb$ phase diagram [Houchens et al., 2009].

Indium as a solvent [Houchens et al., 2010]. The result (Figure 1.9b) shows much improved compositional uniformity throughout, though the growth rate was very slow. A photo of the grown GaInSb ternary crystal is shown in Figure 1.10.

The traveling heater method is primarily a melt growth technique, and when it specifically includes a solvent it is sub-categorized as crystal growth *from solution* (or *solution growth*), and is a hybrid of melt and solution growth. In the above example, GaInSb is crystallized from an excess Indium-rich solvent. Solution growth is especially useful for "substances that melt incongruently, decompose below the melting point, or have several high-temperature polymorphic modifications," with a variety of applications outside of semiconductor crystal growth, including production of processed foods, medicines, fertilizers, pesticides and dyes [Dhanaraj et al., 2010].

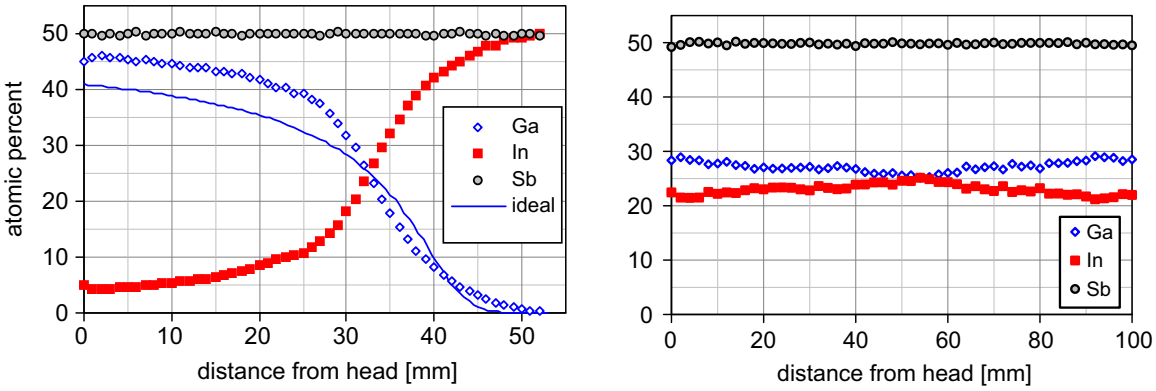

(a) Horizontal Bridgman technique: large variation in element composition

(b) Horizontal traveling heater method with In solvent: improved compositional uniformity

Figure 1.9 : Electron Microprobe analysis of $Ga_{1-x}In_xSb$ crystals grown by (a) horizontal Bridgman (including Ga composition predicted by the ideal phase diagram) and (b) the horizontal traveling heater method [Houchens et al., 2010]; reprinted with permission.

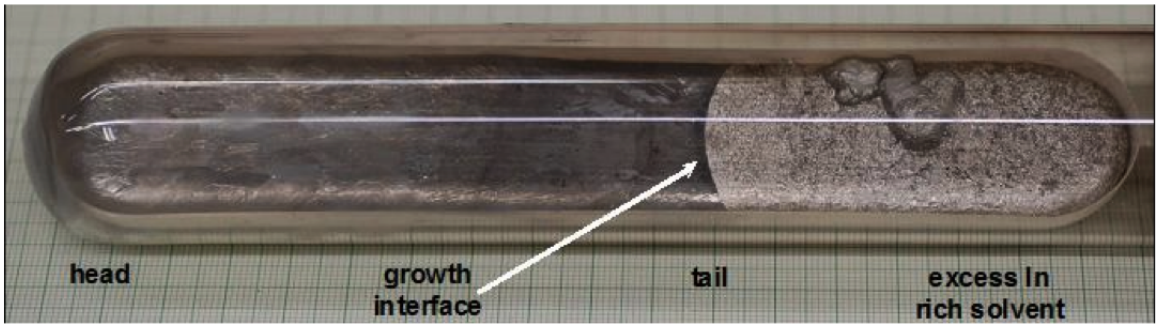

Figure 1.10 : $Ga_{1-x}In_xSb$ crystal grown using the horizontal traveling heater method, inside a boat contained within a quartz ampule [Houchens et al., 2010]; reprinted with permission. The composition of the crystal region is given in Figure 1.9b.

Chapter 2

Applications of Magnetic Fields in Melt Growth

When processing electrically conducted fluids (such as, molten semiconductors and liquid metals), external magnetic fields provide a method of flow control through electromagnetic body forces. The flow $\mathbf{v}$ of an electrically conducting fluid crossing magnetic flux density lines $\mathbf{B}$ induces an electric current density $\mathbf{j}$ in the direction of $\mathbf{v} \times \mathbf{B}$. Subsequently, a Lorentz body force $\mathbf{F}_{\mathrm{EM}} = \mathbf{j} \times \mathbf{B}$ is generated by the electric current density flowing across the magnetic flux density.

The study of dynamics of electrically conducting fluids is a discipline of physics called *magnetohydrodynamics (MHD)*. Aside from magnetic controls in metallurgical process, magnetohydrodynamics covers a wide scope of topics from engineering applications (*e.g.* plasma confinement, and liquid-metal cooling of nuclear reactors), geophysics (*e.g.* reversals of Earth's magnetic field), to astrophysics (*e.g.* formation of planets and stars from electrically conducting matter). Fundamentals of magnetohydrodynamics can be found in textbooks such as [Davidson, 2001, Moreau, 1990].

This work focuses on the branch of magnetohydrodynamics for material processing in the laboratory scale. The concept of magnetic control has been successfully applied in metal casting and refining and magnetic fields are routinely used to melt, pump, stir, and stabilize liquid metals in commercial metallurgical processes. A review of general magnetohydrodynamics in materials processing is available in [Davidson, 1999]. The crystal growth community also utilizes flow control through the application of

external magnetic fields for various crystal growth techniques. Efforts are primarily focused on two ideas: 1. flow damping by steady magnetic fields (*magnetic damping*) to suppress detrimental flow instabilities, and 2. stirring by alternating magnetic fields (*magnetic stirring*) for accelerated mixing between chemical elements, more uniform dopant distribution and breakup of dendritic growth.

2.1 Need for Magnetic Control

The two major issues considered here are magnetic damping to suppress instabilities and magnetic stirring to aid mixing and replenishment of preferentially solidified constituents at the growth front. Magnetic damping is considered in the context of optically-heated float-zone crystal growth in microgravity. Magnetic stirring is applied to traveling heater method growth to force controlled mixing.

2.1.1 Detrimental Flow Instabilities in Float-zone Crystal Growth

Flow instabilities that can develop in the float-zone are generally undesirable for optimum crystal growth. Complex three-dimensional flow patterns in the melt give rise to dopant segregation in the grown crystal. Time-dependent flows lead to alternating melting and re-solidification at the growth front, which introduce defects and additional segregation during crystallization. Instabilities arise when the Marangoni convection (or buoyant or solutal convection in a gravitational field) strengthens beyond a point at which the viscous effect can no longer maintain the base flow state.

Flow visualization of float-zone crystal growth (referred as the Full-Zone in this work) is often impossible because molten semiconductor crystal materials are opaque. However float-zone like instabilities have been demonstrated in a similar configuration (the Half-Zone model) using transparent working fluids with tracer particles. The subtle

differences between the Full-Zone and Half-Zone models are not critical to the concepts in this chapter, but will be discussed in Subsection 3.1.1. For example, [Tanaka et al., 2006] conducted a series of experiments using a silicone oil Half-Zone (Figure 2.1)[1]. By increasing the temperature difference ΔT between the two disks bounding the Half-Zone, the Marangoni convection intensifies. As a result, starting from the axisymmetric, steady base flow state, a progression of instability patterns emerge at different values of Ma until the chaotic flow region is achieved.

Float-zone instabilities of Full-Zone crystal growth experiments are evidenced by post-examination of grown crystals, due to the opaque nature of the materials when molten. For example, Figure 2.2 shows the GaSb sample FR15 from Figure 1.4 sectioned lengthwise and polished. This axial slice was then etched in a HF / CH_3COOH / $KMnO_4$ solution to reveal striations [Cröll et al., 1998a]. In the lower part of Figure 2.2 striations are visible, which is an indication of oscillatory Marangoni convection in the liquid-bridge during growth. Striations vanish in the upper part of Figure 2.2 due to the change in liquid bridge length. This indicates that instability was suppressed and Marangoni convection was weakened to a steady state, potentially the base flow state.

The crystal growth community has been investigating the float-zone (also referred to as the *liquid bridge* and used interchangeably in this content) flow instabilities and exploring ways to suppress them for a few decades. Both axial and transverse magnetic fields have been used to stabilize the float-zone [Kimura et al., 1983, Robertson and O'Connor, 1986]. Since gravitational effects deform the free surface shape and greatly limit the grown crystal diameter and the related buoyant convection is another source

[1] Please note that Figure 2.1 is not a complete collection of their observations. Readers are referred to [Tanaka et al., 2006] for complete results and analysis. Videos of their experiments are available at `http://murasun.me.noda.tus.ac.jp/marangoni.html`.

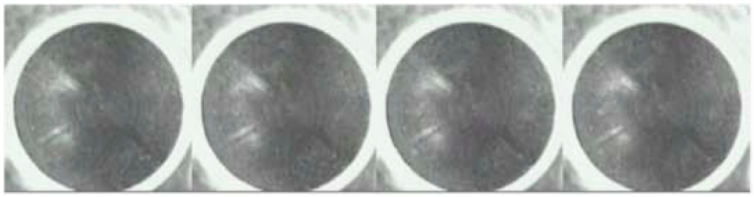

(a) Base flow at $Ma = 0.2 \times 10^4$

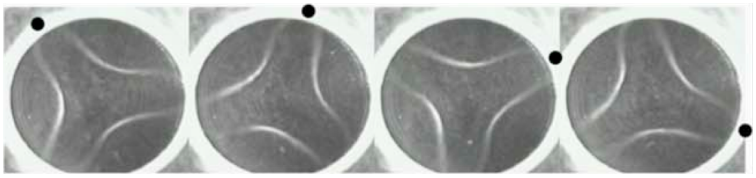

(b) Instability: traveling wave at $Ma = 4.8 \times 10^4$

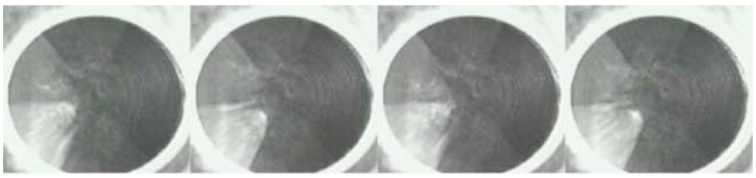

(c) Instability: standing wave at $Ma = 5.8 \times 10^4$

(d) Instability: chaotic flow at $Ma = 9.8 \times 10^4$

Figure 2.1 : Some Half-Zone instabilities observed by tracer particle visualization (Top view consecutive snapshots taken every 7/30 second from left to right. Higher Marangoni numbers Ma correspond to stronger Marangoni driving effect. Click each figure to see the associated experimental video. Test fluid was silicone oil 2 cSt ($Pr = 28.1$) at 25°C. Half-Zone diameter and height are 5 mm and 1.6 mm, respectively [Tanaka et al., 2006]; reprinted with permission.

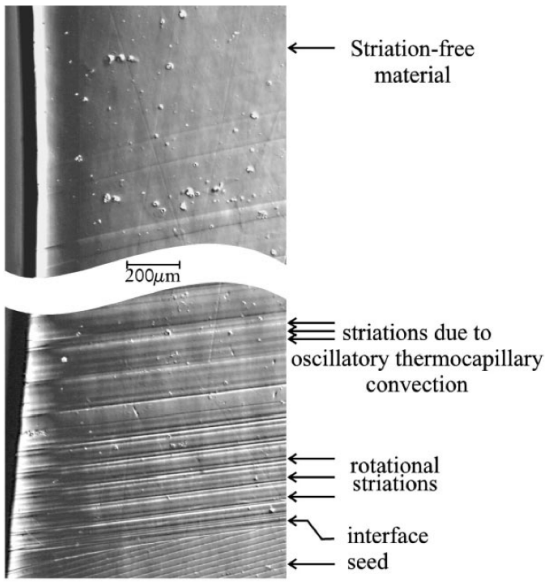

Figure 2.2 : Full-Zone instabilities cause striations in grown GaSb crystal (Nomarsky differential interference contrast micrograph of sample FR15 from Figure 1.4) [Cröll et al., 1998a]; reprinted with permission.

of instability, several float-zone crystal growth experiments were conducted in a microgravity environment to study Marangoni convection explicitly.

For example, Cröll *et al.* confirmed experimentally that Marangoni convection and associated instabilities are the major contributors to dopant striations, and could be greatly reduced by application of an axial magnetic field [Cröll et al., 1994, Cröll et al., 1998b]. Martinez and Eyer grew two silicon crystal rods in a double ellipsoidal mirror furnace with rod rotation in Spacelab-1 [Martinez and Eyer, 1986]. Nakamura *et al.* observed $m = 1$ and 2 oscillating instability modes of molten silicon in an optically heated Half-Zone configuration on the TR-IA rocket [Nakamura et al., 1998]. In addition to magnetic damping, high frequency vibration was also demonstrated experimentally to suppress Marangoni convection and improve microstructure unifor-

mity [Shen et al., 1996]. Lappa reviewed these strategies for Marangoni flow control in a model of laterally heated float-zone growth and also investigated impacts of ambient gas flow control [Lappa, 2005b].

2.1.2 Insufficient Mixing in Bridgman and Traveling Heater Methods

The growth rate using the Bridgman method is very slow for binary (0.5 - 3 mm/hour) and ternary (0.1 - 1 mm/hour) alloy semiconductors. This is due to the slow diffusion rates between elements, which must equilibrate at the growth front. Forced convection can be introduced by exposing the melt to alternating external magnetic fields for accelerated growth.

Furthermore, the growth rate in the traveling heater method is even slower, as low as 1.2 mm/day, as reported in [Houchens et al., 2010]. Substantial time is required to allow the solute to diffuse from the feed rod to replenish the preferentially solidified element at the growth front. To accelerate the mixing process, alternating magnetic fields are introduced in the traveling heater method for ternary semiconductors and alloy growth. When exposed to an alternating magnetic field, electromagnetic body forces are induced within the molten zone, stirring the melt. With the forced convection, mixing between chemical elements is enhanced. Therefore, the traveling heater method with magnetic stirring has been proposed to grow ternary semiconductors and alloys at much faster growth rates, and with better cross-sectional and axial uniformity as compared to Bridgman grown crystals.

2.2 Magnetohydrodynamics Modeling

Magnetohydrodynamics (MHD) problems in general are governed by Maxwell's electromagnetic equations coupled to the equations of motion and the energy equation.

In the following sections the governing equations are described and then simplified for the case of semiconductor crystal growth at the laboratory scale. Throughout, quantities with an asterisk superscript are dimensional. Quantities without an asterisk superscript are nondimensional.

2.2.1 Electromagnetic Equations

Maxwell's equations consist of four equations. In differential form, these are

1. Gauss's law:

$$\nabla^* \cdot \mathbf{E}^* = \frac{\rho_e^*}{\epsilon_0}, \tag{2.1}$$

where $\mathbf{E}^*$ is the electric field, ρ_e^* is the electric charge density, and $\epsilon_0 = 8.85 \times 10^{-12}$ $\mathrm{C}^2/\mathrm{Nm}^2$ is the permitivity of free space. Gauss's law relates the electric charge ρ_e^* to the electric field $\mathbf{E}^*$ produced. In its integral form, Gauss's law states that the electric flux through any closed surface is proportional to the enclosed electric charge ρ_e^*.

2. $\mathbf{B}^*$ is solenoidal. That is, the divergence of $\mathbf{B}^*$ is zero:

$$\nabla^* \cdot \mathbf{B}^* = 0, \tag{2.2}$$

where $\mathbf{B}^*$ is the magnetic flux density. This is sometimes referred to as "Gauss's law for magnetism" and indicates that, unlike electric charges, there are no magnetic "charges" and therefore magnetic flux lines do not end. They either form closed loops or extend to infinity. Equation 2.2 is analogous to Gauss's law for the electric field (Equation 2.1), except the right hand side of Equation 2.2 is always zero, indicating that there are no magnetic monopoles (or no magnetic charges).

3. Faraday's law:

$$\nabla^* \times \mathbf{E}^* = -\frac{\partial \mathbf{B}^*}{\partial t^*}, \tag{2.3}$$

where t^* is time. Faraday's law indicates that changes in the magnetic flux density $\mathbf{B}^*$ result in an electric field $\mathbf{E}^*$.

4. Ampère's law:

$$\nabla^* \times \mathbf{B}^* = \mu_p^* \mathbf{j}^*, \tag{2.4}$$

where $\mathbf{j}^*$ is the electric current density, μ_p^* is the magnetic permeability, and the displacement electric currents have been neglected, as is appropriate for crystal growth materials. Ampère's law determines the magnetic field $\mathbf{B}^*$ generated by an electric current density $\mathbf{j}^*$.

Here, as is typical for crystal growth applications, the magnetic permeability μ_p^* and electrical conductivity σ^* are assumed constant throughout the melt.

Aside from Maxwell's equations, Ohm's law:

$$\mathbf{j}^* = \sigma^*(\mathbf{E}^* + \mathbf{v}^* \times \mathbf{B}^*) \tag{2.5}$$

is a constitutive equation that states that electric current density $\mathbf{j}^*$ can be generated by an electric field $\mathbf{E}^*$ and by flow motion $\mathbf{v}^*$ crossing magnetic flux lines $\mathbf{B}^*$.

Furthermore, a Lorentz force

$$\mathbf{F}_{\mathrm{EM}}^* = \mathbf{j}^* \times \mathbf{B}^* \tag{2.6}$$

is generated whenever electric current density $\mathbf{j}^*$ crosses magnetic flux lines.

2.2.2 Transport Equation for $\mathbf{B}^*$ and Scaling

Ohm's law (Equation 2.5) is used to eliminate the electric current density in Ampère's law (Equation 2.4). Then, taking the curl of the resulting equation and assuming

constant electrical conductivity σ^* and constant magnetic permeability μ_p^* gives

$$\nabla^* \times (\nabla^* \times \frac{\mathbf{B}^*}{\mu_p^*}) = \sigma^* \nabla^* \times (\mathbf{E}^* + \mathbf{v}^* \times \mathbf{B}^*). \tag{2.7}$$

Expanding Equation 2.7 via cross-product vector identities, and using Faraday's law (Equation 2.3) to replace $\nabla^* \times \mathbf{E}^*$ gives

$$\nabla^* \underbrace{(\nabla^* \cdot \frac{\mathbf{B}^*}{\mu_p^*})}_{\substack{=0 \\ \text{Equation 2.2}}} - \nabla^{*2} \frac{\mathbf{B}^*}{\mu_p^*} = \sigma^* \underbrace{(\nabla^* \times \mathbf{E}^*)}_{\substack{=-\partial \mathbf{B}^*/\partial t^* \\ \text{Faraday's law}}} +$$
$$+\sigma^* [(\mathbf{B}^* \cdot \nabla^*)\mathbf{v}^* - (\mathbf{v}^* \cdot \nabla^*)\mathbf{B}^* + \mathbf{v}^* \underbrace{(\nabla^* \cdot \mathbf{B}^*)}_{\substack{=0 \\ \text{Equation 2.2}}} - \mathbf{B}^* \underbrace{(\nabla^* \cdot \mathbf{v}^*)}_{\substack{=0 \\ \text{continuity} \\ \text{Equation 2.32}}}]. \tag{2.8}$$

Rearranging the remaining terms yields the *transport equation for* $\mathbf{B}^*$

$$\underbrace{\frac{\partial \mathbf{B}^*}{\partial t^*}}_{\text{variation in time}} + \underbrace{(\mathbf{v}^* \cdot \nabla^*)\mathbf{B}^*}_{\text{advection}} = \underbrace{\frac{1}{\mu_p^* \sigma^*} \nabla^{*2} \mathbf{B}^*}_{\text{diffusion}} + \underbrace{\mathbf{B}^* \cdot (\nabla^* \mathbf{v}^*)}_{\substack{\mathbf{B}^* \text{ field production} \\ \text{by stretching of} \\ \text{magnetic flux lines}}} . \tag{2.9}$$

The first two terms in Equation 2.9 combined are the material derivative of $\mathbf{B}^*$, denoted as $D\mathbf{B}^*/Dt^*$. The Laplacian term shows the tendency for $\mathbf{B}^*$ to diffuse, analogous to heat conduction. The last term $\mathbf{B}^* \cdot (\nabla^* \mathbf{v}^*)$ can be interpreted as magnetic flux lines $\mathbf{B}^*$ being stretched by the velocity gradient $\nabla^* \mathbf{v}^*$, which increases the magnetic flux density in the direction of stretching.

The transport equation for $\mathbf{B}^*$ demonstrates the coupling between the magnetic flux density $\mathbf{B}^*$ and the flow field $\mathbf{v}^*$ for general MHD problems. Exposed to an external magnetic field, flow of an electrically conducting fluid crossing $\mathbf{B}^*$ generates electric current via Ohm's law. This electric current induces its own magnetic flux density via Ampère's law, which superimposes onto the original external magnetic field. Therefore, the overall magnetic field is, in general, altered by the flow motion. Simultaneously, the electric current density crossing magnetic flux lines produces a Lorentz force,

which affects the flow motion. Thus the most general MHD modeling requires solving the momentum equations and electromagnetic equations simultaneously.

The transport equation for $\mathbf{B}^*$ (Equation 2.9) is now nondimensionalized to evaluate the importance of each term for crystal growth processes. The characteristic values are defined by $\mathbf{B}^* = \mathbf{B}B_0^*$, where B_0^* is the characteristic magnetic flux density, $\mathbf{v}^* = \mathbf{v}V_0^*$, where V_0^* is the characteristic velocity magnitude, $\nabla^* = \frac{\nabla}{L_0^*}$, where L_0^* is the characteristic length, and $t^* = t\ t_0^*$, where t_0^* is the characteristic time. Equation 2.9 becomes

$$\frac{B_0^*}{t_0^*}\frac{\partial \mathbf{B}}{\partial t} + \frac{B_0^* V_0^*}{L_0^*}(\mathbf{v}\cdot\nabla)\mathbf{B} = \frac{1}{\mu_p^*\sigma^*}\frac{B_0^*}{L_0^{*2}}\nabla^2\mathbf{B} + \frac{B_0^* V_0^*}{L_0^*}\mathbf{B}\cdot(\nabla\mathbf{v}). \tag{2.10}$$

Dropping the common factor B_0^*, then multiplying by $\mu_p^*\sigma^* L_0^{*2}$ gives the *nondimensional transport equation for* $\mathbf{B}$:

$$\underbrace{\frac{\mu_p^*\sigma^* L_0^{*2}}{t_0^*}\frac{\partial \mathbf{B}}{\partial t}}_{\text{variation in time}} + \underbrace{\overbrace{\mu_p^*\sigma^* V_0^* L_0^*}^{R_m}(\mathbf{v}\cdot\nabla)\mathbf{B}}_{\text{advection}} = \underbrace{\nabla^2\mathbf{B}}_{\text{diffusion}} + \underbrace{\overbrace{\mu_p^*\sigma^* V_0^* L_0^*}^{R_m}\mathbf{B}\cdot(\nabla\mathbf{v})}_{\substack{\mathbf{B}\text{ field production}\\ \text{by stretching of}\\ \text{magnetic flux lines}}}. \tag{2.11}$$

The ratio of advection to diffusion of $\mathbf{B}$ is defined as the *magnetic Reynolds number*

$$R_m = \mu_p^*\sigma^* V_0^* L_0^*. \tag{2.12}$$

Defining the *magnetic diffusivity* as $\lambda^* = 1/(\mu_p^*\sigma^*)$, then R_m can be rewritten as $R_m = V_0^* L_0^*/\lambda^*$, which has a similar form to the viscous Reynolds number $R_m = V_0^* L_0^*/\nu^*$ where $\nu^* = \mu^*/\rho^*$ is the kinematic viscosity. Equation 2.11 also indicates that the rate of $\mathbf{B}$ field enhancement by stretching of magnetic flux lines is on the same order as the advection rate.

2.2.3 Electromagnetic Equation Decoupling in Crystal Growth Modeling

For crystal growth applications, the magnetic Reynolds number R_m is quite small ($\sim 10^{-4}$ to 10^{-2}). Typical values in the laboratory scale are $\mu_p^*\sigma^* \sim 1$ s/m^2, $V_0^* \sim 10^{-2}$

to 10^{-1} m/s and $L_0^* \sim 10^{-2}$ to 10^{-1} m. Therefore, $\mathbf{B}$ is distributed mostly by diffusion in crystal growth processes. After neglecting the advection and stretching terms for small R_m, the remaining terms in the transport equation for $\mathbf{B}$ (Equation 2.11) become

$$\frac{\mu_p^* \sigma^* L_0^{*2}}{t_0^*} \frac{\partial \mathbf{B}}{\partial t} = \nabla^2 \mathbf{B}. \tag{2.13}$$

Therefore, for typical crystal growth applications, the magnetic field is decoupled from the velocity field, which greatly simplifies the MHD numerical modeling. In this limit the flow field does not affect the magnetic field, though the magnetic field does affect the flow field. The coupling is one way. The magnetic field is completely determined by Equation 2.13 with proper initial and boundary conditions. Once the magnetic field is solved, the electric field is determined by Ohm's law (Equation 2.5). The effect of the electromagnetic field on the flow field is only through the Lorentz body force term in the Navier-Stokes equations.

For the special case of a static magnetic field applied to a low R_m flow, the governing equation for the magnetic flux density further simplifies to

$$\nabla^2 \mathbf{B} = \mathbf{0}. \tag{2.14}$$

It is important to note that the magnetic Reynolds number R_m is fully determined by the fluid properties μ_p^* and σ^* and the scales of the fluid flow, V_0^* and L_0^*. R_m is independent of $\mathbf{B}^*$ and the way in which it is generated externally. This is true both if it is generated by a steady or alternating external current. Therefore, in the case of an alternating magnetic field the frequency (and therefore the period) of the field plays a critical role in further scaling of Equation 2.13.

2.2.4 Shielding Parameter and Skin Depth for Alternating Magnetic Fields

The magnetic Reynolds number R_m reveals that the diffusion rate of $\mathbf{B}^*$ is a finite quantity, *i.e.* the magnetic field *takes time* to penetrate into the conducting media, analogous to heat diffusion. The finite diffusion time is most prominent in large R_m problems where the diffusion term in Equation 2.11 is small. This work focuses rather on small R_m. However, this limit alone does not guarantee that the time derivative of $\mathbf{B}^*$ in Equation 2.13 is negligible.

Even with small R_m, a finite diffusion rate may be observed during crystal growth in the presence of a high-frequency alternating magnetic field. The very short alternating period of the externally applied $\mathbf{B}^*_{\text{ext}}$ may be comparable or even shorter than the diffusion time (which itself is already typically very short). The surrounding $\mathbf{B}^*_{\text{ext}}$ only penetrates by a *skin depth* into the conducting media before $\mathbf{B}^*_{\text{ext}}$ itself changes. The core region below this skin depth is barely affected by the high-frequency alternating magnetic field, remaining almost free of the influence of $\mathbf{B}^*_{\text{ext}}$. This is the *shielding effect* associated with high-frequency alternating magnetic fields.

The shielding effect is quantifiable through a second dimensionless group. Suppose an external magnetic field $\mathbf{B}^*_{\text{ext}}$ alternates with the frequency $f^*_{\text{ext}} = \omega^*_{\text{ext}}/(2\pi)$ (often referred to as the *AC frequency* in this work), where ω^*_{ext} is the angular frequency. Substituting $1/\omega^*_{\text{ext}}$ for the characteristic time t^*_0, Equation 2.13 becomes

$$\underbrace{\frac{\mu^*_p \sigma^* L^{*2}_0}{1/\omega^*_{\text{ext}}}}_{R_\omega} \frac{\partial \mathbf{B}}{\partial t} = \nabla^2 \mathbf{B}, \tag{2.15}$$

where the *shielding parameter* R_ω is defined as

$$R_\omega = \mu^*_p \sigma^* \omega^*_{\text{ext}} L^{*2}_0. \tag{2.16}$$

Rewriting Equation 2.15 as

$$\underbrace{\frac{1}{1/\omega^*_{\text{ext}}}}_{\substack{\text{alternating rate} \\ \text{of } \mathbf{B}^*_{\text{ext}}}} \frac{\partial \mathbf{B}}{\partial t} = \underbrace{\frac{1}{\mu^*_p \sigma^* L^{*2}_0}}_{\text{diffusion rate}} \nabla^2 \mathbf{B}, \tag{2.17}$$

it is clear that the alternating rate of $\mathbf{B}^*_{\text{ext}}$ is $\frac{1}{1/\omega^*_{\text{ext}}}$. The alternating period of $\mathbf{B}^*_{\text{ext}}$ is then $1/\omega^*_{\text{ext}}$. The diffusion rate of $\mathbf{B}^*$ in the conducting media is $\frac{1}{\mu^*_p \sigma^* L^{*2}_0}$ and the diffusion time is $\mu^*_p \sigma^* L^{*2}_0$. Thus, the shielding parameter R_ω can be interpreted as

$$R_\omega = \frac{\text{alternating rate of } \mathbf{B}^*_{\text{ext}}}{\text{diffusion rate of } \mathbf{B}^*} = \frac{\text{diffusion time of } \mathbf{B}^*}{\text{alternating period of } \mathbf{B}^*_{\text{ext}}}.$$

Note that $\mathbf{B}^*$ in the conducting media is not necessarily the same as the external magnetic field $\mathbf{B}^*_{\text{ext}}$. Due to the finite response time to the alternating $\mathbf{B}^*_{\text{ext}}$, the magnetic flux density lines $\mathbf{B}^*$ may be distorted within the conducting media, as shown in Chapter 4. The magnetic flux density in the conducting media $\mathbf{B}^*$ is solved by Equation 2.17 for small magnetic Reynolds number R_m or by the complete Equation 2.9 for a general R_m. All cases treated here will be for $R_m \ll 1$.

$R_\omega > 1$ corresponds to a fast alternating $\mathbf{B}^*_{\text{ext}}$ with high angular frequency ω^*_{ext}, as compared to a slower diffusion response of $\mathbf{B}^*$ in the media – *i.e.* stirring with a high-frequency, alternating-current (AC) generated magnetic field. Within each AC period, $\mathbf{B}^*_{\text{ext}}$ does not have sufficient time to penetrate into the conducting media. The shielding effect is strong in this case. In the limit of $\omega^*_{\text{ext}} \to \infty$, the shielding parameter $R_\omega \to \infty$, and the conducting media would be free of $\mathbf{B}^*_{\text{ext}}$.

For $R_\omega < 1$, $\mathbf{B}^*_{\text{ext}}$ alternates slowly so that the diffusion of $\mathbf{B}^*$ is deep into the conducting media. Thus $\mathbf{B}^*$ responds completely before $\mathbf{B}^*_{\text{ext}}$ changes. The limit of $R_\omega \to 0$ implies either that $\mathbf{B}^*_{\text{ext}}$ is steady with $\omega^*_{\text{ext}} = 0$ (and hence $\mathbf{B}^*$ is also steady) or that the media is a perfect conductor with $\sigma^* \to \infty$, in which case $\mathbf{B}^*$ responds instantaneously to changes in $\mathbf{B}^*_{\text{ext}}$.

The limits suggest the presence of a *magnetic skin depth*, conventionally defined as

$$\delta_m^* = \sqrt{\frac{2}{\mu_p^* \sigma^* \omega_{\text{ext}}^*}}. \tag{2.18}$$

At high AC frequencies ω_{ext}^*, the magnetic shield parameter R_ω is large. The shielding effect is strong. The magnetic skin depth is shallow, as shown by

$$R_\omega = \mu_p^* \sigma^* \omega_{\text{ext}}^* L_0^{*2} = 2 \left(\frac{L_0^*}{\delta_m^*} \right)^2. \tag{2.19}$$

Note that the shielding effect discussed in this subsection is not limited to cases with small magnetic Reynolds number R_m. Equation 2.15 is used for simplicity because the crystal growth flows of interest have $R_m \ll 1$.

2.2.5 Navier-Stokes Equations Exposed to a Steady Magnetic Field

Starting from their dimensional incompressible form and neglecting gravitational effects, the Navier-Stokes equations (*i.e.* conservation of momentum), including the electromagnetic body force, are

$$\rho^* \frac{\partial \mathbf{v}^*}{\partial t^*} + \rho^* (\mathbf{v}^* \cdot \nabla^*) \mathbf{v}^* = -\nabla^* P^* + \mu^* \nabla^{*2} \mathbf{v}^* + \underbrace{\mathbf{j}^* \times \mathbf{B}^*}_{\mathbf{F}_{\text{EM}}^*}, \tag{2.20}$$

where $\mathbf{v}^*$ is flow velocity, P^* is pressure, ρ^* is the fluid density, and μ^* is the dynamic viscosity, all taken as constants.

When the electrical-conducting media is exposed to an external steady magnetic field, electric current $\mathbf{j}^*$ is induced by flow motion crossing the magnetic flux lines via

$$\mathbf{j}^* = \sigma^* (\mathbf{v}^* \times \mathbf{B}^*). \tag{2.21}$$

Thus, the Navier-Stokes equations, when exposed to a steady magnetic field, become

$$\rho^* \frac{\partial \mathbf{v}^*}{\partial t^*} + \rho^* (\mathbf{v}^* \cdot \nabla^*) \mathbf{v}^* = -\nabla^* P^* + \mu^* \nabla^{*2} \mathbf{v}^* + \underbrace{\sigma^* (\mathbf{v}^* \times \mathbf{B}^*) \times \mathbf{B}^*}_{\mathbf{F}_{\text{EM}}^*}. \tag{2.22}$$

Equations 2.22 are nondimensionalized as follows, where dimensional quantities are indicated by the superscript *. The characteristic length is L_0^*. Therefore $\nabla^* = \nabla / L_0^*$. The flow velocity is scaled as $\mathbf{v}^* = \mathbf{v} V_0^*$, with the characteristic velocity $V_0^* = \nu^* / L_0^*$, where $\nu^* = \mu^* / \rho^*$ is the kinematic viscosity. Time is scaled as $t^* = t\ t_0^*$, with the characteristic time set to $t_0^* = L_0^* / V_0^* = L_0^{*2} / \nu^*$. Pressure is scaled by $P^* = P \Delta P_0^*$, with the characteristic pressure difference set to $\Delta P_0^* = \rho^* V_0^{*2} = \rho^* \nu^{*2} / L_0^{*2}$. The magnetic flux density is given by $\mathbf{B}^* = \mathbf{B} B_0^*$, where B_0^* is the dimensional magnitude of the steady applied field.

After nondimensionalization, the Navier-Stokes equations become

$$\rho^* \frac{V_0^*}{t_0^*} \frac{\partial \mathbf{v}}{\partial t} + \rho^* \frac{V_0^{*2}}{L_0^*} (\mathbf{v} \cdot \nabla) \mathbf{v} = - \frac{\Delta P_0^*}{L_0^*} \nabla P + \mu^* \frac{V_0^*}{L_0^{*2}} \nabla^2 \mathbf{v} + \sigma^* V_0^* B_0^{*2} (\mathbf{v} \times \mathbf{B}) \times \mathbf{B}.$$

Then, multiplying every term by $L_0^* / (\rho^* V_0^{*2})$ gives

$$\frac{L_0^*}{t_0^* V_0^*} \frac{\partial \mathbf{v}}{\partial t} + (\mathbf{v} \cdot \nabla) \mathbf{v} = - \frac{\Delta P_0^*}{\rho^* V_0^{*2}} \nabla P + \frac{\mu^*}{\rho^* V_0^* L_0^*} \nabla^2 \mathbf{v} + \frac{\sigma^* L_0^* B_0^{*2}}{\rho^* V_0^*} (\mathbf{v} \times \mathbf{B}) \times \mathbf{B}.$$

Substituting in the characteristic time $t_0^* = L_0^* / V_0^*$, characteristic pressure difference $\Delta P_0^* = \rho^* V_0^{*2}$ and characteristic flow velocity $V_0^* = \nu^* / L_0^* = \mu^* / (\rho^* L_0^*)$ gives the *Navier-Stokes equations when exposed to an external, steady magnetic field* as

$$\frac{\partial \mathbf{v}}{\partial t} + (\mathbf{v} \cdot \nabla) \mathbf{v} = - \nabla P + \underbrace{\frac{\mu^*}{\rho^* V_0^* L_0^*}}_{\frac{1}{Re_{\text{classic}}}} \nabla^2 \mathbf{v} + \underbrace{\frac{\sigma^*}{\mu^*} L_0^{*2} B_0^{*2}}_{Ha^2} (\mathbf{v} \times \mathbf{B}) \times \mathbf{B}. \tag{2.23}$$

where Re_{classic} is the *classic viscous Reynolds number*

$$Re_{\text{classic}} = \frac{\rho^* V_0^* L_0^*}{\mu^*}, \tag{2.24}$$

indicating the ratio of the inertia to viscous terms. The dimensionless *Hartmann number*

$$Ha = \left(\frac{\sigma^*}{\mu^*} \right)^{\frac{1}{2}} B_0^* L_0^* \tag{2.25}$$

measures the importance of the electromagnetic body forces to the viscous effects. In the context of magnetic damping using a steady magnetic field, Ha is a common measure of magnetic flux density $\mathbf{B}^*$. See Subsection 3.2.3 for further discussion of Hartmann number Ha effects.

Note that the choice of a viscous velocity scale $V_0^* = \mu^*/(\rho^* L_0^*)$ yields $Re_{\text{classic}} = 1$, which is commonly seem in flow dynamics studies. With $Re_{\text{classic}} = 1$, the final form of the Navier-Stokes equations when exposed to an external, steady magnetic field becomes

$$\frac{\partial \mathbf{v}}{\partial t} + (\mathbf{v} \cdot \nabla)\mathbf{v} = -\nabla P + \nabla^2 \mathbf{v} + Ha^2(\mathbf{v} \times \mathbf{B}) \times \mathbf{B}. \tag{2.26}$$

This choice of scaling with $Re_{\text{classic}} = 1$ does not preclude the formation of boundary layers, but the boundary layer mechanism is not that of classical fluid mechanics. Here, the balance between any driving effect (which in Chapter 3 will be thermocapillary driving for a crystal growth process with a free surface) and magnetic damping leads to boundary layers. The formation of boundary layers is particularly common when the melt is contained within electrically insulating boundaries, as these force the electric current density to flow in thin layers adjacent to the boundary.

2.2.6 Navier-Stokes Equations Exposed to an Alternating Magnetic Field

For magnetic stirring during crystal growth, the alternating frequency $f_{\text{ext}}^* = \omega_{\text{ext}}^*/(2\pi)$ of the external magnetic field must be considered relative to how fast the flow can respond. If the angular frequency of the field is very high, the external field may change much faster than the response, yielding the case $\omega_{\text{ext}}^* L_0^* \gg V_0^*$. Furthermore, if the angular frequency of the external field ω_{ext}^* is very high, even the resulting $\mathbf{B}^*$ in the flow may respond slowly due to the shielding effect associated with $R_\omega > 1$.

When electrically conducting media is exposed to an external alternating magnetic

field, electric current $\mathbf{j}^*$ is induced by the relative motion $\mathbf{v}^*_{\text{rel}}$ between the flow and the magnetic field

$$\mathbf{j}^* = \sigma^*(\mathbf{v}^*_{\text{rel}} \times \mathbf{B}^*). \tag{2.27}$$

The dimensional Navier-Stokes equations, when exposed to a rotating magnetic field, are

$$\rho^* \frac{\partial \mathbf{v}^*}{\partial t^*} + \rho^*(\mathbf{v}^* \cdot \nabla^*)\mathbf{v}^* = -\nabla^* P^* + \mu^* \nabla^{*2}\mathbf{v}^* + \underbrace{\sigma^*(\mathbf{v}^*_{\text{rel}} \times \mathbf{B}^*) \times \mathbf{B}^*}_{\mathbf{F}^*_{\text{EM}}} \tag{2.28}$$

are nondimensionalized in a similar way to the steady magnetic field case in Subsection 2.2.5 but with the new scaling of the relative velocity $\mathbf{v}^*_{\text{rel}} = \mathbf{v}_{\text{rel}} V^*_{\text{rel},0}$ where $V^*_{\text{rel},0} = \omega^*_{\text{ext}} L^*_0$. Equation 2.28 becomes

$$\rho^* \frac{V^*_0}{t^*_0} \frac{\partial \mathbf{v}}{\partial t} + \rho^* \frac{V^{*2}_0}{L^*_0}(\mathbf{v} \cdot \nabla)\mathbf{v} = -\frac{\Delta P^*_0}{L^*_0}\nabla P + \mu^* \frac{V^*_0}{L^{*2}_0}\nabla^2 \mathbf{v} + \sigma^* \omega^*_{\text{ext}} L^*_0 B^{*2}_0 (\mathbf{v}_{\text{rel}} \times \mathbf{B}) \times \mathbf{B}.$$

Multiplying every term by $L^*_0/(\rho^* V^{*2}_0)$ gives

$$\frac{L^*_0}{t^*_0 V^*_0}\frac{\partial \mathbf{v}}{\partial t} + (\mathbf{v} \cdot \nabla)\mathbf{v} = -\frac{\Delta P^*_0}{\rho^* V^{*2}_0}\nabla P + \frac{\mu^*}{\rho^* V^*_0 L^*_0}\nabla^2 \mathbf{v} + \frac{\sigma^* \omega^*_{\text{ext}} B^{*2}_0 L^{*2}_0}{\rho^* V^{*2}_0}(\mathbf{v}_{\text{rel}} \times \mathbf{B}) \times \mathbf{B}.$$

Substituting the characteristic time $t^*_0 = L^*_0/V^*_0$, the characteristic pressure difference $\Delta P^*_0 = \rho^* V^{*2}_0$, and the characteristic flow velocity $V^*_0 = \nu^*/L^*_0 = \mu^*/(\rho^* L^*_0)$, the *Navier-Stokes equations when exposed to a rotating magnetic field* become

$$\frac{\partial \mathbf{v}}{\partial t} + (\mathbf{v} \cdot \nabla)\mathbf{v} = -\nabla P + \underbrace{\frac{\mu^*}{\rho^* V^*_0 L^*_0}}_{\frac{1}{Re_{\text{classic}}}} \nabla^2 \mathbf{v} + \underbrace{\frac{\sigma^* \omega^*_{\text{ext}} B^{*2}_0 L^{*4}_0}{\rho^* \nu^{*2}}}_{2 \times Ta_m} (\mathbf{v}_{\text{rel}} \times \mathbf{B}) \times \mathbf{B}, \tag{2.29}$$

where the *magnetic Taylor number*[2]

$$Ta_m = \frac{\sigma^* \omega^*_{\text{ext}} B^{*2}_0 L^{*4}_0}{2\rho^* \nu^{*2}} \tag{2.30}$$

[2] This is analogous to the more common *Taylor number* $Ta = 4\omega^{*2} L^{*4}_0/\nu^{*2}$, which measures the importance of centrifugal forces as compared to viscous effects.

measures the electromagnetic body force of a rotating magnetic field over viscous effects.

Again, the choice of a viscous velocity scale requires $Re_{\text{classic}} = 1$, but does not preclude boundary layer development. The factor of 2 is typically absorbed into the scaling on the electromagnetic body force, where $\mathbf{F}^*_{\text{EM}}$ then scales as $\sigma^*\omega^*_{\text{ext}}B^{*2}_0 L^*_0/2$. The resulting Navier-Stokes equations when exposed to a rotating magnetic field are

$$\frac{\partial \mathbf{v}}{\partial t} + (\mathbf{v}\cdot\nabla)\mathbf{v} = -\nabla P + \nabla^2\mathbf{v} + Ta_m\mathbf{F}_{\text{EM}}. \tag{2.31}$$

2.2.7 Continuity and Energy Equations

Buoyancy and gravity effects are not considered in this work. Assume constant density ρ^*, viscosity μ^*, specific heat c^*_p and thermal conductivity k^*. Aside from the Navier-Stokes equations, the nondimensional governing equations for the flow dynamics also include

1. Incompressible, constant density continuity (conservation of mass):

$$\nabla\cdot\mathbf{v} = 0. \tag{2.32}$$

2. Conservation of energy:

$$Pr\left[\frac{\partial T}{\partial t} + (\mathbf{v}\cdot\nabla)T\right] = \nabla^2 T, \tag{2.33}$$

where T is the temperature and the *Prandtl number* $Pr = \mu^* c^*_p/k^*$ is a material property indicating the relative effectiveness of thermal convection to heat conduction in the melt. The Prandtl number includes the dynamic viscosity μ^*, the specific heat c^*_p, and the thermal conductivity k^*. See Subsection 3.2.3 for further discussion of Prandtl number Pr effects.

Chapter 3

Flow Damping by Steady Magnetic Field

This chapter investigates how a steady magnetic field is used to suppress detrimental flow instabilities in crystal growth. The *float-zone crystal growth process* is chosen for demonstration. During this process, if the thermocapillary flow is too intense, instabilities in the melt cause transient melting and resolidification at the crystal growth front, which subsequently introduce defects and non-uniformity into the grown crystal. Furthermore, a minimum temperature gradient must be maintained at the growth front to avoid onset of the morphological instability, which results in polycrystalline solidification [Davis, 1993]. Therefore it is not possible to completely avoid the thermocapillary flow. To suppress the resulting flow instabilities, a constant, uniform external magnetic field is applied in the direction perpendicular to the growth front. Any flow motion normal to the magnetic field direction is damped by the Lorentz force, which is induced by the flow motion itself.

3.1 Liquid Bridge

The liquid bridge refers to the molten region in the float-zone crystal growth process (Figure 3.1). As the name suggests, a small amount of molten material is confined between two solid crystal rods, the feed rod and the grown crystal rod, by wetting. The liquid bridge free surface is exposed to inert gas and holds itself in place by surface tension. This molten region is produced by focused heating onto a section of a crystal

rod above its melting temperature.

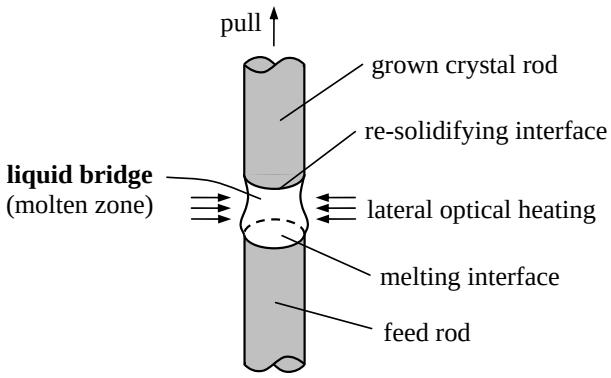

Figure 3.1 : Liquid bridge in the optically-heated float-zone crystal growth process with sagging due to the influence of gravity (Full-Zone)

3.1.1 Half-Zone and Full-Zone Models

The liquid bridge has become a classic model for Marangoni convection study. Two simplified models of float-zone crystal growth are commonly used in both numerical and experimental studies – the *Half-Zone* and the *Full-Zone*. In microgravity only the Marangoni (thermocapillary) force drives the flow.

Half-Zone

Roughly speaking, the Half-Zone models one half of the liquid bridge – from either one of the solid-liquid interfaces to the mid-plane, also referred to as the "equatorial plane". Note that "mid-plane" always refers to the cross-sectional plane at the half-length of a Full-Zone. The half-length of a Half-Zone is of no special significance. The solid-liquid interface is often approximated by a no-slip boundary maintained at a lower, uniform temperature through cooling. The mid-plane is replaced by another

no-slip, no-penetration boundary held at a higher uniform temperature by heating, as shown in Figure 3.2. Since this experiment was in microgravity, orientation has no importance. This heated solid boundary imposes a momentum constraint to the flow field which does not exist in the crystal growth molten zone. Furthermore, the temperature at the mid-lane is not uniform in the true crystal growth molten zone. These deficiencies in the Half-Zone model of liquid bridge crystal growth are corrected in the Full-Zone model.

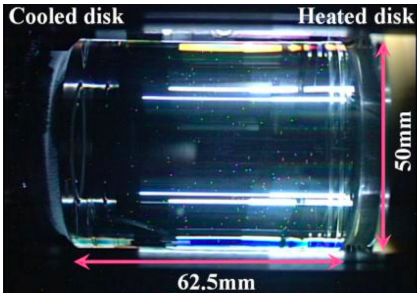

Figure 3.2 : "Marangoni Experiment in Space" (MEIS)-4, Half-Zone liquid bridge experiment, in the Japanese Experimental Module "KIBO" on the International Space Station (working fluid: silicone oil with the kinematic viscosity of 20cSt, Prandtl number $Pr = 207$ at 25^{o}C) [Yano et al., 2011]; reprinted with permission.

However, the Half-Zone is an excellent model to study Marangoni effect due to several advantages. Half-Zone liquid bridge is bounded by two concentric disks. The length of the liquid bridge and temperature difference between two disks are relatively easy to control in experiments. Transparent and low melting temperature test fluids can be used, allowing for interior flow visualization by introducing tracer particles. Because most of these working liquids are at room temperature, they do not pose a

fire hazard in spacecraft.[1] Commonly used test fluids include silicone oil ($Pr = 68$ at 25°C [Kawamura et al., 2010]), acetone ($Pr = 4.4$ at 20 or 23°C [Simic-Stefani et al., 2006]), n-decane ($Pr = 14.7$ at 20°C [Schwabe et al., 2007]) and sodium nitrate ($Pr = 8.0$ at 350°C [Schwabe et al., 2007]), where the Prandtl number Pr is a material property. For $Pr > 1$ fluids, convective heat transfer is dominant over thermal conduction.

Full-Zone

The Full-Zone models the entire molten zone, with both ends of the liquid bridge at the melting temperature. All actal float-zone crystal growth experiments are Full-Zone. The primary differences from the Half-Zone are that 1) no boundary is imposed at the mid-plane in the Full-Zone and 2) a heat flux is applied on the free surface in the Full-Zone. Fluid is allowed to travel across the mid-plane, which often occurs in liquid bridge flow instabilities. This important physics is not allowed in the Half-Zone model, be it through experimental studies or numerical simulations. For a typical liquid bridge configuration, the thermocapillary driving force required for the onset of instabilities in the Half-Zone is 25% to 50% larger than that in the Full-Zone for $Pr \leq 0.05$, and the two models diverge further at higher Pr [Houchens and Walker, 2005]. These first Full-Zone instabilities have been confirmed by Bouizi and Delcarte by comparing linear stability theory to saturated disturbances from transient, three-dimensional spectral simulations [Bouizi et al., 2007].

Commonly used crystal growth materials include molten silicon ($Pr = 0.01$ [Teng

[1] During Full-Zone experiments in spacecraft, materials are heated above their melting points – usually on the order of 1000°C. Liquid bridges can spill out if surface tension fails to hold the melt and at such high temperatures pose a great fire hazard in spacecraft.

et al., 2010]), molten GaSb ($Pr = 0.042$ [Cröll et al., 1998a]), molten Bi ($Pr = 0.017$ [Cröll et al., 1998a]) and molten Sn ($Pr = 0.01$ [Takagi et al., 2001, Yang and Kou, 2001]). Note that conductive heat transfer is dominant over convection for $Pr < 1$ fluids. Compared to Half-Zone experiments, Full-Zone float-zone crystal growth experiments are more challenging to control. In addition, in low Pr fluids, flow field measurements are hindered by the opaque nature and generally high melting temperatures of the fluids. Thus, most semiconductors grown by optically-heated, float-zone crystal growth are analyzed post-growth, by measuring micro- and macro-segregation of grown crystals [Dold, 2004].

3.1.2 Full-Zone Numerical Model

The Full-Zone model shown in Figure 3.3 is investigated in this chapter. The liquid bridge geometry is approximated by a cylinder of radius R^* and length $2bR^*$, where b is the aspect ratio. Throughout, the length of the Full-Zone is assumed equal to the diameter ($b = 1$). The free surface is approximated as a non-deformable cylinder, although the actual free surface would be barrel-shaped in space or sagged down under gravity. The melting and re-solidifying interfaces are approximated by planar, no-slip, no-penetration surfaces, although these are observed to be curved in experiments due to flow convection. These two ends are fixed at the melting temperature T_0^*. The lateral heat flux onto the free surface is assumed axisymmetric. It decays parabolically from a maximum q^* at the mid-plane to 0 at two solid-liquid interfaces as

$$k^* \frac{\partial T^*}{\partial r^*} = q^* \left[1 - \left(\frac{z^*}{bR^*} \right)^2 \right], \tag{3.1}$$

where k^* is the thermal conductivity. The liquid bridge is exposed to a constant axial magnetic field B_0^*. The fluid is incompressible and gravitational and buoyant effects

are neglected for a microgravity environment. All symbols with an asterisk superscript are dimensional quantities.

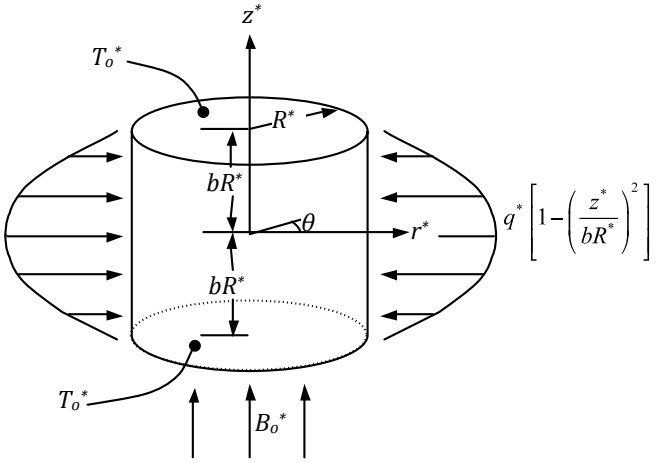

Figure 3.3 : Full-Zone exposed to a constant axial magnetic field. Note that the B_0^* field penetrates uniformly throughout the entire liquid bridge.

Nondimensionalization is carried out as follows. The length scale is set to R^*. The viscous velocity scale is $V^* = \mu^*/(\rho^* R^*)$, where μ^* is the dynamic viscosity and ρ^* is the fluid density. The time and pressure scales are chosen to be R^{*2}/ν^* and $\rho^*\nu^{*2}/R^{*2}$, respectively, where $\nu^* = \mu^*/\rho^*$ is the kinematic viscosity. The temperature is scaled as $T = (T^* - T_0^*)/\Delta T^*$, where $\Delta T^* = q^* R^*/k^*$.

In general, the flow field and electromagnetic fields must be solved simultaneously for an electric conducting fluid, because the flow velocity $\mathbf{v}$ determines the Lorentz body force, which then acts on the flow field itself. Here the magnetic flux density $\mathbf{B}$ is assumed to be constant, uniform and specified by some external electric current density, in this case a solenoidal current. The properties of the melt are assumed constant. The low magnetic Reynolds number limit ($R_m = \mu_p^* \sigma^* V^* R^* \ll 1$) is taken

such that the magnetic and velocity fields partially decouple (the coupling is now one-way) and the induced magnetic field is neglected.

Thus Maxwell's equations are not required and only the induced electric field in the melt resulting from Ohm's law remains to be solved, along with the flow field. In this case, the remaining nondimensional governing equations are incompressible continuity (repeating Equation 2.32), the Navier-Stokes equations including the electromagnetic body force, the energy equation neglecting viscous dissipation (repeating Equation 3.32), conservation of charge in the melt and Ohm's law in the melt:

$$\nabla \cdot \mathbf{v} = 0,$$

$$\frac{\partial \mathbf{v}}{\partial t} + (\mathbf{v} \cdot \nabla)\mathbf{v} = -\nabla P + \nabla^2 \mathbf{v} + Ha^2(\mathbf{j} \times \hat{\mathbf{e}}_z), \tag{3.2}$$

$$Pr\left[\frac{\partial T}{\partial t} + (\mathbf{v} \cdot \nabla)T\right] = \nabla^2 T,$$

$$\nabla \cdot \mathbf{j} = 0, \tag{3.3}$$

$$\mathbf{j} = -\nabla\phi + \mathbf{v} \times \hat{\mathbf{e}}_z, \tag{3.4}$$

where ϕ is the electric potential field and

$$Ha = \left(\frac{\sigma^*}{\mu^*}\right)^{\frac{1}{2}} B_o^* R^*, \tag{3.5}$$

$$Pr = \frac{\mu^* c_p^*}{k^*} = \frac{\nu^*}{\alpha^*}. \tag{3.6}$$

The *Hartmann number* Ha is proportional to the magnetic flux density B_o^* and measures the ratio of the electromagnetic body forces to the viscous forces. Notice that the magnetic field only has an axial component $\mathbf{B}^* = B_o^* \hat{\mathbf{e}}_z$ here. At high Ha (strong B_o^* field), the electromagnetic body force term $Ha^2(\mathbf{j} \times \hat{\mathbf{e}}_z)$ becomes dominant in the Navier-Stokes equations.

The *Prandtl number* Pr indicates the relative effectiveness of thermal convection to heat conduction in the melt. Pr is a material property, where c_p^* and α^* are the specific heat and thermal diffusivity of the melt, respectively. This work focuses on fluids with small Prandtl number, for which heat conduction is dominant over convection.

The boundary conditions at each end of the cylinder are

$$\mathbf{v} = \mathbf{0}, \quad T = 0, \quad \text{and} \quad j_z = 0 \quad \text{at} \quad z = \pm b. \tag{3.7}$$

Boundary conditions at the free surface are

$$\begin{aligned} v_r = 0, \quad j_r = 0, \quad \tau_{r\theta} = -Re_{FZ}\frac{1}{r}\frac{dT}{d\theta}, \\ \tau_{rz} = -Re_{FZ}\frac{dT}{dz} \quad \text{and} \quad \frac{\partial T}{\partial z} = 1 - \left(\frac{z}{b}\right)^2 \quad \text{at} \quad r = 1, \end{aligned} \tag{3.8}$$

where $\tau_{r\theta}$ and τ_{rz} are shear stresses. Derivation of these thermocapillary stresses is available in [Huang, 2009]. Re_{FZ} is the *thermocapillary Reynolds number*

$$Re_{FZ} = \frac{\rho^* R^* \left|\frac{d\gamma^*}{dT^*}\right| \Delta T^*}{\mu^{*2}} \tag{3.9}$$

where the subscript FZ refers to the Full-Zone model.

The thermocapillary Reynolds number Re_{FZ} measures the shear stress intensity resulting from surface tension variations due to temperature gradients on the free surface, relative to viscous effects. A greater Re_{FZ} corresponds to a stronger thermocapillary driving force. The related *Marangoni number* $Ma = Re_{FZ}Pr$ is also commonly used in the literature. In comparison, the *classic viscous Reynolds number* Re_{classic} is defined previously in Subsection 2.2.5 as

$$Re_{\text{classic}} = \frac{\rho^* V_0^* R^*}{\mu^*}, \tag{3.10}$$

where $V_0^* = \mu^*/(\rho^* R^*)$ is the choice of the characteristic flow velocity.

The surface tension γ^* is assumed to decay linearly as temperature rises

$$\gamma^* = \gamma_0^* + \frac{d\gamma^*}{dT^*}\left(T^* - T_0^*\right), \tag{3.11}$$

where $d\gamma^*/dT^*$ is a negative quantity. The surface tension γ^* is scaled by $|d\gamma^*/dT^*|\,\Delta T^*$, which simplifies the nondimensional value of $d\gamma/dT$ to -1.

3.2 Base Flow

In a Full-Zone liquid bridge, the weakest flow state is called the *base flow* state. In the simplest case when no magnetic field is present, the Marangoni convection forms a pair of symmetric toroids (Figure 3.4). At the free surface, fluid is pulled away from the middle of the liquid bridge toward the two ends, then circulates back through the interior. The donut-shaped surfaces in Figure 3.4 are stream function iso-surfaces of the base flow (*i.e.* flow particles move along these surfaces). The base flow state is steady, axisymmetric and exhibits axial symmetry with respect to the mid-plane.

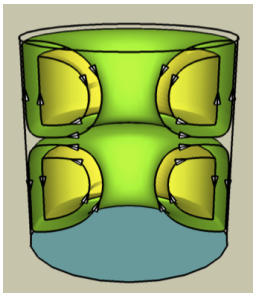

Figure 3.4 : Illustration of the base flow stream function iso-surfaces in a Full-Zone liquid bridge when no magnetic field is present

The base flow state is not entirely undesirable for float-zone growth as the weak, steady flow improves uniformity in the final crystal. However, a quiescent melt is

even more desirable for eliminating defects. Unfortunately, to avoid the morphological instability, a minimum temperature gradient must be maintained at the growth front, requiring a minimum temperature gradient on the free surface. Merely one degree of temperature difference on the free surface is sufficient to induce the thermocapillary flow. Furthermore, if the Marangoni convection intensifies due to a slight increase in heat input (often required to avoid interface breakdown) *instabilities* in the flow field (also called *perturbations* or *disturbances* interchangeably in this content) may develop in time. These cause the base flow to evolve into more complex three-dimensional and/or pulsing (time-dependent) flows. These flow fields are even less desirable than the axisymmetric base state, as periodicity in particular results in cyclical melting and resolidification of the growth front, leading to striations. Applying a steady, axial magnetic field is a strategy to suppress both the instabilities and the base state, yielding a quiescent interior region ideal for uniform, defect-free crystal growth.

3.2.1 Base Flow Formulations

The base flow is steady ($\partial/\partial t = 0$), axisymmetric ($\partial/\partial\theta = 0$) with zero azimuthal velocity ($v_{\theta 0} = 0$) and exhibits axial symmetry with respect to the mid-plane. Therefore, the base flow can be solved in axisymmetric (2D) cylindrical coordinates (r and z). Base flow variables are denoted with subscript 0 to differentiate them from perturbation variables, which are denoted with subscript 1.

Primitive Variable Formulation

With the above assumptions the base flow governing equations simplify to

$$\frac{\partial v_{r0}}{\partial r} + \frac{v_{r0}}{r} + \frac{\partial v_{z0}}{\partial z} = 0, \tag{3.12}$$

$$v_{r0}\frac{\partial v_{r0}}{\partial r} + v_{z0}\frac{\partial v_{r0}}{\partial z} = -\frac{\partial P_0}{\partial r} + \frac{\partial^2 v_{r0}}{\partial r^2} + \frac{1}{r}\frac{\partial v_{r0}}{\partial r} - \frac{v_{r0}}{r^2} + \frac{\partial^2 v_{r0}}{\partial z^2} - Ha^2 v_{r0}, \tag{3.13}$$

$$v_{r0}\frac{\partial v_{z0}}{\partial r} + v_{z0}\frac{\partial v_{z0}}{\partial z} = -\frac{\partial P_0}{\partial z} + \frac{\partial^2 v_{z0}}{\partial r^2} + \frac{1}{r}\frac{\partial v_{z0}}{\partial r} + \frac{\partial^2 v_{z0}}{\partial z^2}, \tag{3.14}$$

$$Pr\left(v_{r0}\frac{\partial T_0}{\partial r} + v_{z0}\frac{\partial T_0}{\partial z}\right) = \frac{\partial^2 T_0}{\partial r^2} + \frac{1}{r}\frac{\partial T_0}{\partial r} + \frac{\partial^2 T_0}{\partial z^2}, \tag{3.15}$$

with boundary conditions

$$v_{r0} = 0, \quad \frac{\partial v_{z0}}{\partial r} = -Re_{FZ}\frac{\partial T_0}{\partial z}F(z) \quad \text{and} \quad \frac{\partial T_0}{\partial r} = 1 - \left(\frac{z}{b}\right)^2 \quad \text{at} \quad r = 1, \tag{3.16}$$

$$v_{r0} = 0, \quad v_{z0} = 0 \quad \text{and} \quad T_0 = 0 \quad \text{at} \quad z = \pm b, \tag{3.17}$$

where

$$F(z) = 1 - \exp\left\{-\alpha\left[1 - \left(\frac{z}{b}\right)^2\right]^2\right\} \tag{3.18}$$

is a regularization function to remove the $\partial v_{z0}/\partial r$ singularity at $(r, z) = (1, \pm b)$ between the thermocapillary driving force on the free surface and the no-penetration conditions at the top and bottom boundaries.

Notice that the base flow electric field reduces to

$$j_{r0} = 0, \quad j_{z0} = 0, \quad j_{\theta 0} = -v_{r0} \quad \text{and} \quad \phi = \text{constant} \tag{3.19}$$

through the solution of conservation of charge (Equation 3.3) and Ohm's law (Equation 3.4) with related boundary conditions under the base flow assumptions. Therefore, variables $\mathbf{j}$ and ϕ do not appear in the base flow formulation (Equations 3.12 to 3.17).

Equations 3.12 to 3.17 are the *primitive variable formulation* of the base flow with four unknowns v_{r0}, v_{z0}, P_0 and T_0. A detailed derivation of these base flow equations is available in [Huang, 2009].

4^{th} Order Stream Function Formulation

Houchens and Walker combined these base flow equations into two governing equations in two unknowns ψ and T_0 in the 4^{th} *order stream function formulation* [Houchens and Walker, 2001, Houchens and Walker, 2005]. The momentum equations become

$$\begin{aligned}\frac{\partial^4\psi}{\partial r^4} - \frac{2}{r}\frac{\partial^3\psi}{\partial r^3} + \frac{3}{r^2}\frac{\partial^2\psi}{\partial r^2} - \frac{3}{r^3}\frac{\partial\psi}{\partial r} + 2\frac{\partial^4\psi}{\partial r^2\partial z^2} - \frac{2}{r}\frac{\partial^3\psi}{\partial r\partial z^2} + \frac{\partial^4\psi}{\partial z^4} \\ - Ha^2\frac{\partial^2\psi}{\partial z^2} + \frac{1}{r}\frac{\partial\psi}{\partial r}\left[\frac{\partial^3\psi}{\partial r^2\partial z} - \frac{1}{r}\frac{\partial^2\psi}{\partial r\partial z} + \frac{\partial^3\psi}{\partial z^3}\right] \\ - \frac{1}{r}\frac{\partial\psi}{\partial z}\left[\frac{\partial^3\psi}{\partial r^3} - \frac{3}{r}\frac{\partial^2\psi}{\partial r^2} + \frac{3}{r^2}\frac{\partial\psi}{\partial r} + \frac{\partial^3\psi}{\partial r\partial z^2} - \frac{2}{r}\frac{\partial^2\psi}{\partial z^2}\right] = 0, \end{aligned} \tag{3.20}$$

where ψ is the stream function in the axisymmetric cylindrical domain defined as

$$v_{r0} = \frac{1}{r}\frac{\partial\psi}{\partial z}, \quad v_{z0} = -\frac{1}{r}\frac{\partial\psi}{\partial r}. \tag{3.21}$$

The energy equation becomes

$$Pr\left(\frac{1}{r}\frac{\partial\psi}{\partial z}\frac{\partial T_0}{\partial r} - \frac{1}{r}\frac{\partial\psi}{\partial r}\frac{\partial T_0}{\partial z}\right) = \frac{\partial^2 T_0}{\partial r^2} + \frac{1}{r}\frac{\partial T_0}{\partial r} + \frac{\partial^2 T_0}{\partial z^2}, \tag{3.22}$$

and the boundary conditions are

$$\psi = 0, \quad \frac{\partial^2\psi}{\partial r^2} - \frac{\partial\psi}{\partial r} = Re_{FZ}\frac{\partial T_0}{\partial z}F(z) \quad \text{and} \quad \frac{\partial T_0}{\partial r} = 1 - \left(\frac{z}{b}\right)^2 \quad \text{at} \quad r = 1, \tag{3.23}$$

$$\frac{\partial\psi}{\partial z} = 0, \quad \psi = 0 \quad \text{and} \quad T_0 = 0 \quad \text{at} \quad z = b. \tag{3.24}$$

The "4^{th} order" refers to the maximum order of derivatives appearing in the governing equations. With this formulation, the liquid bridge with moderate magnetic damping was successfully resolved. [Houchens, 2005] reported results up to $Ha = 100$ for a Full-Zone with $Pr = 0.02$ (for silicon melt).

The magnetic damping effect imposes a great numerical challenge for liquid bridge simulations. The electromagnetic force effectively confines the Marangoni convection into a shallow layer near the free surface. Flow circulation within this narrow layer

causes a large velocity gradient where the free surface and solid boundaries meet. [Houchens, 2005] employed Gauss-Lobatto collocation grids and allocated the finest grid resolution in these regions. A global spectral method with Chebyshev basis functions was also used for discretization to achieve spectral accuracy. The trigonometric definition of the *Chebyshev functions of the first kind* is

$$T_n(x) = \cos\left[n * \arccos(x)\right]. \tag{3.25}$$

A recurrence relation between the Chebyshev functions is also available and is preferred in actual computations. The recursion relation is given by

$$T_0(x) = 1, \tag{3.26}$$

$$T_1(x) = x, \tag{3.27}$$

$$T_{n+1}(x) = 2xT_n(x) - T_{n-1}(x). \tag{3.28}$$

A major source of numerical difficulty in the 4^{th} order stream function formulation was the combination of low and high order derivatives of Chebyshev basis functions in the same equation. A common observation is that derivatives of Chebyshev functions increase dramatically as the derivative order increases. Therefore, in the momentum equation the 4^{th} order derivative coefficients ($\partial^4\psi/\partial r^4$ and $\partial^4\psi/\partial z^4$) dwarf those of the 1^{st} and 2^{nd} order derivatives (for example, $\partial\psi/\partial r$ and $\partial^2\psi/\partial z^2$) by several orders of magnitude. Inspired by the difficulties of the 4^{th} order stream function formulation, this work aims at extending the limit of magnetic damping that can be studied by improving the numerics. To that end, a 2^{nd} order vorticity transport formulation is introduced.

2^{nd} Order Vorticity Transport Formulation

Based on difficulties observed in the 4^{th} order stream function solution, lowering the order of derivatives that must be approximated by Chebyshev functions is a logical way to improve the numerics. In this work, this is achieved at the expense of the addition of one variable – the azimuthal vorticity ω_θ, defined as

$$\omega_\theta = \frac{\partial v_{r0}}{\partial z} - \frac{\partial v_{z0}}{\partial r}. \tag{3.29}$$

This allows for derivation of the 2^{nd} *order vorticity transport formulation*, with vorticity and stream function related by

$$\omega_\theta = \frac{1}{r}\frac{\partial^2 \psi}{\partial r^2} - \frac{1}{r^2}\frac{\partial \psi}{\partial r} + \frac{1}{r}\frac{\partial^2 \psi}{\partial z^2}. \tag{3.30}$$

The momentum equations become

$$\frac{1}{r}\frac{\partial \psi}{\partial z}\left[\frac{\partial \omega_\theta}{\partial r} - \frac{\omega_\theta}{r}\right] - \frac{1}{r}\frac{\partial \psi}{\partial r}\left[\frac{\partial \omega_\theta}{\partial z}\right] = \frac{\partial^2 \omega_\theta}{\partial r^2} + \frac{1}{r}\frac{\partial \omega_\theta}{\partial r} + \frac{\partial^2 \omega_\theta}{\partial z^2} - \frac{\omega_\theta}{r^2} - \frac{Ha^2}{r}\frac{\partial^2 \psi}{\partial z^2}, \tag{3.31}$$

and the energy equation becomes

$$Pr\left(\frac{1}{r}\frac{\partial \psi}{\partial z}\frac{\partial T_0}{\partial r} - \frac{1}{r}\frac{\partial \psi}{\partial r}\frac{\partial T_0}{\partial z}\right) = \frac{\partial^2 T_0}{\partial r^2} + \frac{1}{r}\frac{\partial T_0}{\partial r} + \frac{\partial^2 T_0}{\partial z^2}. \tag{3.32}$$

The boundary conditions are

$$\psi = 0, \quad \frac{\partial^2 \psi}{\partial r^2} - \frac{\partial \psi}{\partial r} = Re_{FZ}\frac{\partial T_0}{\partial z}F(z) \quad \text{and} \quad \frac{\partial T_0}{\partial r} = 1 - \left(\frac{z}{b}\right)^2 \quad \text{at} \quad r = 1, \tag{3.33}$$

$$\frac{\partial \psi}{\partial z} = 0, \quad \psi = 0 \quad \text{and} \quad T_0 = 0 \quad \text{at} \quad z = b. \tag{3.34}$$

The complete derivation of this formulation can be found in [Huang, 2009].

The "2^{nd} order" refers to the maximum order of derivatives that appears in the governing equations. The 2^{nd} order vorticity transport formulation is used for the rest of this chapter.

3.2.2 Numerical Techniques

The numerical solution of the base flow is now presented. This includes the form of the spectral collocation representation, special treatment of the equations at $r = 0$ and $z = 0$, and regularization of the vorticity singularity in the boundary conditions at the outside corner of the domain.

Base Flow Chebyshev Polynomial Representation

In the 2^{nd} order vorticity transport formulation the three base flow variables ψ, ω_θ and T_0 are represented with global Chebyshev polynomials over the domain $r \in [0, 1]$ and $z \in [0, b]$. The representations are

$$\psi\left(r, \frac{z}{b}\right) = r^2 \sum_{L=0}^{NRF+1} \sum_{M=0}^{NZF+1} A_{LM} T_{2L}(r) T_{2M+1}\left(\frac{z}{b}\right), \tag{3.35}$$

$$\omega_\theta\left(r, \frac{z}{b}\right) = r \sum_{L=0}^{NRF} \sum_{M=0}^{NZF} B_{LM} T_{2L}(r) T_{2M+1}\left(\frac{z}{b}\right), \tag{3.36}$$

$$T_0\left(r, \frac{z}{b}\right) = \sum_{L=0}^{NRT} \sum_{M=0}^{NZT} C_{LM} T_{2L}(r) T_{2M}\left(\frac{z}{b}\right), \tag{3.37}$$

where $T_n(r)$ and $T_n(z/b)$ are Chebyshev basis functions defined in Equation 3.25. A_{LM}, B_{LM} and C_{LM} are the unknown coefficients of the Chebyshev polynomials.

Equations 3.35 to 3.37 are determined based on several numerical considerations. Firstly, the r^2 and r multiples in ψ and ω_θ respectively are chosen to ensure non-zero A_{00} and B_{00} using the *Method of Frobenius*. This method investigates the governing equations 3.30 and 3.31 at the singularity as $r \to 0$. This derivation is available in Appendix A of [Huang, 2009]. Note that the temperature, governed by the energy equation 3.32, is nonzero at $r = 0$ and therefore no factor of r is required in the representation of T_0.

Secondly, because of the axisymmetry and the axial symmetry, only even or odd Chebyshev terms are kept in both the r and z directions. Chebyshev polynomials $T_n(x)$ are even if n is even and odd if n is odd. The stream function ψ is even in the radial direction.[2] Therefore ψ has only even radial Chebyshev terms $T_{2L}(r)$, with the r^2 multiple in ψ retaining this symmetry. All of the odd radial Chebyshev coefficients in ψ are identically zero. Similarly, the stream function ψ is odd in the axial direction, since the flow circulates in opposite directions in the lower and upper half of a liquid bridge. Therefore only odd Chebyshev terms $T_{2M+1}(z/b)$ are nonzero in the representation of ψ. Arguments to support the even and odd Chebyshev selections in the representations of vorticity ω_θ and temperature T_0 are determined in a similar way.

Taking advantage of axisymmetry and the axial symmetry, the unique computational domain for the base flow is reduced to $r \in [0,1]$, $z \in [0,b]$ at $\theta = 0$ and is discretized using Gauss-Lobatto collocation grids ($r \times z = NRF \times NZF$ for the flow field and $r \times z = NRT \times NZT$ for the temperature field) given by

$$r_{IF} = \cos\left(\frac{IF * \pi}{2 * NRF}\right) \quad \text{for} \quad IF = 0, 1, 2, ..., NRF, \tag{3.38}$$

$$z_{KF} = \cos\left(\frac{KF * \pi}{2 * NZF}\right) \quad \text{for} \quad KF = 0, 1, 2, ..., NZF. \tag{3.39}$$

These grids weight the finest resolution toward the free surface and the solid boundary, respectively, where it is most needed. A grid dependence study is available in Appendix A.2.

---

[2] Strictly speaking, in the cylindrical coordinate system, "even" in the radial direction is not a valid argument. A rigid derivation requires transforming into a Cartesian coordinate system in a θ cutting plane crossing the mid-axis ($r = 0$). In this plane, ψ is even with respect to the mid-axis. A detailed derivation is available in [Huang, 2009].

Lastly, summation limits in Equations 3.35 to 3.37 are determined by balancing the total number of equations and the degrees of freedom in the Chebyshev polynomial representations. Discretization of the governing equations and boundary conditions are briefly described here. A complete reference is available in Appendix B of [Huang, 2009]. The momentum equation 3.31 is applied at collocation points within the interior, for $r \in [0, 1)$ and $z \in [0, b)$. The stream function – vorticity relationship Equation 3.30 is applied at collocation points over the entire domain $r \in [0, 1]$ and $z \in [0, b]$ including the boundaries. The energy equation 3.32 is applied at collocation points within the interior, for $r \in [0, 1)$ and $z \in [0, b)$. All boundary conditions at $z = b$ are applied using orthogonality. Boundary conditions at $r = 1$ are applied at collocation points for $z \in [0, b)$. Therefore boundary conditions at the top ($z = b$) take precedence over those on the free surface ($r = 1$) when they meet at the corner point $(r, z) = (1, b)$.

Constraints at $r = 0$ and $z = 0$

At $r = 0$, $z = 0$ and $r = z = 0$ the vorticity equation 3.30 and the momentum equation 3.31 reduce to $0 = 0$. The same is true of the boundary conditions for ψ at $z = 0$ (Equation 3.33).[3] Thus, the first nonzero orders of these equations from Taylor series expansions are applied instead, as in [Huang and Houchens, 2011b]. These equations are referred to as *constraints at* $r = 0$ and *constraints at* $z = 0$ in this content.

Applying constraints at $r = 0$ and $z = 0$ greatly enhances the numerical accuracy by enforcing the governing equations where the Gauss-Lobatto grid is coarsest. For example, the flow field is well resolved with $r = 0$ and $z = 0$ constraints applied

[3] Boundary conditions for ψ at $z = b$ are applied using orthogonality rather than at individual collocation points, therefore an expansion is not needed for the conditions at $r = 0$ and $z = b$.

on a $NRF \times NZF = 8 \times 9$ flow grid as shown in Figure 3.5a. For the equivalent resolution without the constraints[4] the stream function ψ contours exhibit unphysical behavior (Figure 3.5b). Note that, even with the slightly finer grid near $r = 1$ and $z = b$, these regions are still less resolved in Figure 3.5b as compared to Figure 3.5a. This is due to insufficient resolution of the interior region, which contains critical details about the flow field even though the velocities are small in this region. Unlike local numerical schemes such as finite element or finite difference methods, global spectral methods weight the solution over the entire domain. Thus the truncation error appears throughout. Even with sufficient resolution to mask this error in the contours associated with larger values of ψ, the nonphysical zero contours persist in the interior, as in Figure 3.5d. With the same resolution and the constraints applied these artifacts disappear as shown in Figure 3.5c.

The Chebyshev polynomial coefficients provide insight to the solution quality. Exponential decay of the coefficients is the sign of the flow field being sufficiently resolved by the truncated series. The stream function ψ coefficients $|A_{0M}|$'s from all four cases in Figure 3.5 are plotted in Figure 3.6. As shown in Figure 3.5a, the flow field appears well resolved on a $NRF \times NZF = 7 \times 8$ grid with $r = 0$ and $z = 0$ constraints applied. The corresponding stream function coefficients (green square markers) support this claim, as they decay by four orders of magnitude overall. In comparison, for the case with a $NRF \times NZF = 8 \times 9$ grid without $r = 0$ and $z = 0$ constraints, the stream function coefficients (blue $\times$ markers) have a tail that is one to

[4] The degrees of freedom for ψ equal the number of A_{LM}'s in Equation 3.35. With $r = 0$ and $z = 0$ constraints, there are $(NRF + 2) \times (NZF + 2)$ equations (including boundary conditions) to match the degrees of freedom for ψ. Without these constraints there are only $(NRF+1) \times (NZF+1)$ equations and the limits on the representation of ψ would need to be reduced by one in each direction.

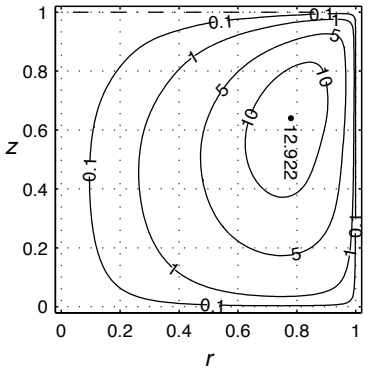

(a) $7 \times 8, 5 \times 5$, WITH $r = 0$ and $z = 0$ constraints, ψ degrees of freedom = 90

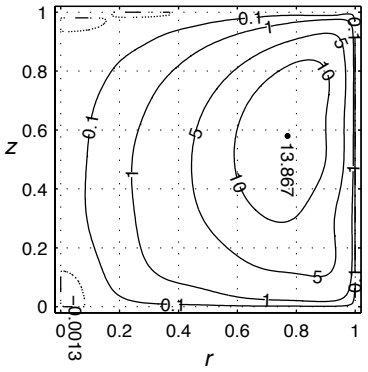

(b) $8 \times 9, 5 \times 5$, WITHOUT $r = 0$ and $z = 0$ constraints, ψ degrees of freedom = 90

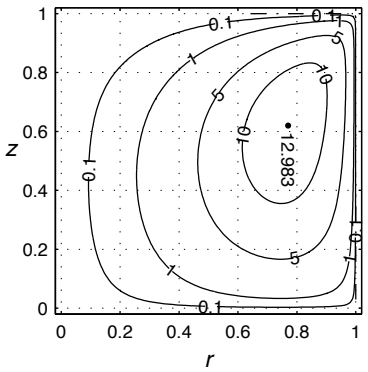

(c) $14 \times 16, 10 \times 10$, WITH $r = 0$ and $z = 0$ constraints, ψ degrees of freedom = 288

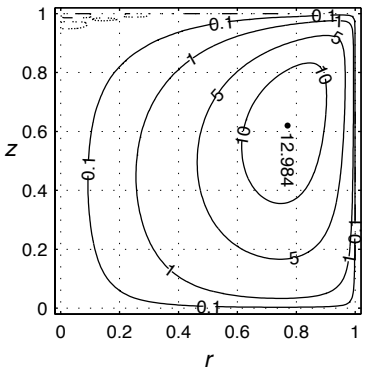

(d) $15 \times 17, 10 \times 10$, WITHOUT $r = 0$ and $z = 0$ constraints, ψ degrees of freedom = 288

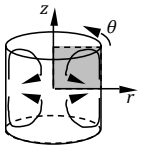

Figure 3.5 : Comparisons of stream function contours demonstrating the numerical improvement achieved by applying $r = 0$ and $z = 0$ constraints for $Pr = 0.02$, at $Re_{FZ} = 1,546.58$, with regularization parameter $\alpha = 400$, no magnetic field, with numbers in subfigure titles representing $NRF \times NZF$, $NRT \times NZT$ [Li et al.,]

two orders of magnitude larger. These large high order Chebyshev terms correspond to the unphysical high frequency oscillations of the flow solution in Figure 3.5b.

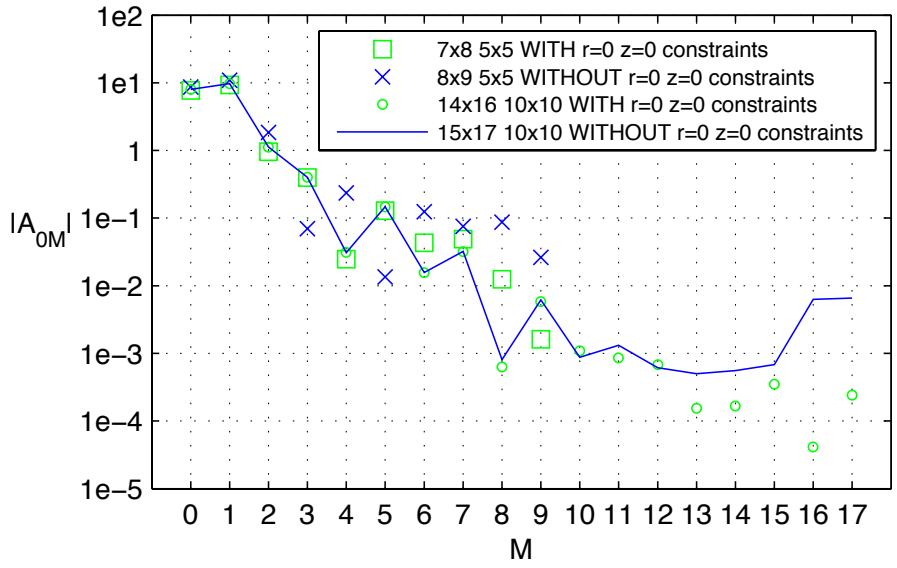

Figure 3.6 : Absolute value of stream function ψ Chebyshev polynomial coefficients $|A_{0M}|$ for all four cases from Figure 3.5 [Li et al.,]

The flow solution is further examined by doubling the grid resolution. With $r = 0$ and $z = 0$ constraints, the flow field (Figure 3.5c) shows very minor changes compared to the case with the coarse grid (Figure 3.5a). The stream function Chebyshev polynomial coefficients (green circle markers in Figure 3.6) decay by an additional one to two orders of magnitude, indicating better solution quality. Without $r = 0$ and $z = 0$ constraints, even if the grid resolution is doubled ($NRF \times NZF = 15 \times 17$, $NRT \times NZT = 10 \times 10$), nonphysical zero stream function contours are not completely eliminated in the interior (Figure 3.5d). The associated Chebyshev polynomial coefficients (blue line in Figure 3.6) have a fairly significant tail with the last two terms having magnitude larger than the smallest term in the 7×8 case with constraints

applied. In summary, the $r = 0$ and $z = 0$ constraints significantly improve solution quality for the same degrees of freedom (and therefore no additional computational cost) and are are thus always applied in the solutions presented here.

Regularization of the Vorticity Singularity

A singularity exists at the corner $(r, z) = (1, b)$ where the free surface and the melting/re-solidifying interface meet. The no-penetration boundary condition $v_{z0} = 0$ at the top $z = b$ boundary (Equation 3.17) implies $\partial v_{z0}/\partial r = 0$ at $(r, z) = (1, b)$. The thermocapillary boundary condition $\partial v_{z0}/\partial r = -F(z)Re_{FZ}\partial T_0/\partial z$ (Equation 3.16) is nonzero at $(r, z) = (1, b)$ due to the nonzero temperature gradient $\partial T_0/\partial z$ at the free surface. Thus, the regularization function $F(z)$ is introduced in the thermocapillary boundary condition to resolve this inconsistency.

This vorticity (velocity gradient) singularity is removed through the regularization function $F(z)$, which decays quickly to 0 as $z \to b$, and remains equal or very close to 1 for the rest of z. Thus the thermocapillary boundary condition is reduced over a small region near $(r, z) = (1, b)$ to let the no-penetration boundary condition $v_{z0} = 0$ take precedence at $(r, z) = (1, b)$. An exponentially decaying function is chosen for $F(z)$ and is used in all solutions in this chapter (repeating Equation 3.18)

$$F(z) = 1 - \exp\left\{-\alpha\left[1 - \left(\frac{z}{b}\right)^2\right]^2\right\}.$$

The regularization parameter α in $F(z)$ determines how much impact the regularization has over $z \in [0, b]$. Smaller values of α smooth out the singularity effectively, but may also change the actual physics by significantly reducing the heat flux distribution along the free surface. Larger values of α alter the physics less. However, if α is too large the weighting factor on the free surface collocation point nearest $z = b$

(and on all other collocation points) will approach 1. In this case the singularity will not be smoothed at all and it will corrupt the global spectral solution. An optimum α is found when increasing α further has no measurable impact on the flow and the singularity is still effectively removed. Regularization dependence studies are included in Appendix A.1.

3.2.3 Base Flow Physics

Here the impacts of the dimensionless parameters on the base flow are discussed. This dimensionless parameters include the thermocapillary Reynolds number Re_{FZ}, the Hartmann number Ha and the Prandtl number Pr.

Marangoni Convection

In the Full-Zone liquid bridge, the flow convection is driven by the Marangoni effect at the free surface. The surface tension is weakest near the mid-plane at $z = 0$ where the temperature is highest. The surface tension is stronger near the melting/re-solidification planes at $z = \pm b$, where the temperature is lowest. Due to this surface tension gradient, fluid near the free surface is pulled away from the mid-plane toward the two ends. The flow hits these two end boundaries, then turns inwards and circulates back to the equatorial plane, forming a pair of "toroids". Mathematically, these donut-shaped, axisymmetric surfaces are stream function iso-surfaces for the base flow – a weightless particle released on one such surface will circulate and always remain on that toroidal surface. In this chapter, the stream function iso-surface in a θ plane is often referred as the stream function contour or a "circulation cell". The name "circulation cell" refers to the shape of a toroidal stream function iso-surface in a θ cutting plane, but in three-dimensions these "circulation cells" are toroidal iso-surfaces.

The intensity of the Marangoni effect (here specifically the thermocapillary effect) is measured by the thermocapillary Reynolds number Re_{FZ} defined as (repeating Equation 3.9)

$$Re_{FZ} = \frac{\rho^* R^* \left|\frac{d\gamma^*}{dT^*}\right| \Delta T^*}{\mu^{*2}}.$$

Figure 3.7 shows the flow field (or at minimum the zero streamlines) for weak to strong Marangoni effects at a fixed Hartmann number $Ha = 50$. Due to the magnetic damping effect, the primary (outermost and strongest) circulation cell is confined near the free surface. This primary circulation cell is also rendered in 3D in Figure 3.7 to show its toroidal structure. Two weaker circulation cells develop in the interior due to a combination of viscous effects and magnetic damping.

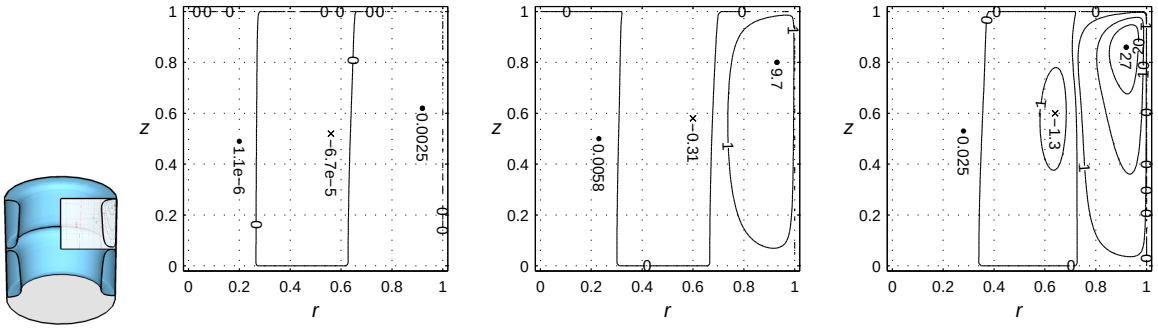

(a) $Re_{FZ} = 1$ (b) $Re_{FZ} = 5,000$ (c) $Re_{FZ} = 21,879.55$

Figure 3.7 : Weak to strong Marangoni convections shown by stream function contours (streamlines). Larger values of Re_{FZ} correspond to stronger Marangoni convection. (Pr=0.02, Ha=50, $NRF \times NZF = 70 \times 100$, $NRT \times NZT = 40 \times 40$, and $\alpha = 1000$) [Huang and Houchens, 2011a]; reprinted with permission.

Stronger Marangoni effects intensify the flow, as indicated by the stream function values in Figure 3.7. The flow is almost stagnant at $Re_{FZ} = 1$, which represents the

limit of no Marangoni driving. The stream function contours at the intermediate value $Re_{FZ} = 5,000$ and high value $Re_{FZ,cr} = 21,879.55$ (the critical thermocapillary number of the first instability, explained in Subsection 3.3.1) show that the flow is most significant within the primary circulation cell near the free surface. The innermost circulation cell is an effectively stagnant interior, which is preferred for many crystal growth applications. Notice that the radial extents of the circulation cells are controlled predominately by the Hartmann number Ha (proportional to the magnetic flux density B_o^*). The Marangoni effect is only a secondary factor on the positions and extents of the circulation cells.

Strong shear flows are observed near the free surface and near the corner $(r, z) = (1, b)$ in the vorticity contours (Figure 3.8a). Because conductive heat transfer is dominant for low Pr fluids, the isotherms (Figure 3.8b) are only slightly bent near the free surface by convection, even with a strong Marangoni convection at $Re_{FZ} = 21,879.55$.

In computing the base flow, Re_{FZ} is ramped up from $Re_{FZ} < 1$, where the flow field is almost stagnant, until the desired value is reached. Solutions at lower Re_{FZ} become initial guesses for larger Re_{FZ} cases. The governing equations and boundary conditions are solved using the Newton-Raphson iterative method. LU decomposition and back substitution is performed using the DGESV routine [Intel®, 2008] in LAPACK [Anderson et al., 1999]. The base flow code is written in FORTRAN 90.

Magnetic Damping

Exposed to the axial static magnetic field, radial flow motions are damped by the electromagnetic body force. Consider the region where the base flow turns inward

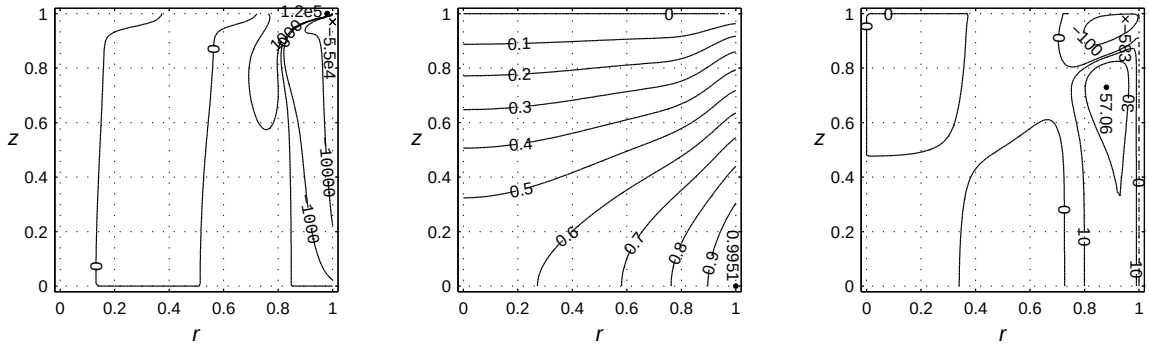

(a) Vorticity ω_θ (b) Temperature T_0 (c) $v_{r0}(= -j_{\theta 0})$

Figure 3.8 : Base flow vorticity, isotherms and radial velocity (equal to the negative azimuthal electric current density in the base state) contours for $Pr = 0.02$ and $Ha = 50$ at $Re_{FZ,cr} = 21,879.55$ (the critical thermocapillary number of the first instability) with $NRF \times NZF = 70 \times 100$, $NRT \times NZT = 40 \times 40$, and $\alpha = 1000$) [Huang and Houchens, 2011a]; reprinted with permission.

near the corner at $(r, z) = (1, b)$. Here the flow motion has a large radial component in the $-\hat{\mathbf{e}}_r$ direction (a negative v_{r0}). Exposed to a magnetic field in $+\hat{\mathbf{e}}_z$ direction, this radial motion induces an electric current density in $+\hat{\mathbf{e}}_\theta$ direction (a positive $j_{\theta 0}$), the negative of which is shown in Figure 3.8c. A Lorentz force $\mathbf{j} \times \mathbf{B} = j_{\theta 0}\hat{\mathbf{e}}_r$ is induced in the $+\hat{\mathbf{e}}_r$ direction, which opposes the radial flow motion in the $-\hat{\mathbf{e}}_r$ direction. The Lorentz force is proportional to the dimensional magnetic flux density B_0^*.

The magnetic damping effect is measured by the Hartmann number (repeating Equation 3.5)

$$Ha = \left(\frac{\sigma^*}{\mu^*}\right)^{\frac{1}{2}} B_o^* R^*,$$

where σ^* and μ^* are electrical conductivity and dynamic viscosity, respectively. Thus Ha measures the electromagnetic force relative to viscous effects. The base flow is

strongly impacted by magnetic damping. Figure 3.9 shows modifications in the base flow under a range of Hartmann number Ha influences. The material properties (Pr) and the heat input (Re_{FZ}) are kept the same in all cases.

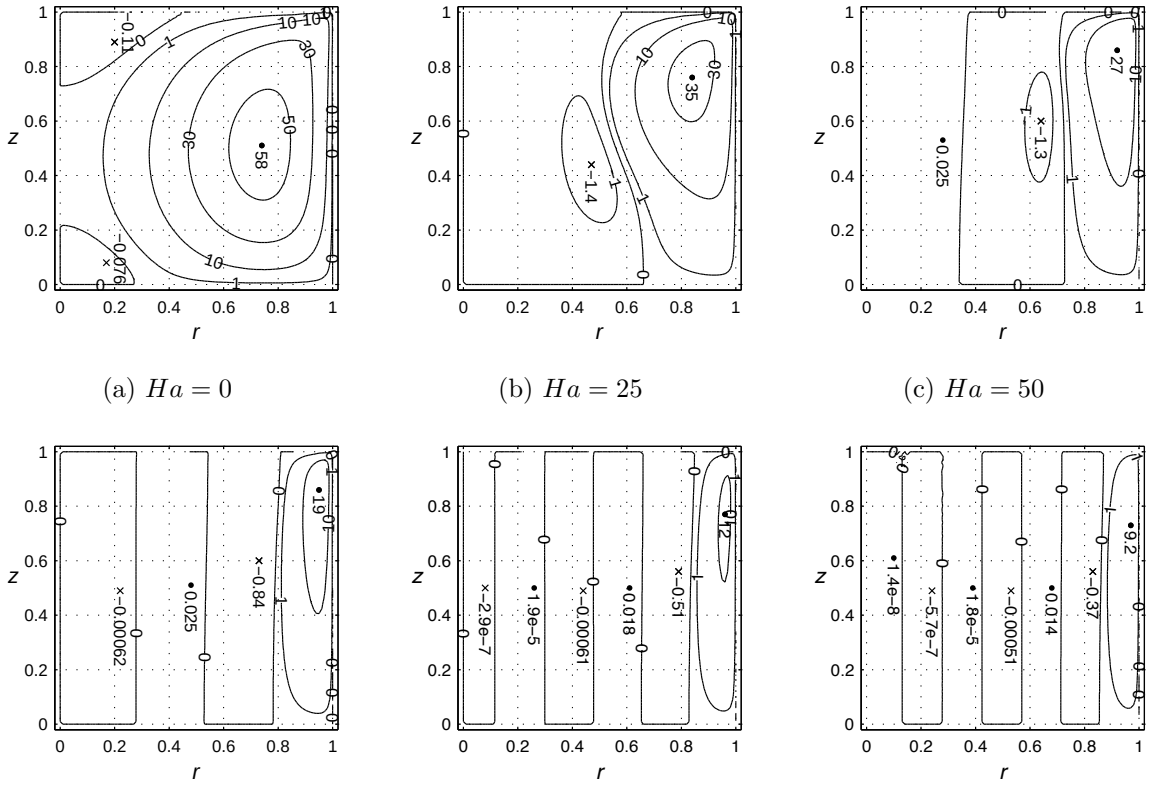

(a) $Ha = 0$ (b) $Ha = 25$ (c) $Ha = 50$

(d) $Ha = 100$ (e) $Ha = 200$ (f) $Ha = 300$

Figure 3.9 : Magnetic damping effect shown by stream function contours. Larger Hartmann numbers Ha correspond to stronger electromagnetic damping ($Pr = 0.02$ and $Re_{FZ} = 21,914.8$ in all cases) [Huang and Houchens, 2011b]; reprinted with permission.

Without magnetic damping ($Ha = 0$), a primary circulation cell develops driven by the Marangoni effect (Figure 3.9a). Flow circulates counterclockwise (in the upper half of the liquid bridge) and extends throughout the domain $r \in [0, 1]$. Small secondary

recirculation cells also emerge in the interior due to strong convection associated with the large Re_{FZ}.[5]

At $Ha = 25$, the magnetic damping weakens the primary circulation cell (as shown by the stream function values) and confines it near the free surface – roughly within $r \in [0.5, 1]$ (Figure 3.9b). This results because the radial flow is damped by the Lorentz force when exposed to an axial magnetic field. To preserve continuity, the flow must turn downward and then circulate back to the mid-plane.

As the magnetic field further intensifies (*i.e.* Ha increases), the primary circulation cell is confined ever more dramatically near the free surface, and more circulation cells develop in the interior as shown by Figures 3.9c to 3.9f. Stream function values indicate flow intensity within that cell. Notice that the most significant flow is always within the primary circulation cell. The maximum or minimum stream function values in each circulation cell drops one to two orders of magnitude from its outer neighbor. This suggests that the interior of the liquid bridge can be made effectively quiescent with a sufficiently strong magnetic field, ideal for crystal growth.

Furthermore, the thickness of the primary (outermost) circulation cell is an important indication of the magnetic damping effect for crystal growth. After a crystal rod is grown, experimentalists will often remove the outermost layer which inevitably develops defects due to the local intense flow. Only the more uniform interior is processed into electro-optical devices. Therefore, the radial contraction of the circulation cells with magnetic damping is very much desired. Figure 3.10 shows the primary circulation cell thickness decays as $Ha^{-0.5096}$ for $Pr = 0.02$, which is very close to the

[5] The value $Re_{FZ} = 21,914.8$ is near the critical value of the first instability at $Ha = 50$ for $Pr = 0.02$. This Re_{FZ} value is well above the critical values for $Ha = 0$ and $Ha = 25$, therefore the actual flow for these cases would be in perturbed, not base flow states.

$Ha^{-0.5}$ decay observed numerically in a Half-Zone over a smaller Ha range [Prange et al., 1999]. Note that the Re_{FZ} is not held constant in this plot, though this is not too important, as the primary cell thickness is a much weaker function of Re_{FZ} than it is of Ha. The primary circulation cell thickness decays slightly faster with Ha for $Pr = 0.001$, as compared to $Pr = 0.02$.

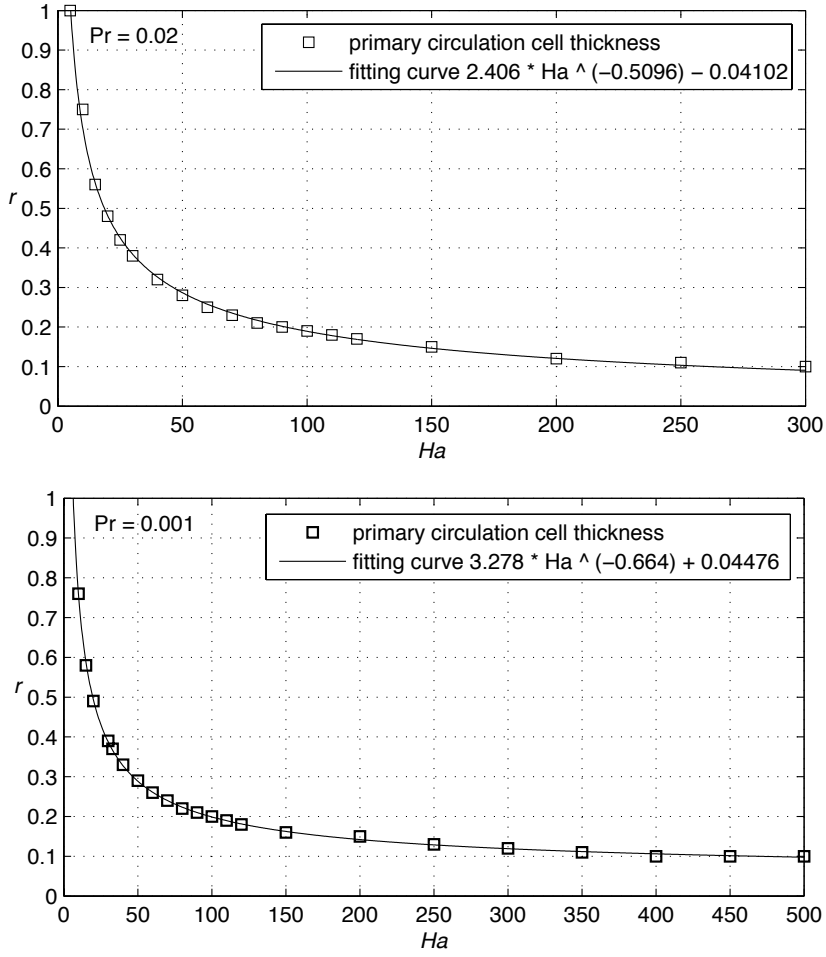

Figure 3.10 : Primary (outermost) circulation cell thicknesses for $Pr = 0.02$ and $Pr = 0.001$ at the $Re_{FZ,cr}$ (the critical thermocapillary number, explained in Subsection 3.3.1) of the first instability [Huang and Houchens, 2011b]; reprinted with permission.

Prandtl Number Effects

The Prandtl number Pr is a material property defined as (repeating Equation 3.6)

$$Pr = \frac{\mu^* c_p^*}{k^*} = \frac{\nu^*}{\alpha^*},$$

The Prandtl number Pr determines the dominant heat transfer mechanism.[6] For a liquid with $Pr < 1$, the thermal boundary layer is thicker than the velocity boundary layer. With a large thermal diffusivity $\alpha^* = k^*/(\rho^* c_p^*)$, heat conducts well. Weak viscus effects (due to a small kinematic viscosity $\nu^* = \mu^*/\rho^*$) limit the influence of the velocity to within a thinner boundary layer, which also limits the convective heat transfer. In summary, heat conduction is dominant for $Pr < 1$ liquids. Molten semiconductors grown by float-zone crystal growth typically have small Pr.

For a liquid with $Pr > 1$, the opposite happens. With a thicker velocity boundary layer, heat is mostly distributed within the fluid by thermal convection. Heat conduction is relatively weak and less-penetrating. Therefore, convective heat transfer is dominant for $Pr > 1$ liquids. Half-Zone liquid bridge experiments usually use transparent fluids with large Pr, such as silicone.

Prandtl number effects are often discussed in crystal growth studies. Small and large Prandtl number fluids exhibit significantly different liquid bridge physics. For example, [Kasperski et al., 2000] first investigated the different characteristics of small and large Pr Full-Zone instabilities. [Levenstam et al., 2001] performed a fairly continuous Pr study using the Half-Zone with a focus on the intermediate Pr range, which bridges the gap between the small and large Pr regimes. [Bouizi

[6] Note that α without the asterisk superscript is the regularization parameter while α^* is the unrelated thermal diffusivity.

et al., 2007] presented Full-Zone instabilities over a wide range of $Pr \in [0.001, 100]$ by three-dimensional nonlinear spectral computations.

This work treats small Pr Full-Zone liquid bridges. Even though heat conduction is dominant for $Pr < 1$, the impact of varying Pr is still non-negligible.

Varying Only Pr, with Ha and Re_{FZ} Held Constant

In the limit of $Pr \to 0$, the heat transfer is purely conductive. The isotherms for $Pr = 10^{-6}$ (Figure 3.11a) closely approximate $Pr \to 0$. The energy equation 3.32 reduces to the heat conduction equation $\nabla^2 T = 0$ and the temperature field decouples from the flow field. In fact, the temperature field for $Pr = 10^{-6}$ is almost unchanged as Ha varies from 0 to 300 because the thermal boundary conditions remain the same (figures not shown). The maximum nondimensional temperature $T_{\max} = 1.0633$ remains constant at $(r, z) = (1, 0)$.

As Pr increases, conductive heat transfer assists to distribute the thermal energy throughout the domain. Figure 3.11b shows that isotherms are bent by convection at $Pr = 0.0667$, compared to $Pr = 10^{-6}$ (Figure 3.11a). $T_{\max}$ is reduced to 0.8102 due to convective heat transfer (while Ha and Re_{FZ} are fixed). Notice that the $T = 0.5$ curve shifts by a large amount compared to $Pr = 10^{-6}$.

Varying the Prandtl number has a less significant impact on the flow field as compared to the effect on the temperature field. In moving from $Pr = 10^{-6}$ to $Pr = 0.0667$, the flow is weakened (Figure 3.11c and 3.11d) due to the weaker thermocapillary driving force resulting from the smaller temperature gradient at the free surface. Otherwise, the cell thicknesses and locations of local extrema change little, primarily because the magnetic damping, proportional to the radial flow velocity, also weakens as the Marangoni convection weakens.

Isotherms:

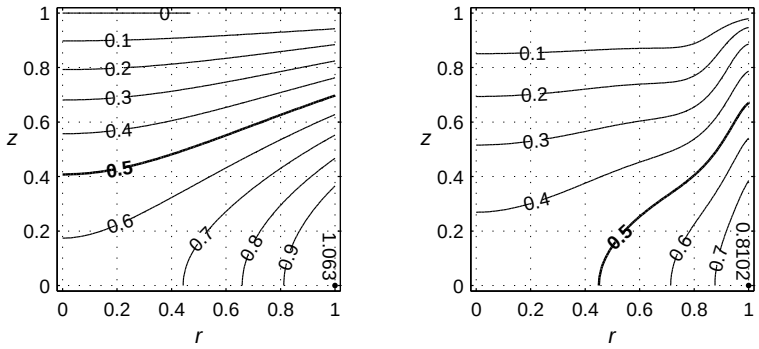

(a) $Pr = 10^{-6}$ (b) $Pr = 0.0667$

Stream function contours:

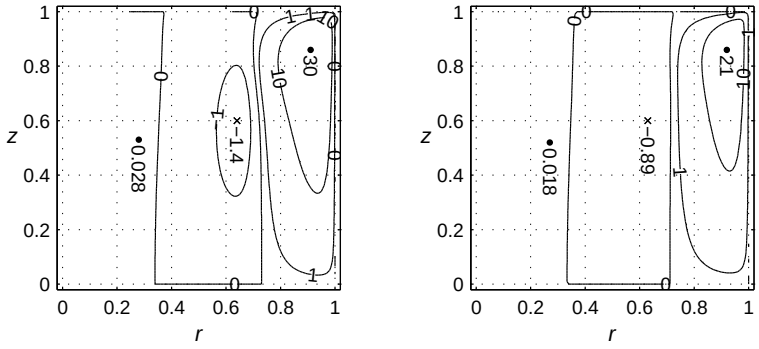

(c) $Pr = 10^{-6}$ (d) $Pr = 0.0667$

Figure 3.11 : Prandtl number Pr effects on the temperature field and the flow field. Smaller Pr corresponds to heat conduction dominance ($Ha = 50$ and $Re_{FZ} = 21,914.8$ in both cases) [Huang and Houchens, 2011b]; reprinted with permission.

Pr Effects under Variation of *Ha*, with Re_{FZ} Held Constant

Nevertheless, variation of the Prandtl number also affects the magnetic damping slightly.

Previously, the classic viscous Reynolds number is defined as (repeating Equation 3.10)

$$Re_{\text{classic}} = \frac{\rho^* V_0^* R^*}{\mu^*},$$

where the choice of velocity scaling $V_0^* = \mu^*/(\rho^* R^*)$ yields $Re_{\text{classic}} = 1$.

Here, for the purpose of showing the actual flow intensity, another viscous Reynolds number is defined based on the *maximum* flow velocity

$$Re_{\text{viscous}} = \frac{\rho^* v_{\max}^* R^*}{\mu^*} = \frac{\rho^* v_{\max} V_0^* R^*}{\mu^*} = v_{\max} \underbrace{Re_{\text{classic}}}_{=1} = v_{\max}. \tag{3.40}$$

In this new scaling, the viscous Reynolds number equals the maximum nondimensional velocity $v_{\max}$ from the computed result. Re_{classic} is defined based on material properties μ^*, ρ^* and melt radius R^*, which are all assumed constant, therefore the newly defined $Re_{\text{viscous}} = v_{\max} Re_{\text{classic}}$ is a proper measurement of the (maximum) flow intensity.

Figure 3.12a shows how this newly defined Re_{viscous} changes with increasing magnetic damping over a range of Pr for fixed Re_{FZ}. In general, Re_{viscous} decreases as Ha increases as a result of magnetic damping (Figure 3.12a). However, the $Pr = 0.01$ curve marks the boundary of two distinct observations for all Pr curves.

For $Pr > 0.01$, Re_{viscous} exhibits an initial increase when Ha increases from 0 to roughly 30. Re_{viscous} then decreases with stronger magnetic damping. Increasing Ha continuously from zero confines the flow into a narrow layer near the free surface, which reduces the effectiveness of convective heat transfer into the interior. Thermal energy

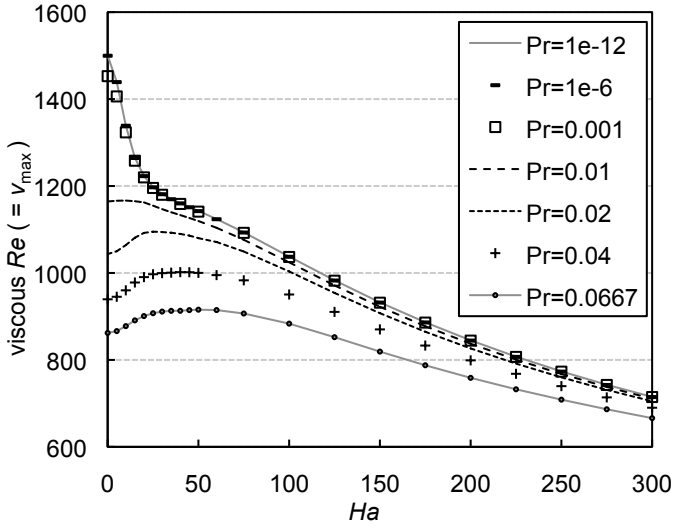

(a) Re_{viscous}

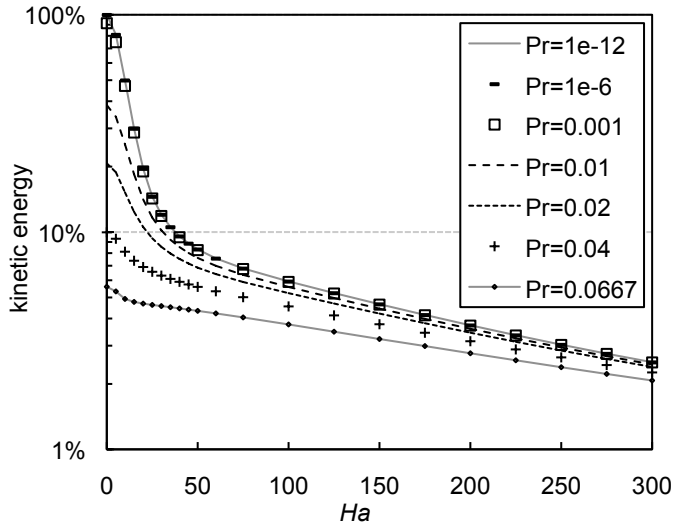

(b) Nondimensional kinetic energy (a semi-log plot)

Figure 3.12 : Effects of Prandtl number and magnetic damping on viscous Reynolds number and nondimensional kinetic energy (Re_{FZ}=21,914.8 in all cases) [Huang and Houchens, 2011b]; reprinted with permission.

is thus better preserved near the free surface and $T_{\max}$ at $(r, z) = (1, b)$ increases as shown in Figure 3.13 for $Pr = 0.02$. Because of the increased temperature difference along the free surface, the thermocapillary driving force is enhanced. As a result, flow at the free surface is accelerated even more (but limited to a narrow layer due to magnetic damping). The maximum nondimensional velocity $v_{\max}$, which always occurs near $(r, z) = (1, b)$, increases. Therefore, $Re_{\text{viscous}} = v_{\max}$ increases initially, before Ha gets too large. Eventually at higher Ha, magnetic damping is sufficiently strong to decrease $Re_{\text{viscous}} = v_{\max}$, even though $T_{\max}$ continues to increase and approach 1.0633 – the value in the limit of no convective heat transfer.

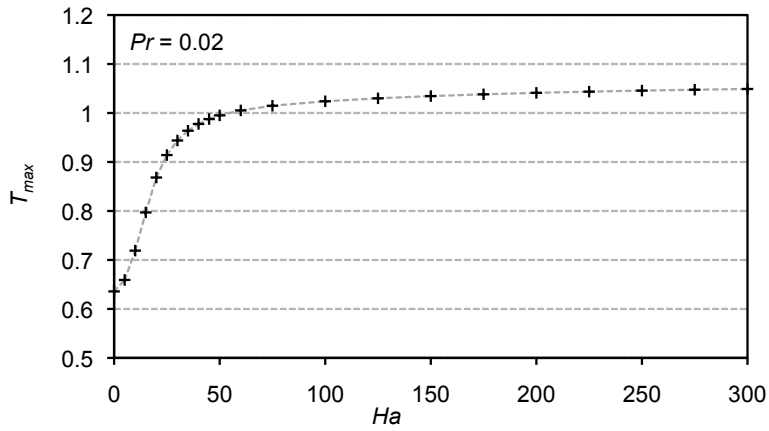

Figure 3.13 : Maximum nondimensional temperature $T_{\max}$ at $(r, z) = (1, b)$ increases with Ha for $Pr = 0.02$, which indicates the thermal energy is better preserved near the free surface at higher Ha (Re_{FZ}=21,914.8 in all cases).

For $Pr < 0.01$, Re_{viscous} always decreases monotonically with increasing Ha. With weak convective heat transfer, the temperature field is effectively decoupled from the flow field and $T_{\max}$ remains almost constant as Ha increases. Thus, increasing Ha has virtually no impact on the thermocapillary effect for $Pr < 0.01$. $Re_{\text{viscous}} = v_{\max}$

decreases monotonically because the flow field is further damped by the Lorentz force at higher Ha.

Furthermore, Table 3.1 summarizes Re_{viscous} at the transition point from the base flow to instabilities (see Subsection 3.3 for discussion about flow instabilities in the liquid bridge). In such definition, it may as well be called the critical viscous Reynolds number $Re_{\text{viscous,cr}}$. $Re_{\text{viscous,cr}}$ increases significantly with Ha, which physically means that, with stronger magnetic damping, the flow can be greatly intensified (but only near the free surface, the interior is damped largely to stagnant) while still maintains the base flow state.

Please note that in this work, the transition point to flow instabilities is still primarily measured by the critical thermocapillary Reynolds number $Re_{FZ,cr}$, because Re_{FZ} is a direct input in flow equations (the thermocapillary boundary condition Equation 3.8, to be precise). On the other hand, the viscous Reynolds number Re_{viscous} is a derived quantity, which is calculated from the flow solution after the transition point is determined.

Lastly, for all values of Pr considered, the nondimensional kinetic energy drops quickly as Ha increases (Figure 3.12b), which demonstrates the effectiveness of magnetic damping. The kinetic energy is computed as the integral of velocity squared over the 2D cylindrical domain with $r \in [0, 1]$ and $z \in [0, b]$.

For a fixed $Re_{FZ}(\propto q^* R^*/k^*)$, the fact that kinetic energy drops as $Pr(= \mu^* c_p^*/k^*)$ increases can be explained as follows. Assume that the dynamic viscosity μ^*, specific heat c_p^* and radius R^* remain unchanged. Increasing Pr corresponds to decreasing the thermal conductivity k^* and consequently a reduction in maximum heat flux q^* (to maintain a constant Re_{FZ}). Because the heat flux is reduced, the thermocapillary driving force is weakened. With less energy pumped into the system, the kinetic

Table 3.1 : Viscous Reynolds number Re_{viscous} based on $v_{\max}$ at the transition point to flow instabilities (measured by the critical thermocapillary Reynolds number $Re_{FZ,cr}$) in the liquid bridge

	$Pr = 0.02$		$Pr = 0.001$	
Ha	$Re_{FZ,cr}$	$Re_{\text{viscous,cr}}$	$Re_{FZ,cr}$	$Re_{\text{viscous,cr}}$
0	1,547	186	1,205	163
25	7,800	542		
50	21,880	1,080	13,015	774
100	61,733	2,143	27,891	1,258
150	105,777	3,037	43,083	1,647
200	153,946	3,873	59,579	2,014
250	204,741	4,646	77,096	2,363
300	259,068	5,396	95,719	2,705
350			115,168	3,036
400			135,437	3,361
450			156,186	3,675
500			177,202	3,976

energy within the melt is reduced as Pr increases.

Also notice that the $Pr = 0.001$, $Pr = 10^{-6}$ and $Pr = 10^{-12}$ curves are virtually identical in Figures 3.12a and 3.12b. This suggests that the $Pr = 0.001$ liquid bridge is a good representation for the limit of $Pr \to 0$, at least over the range $Ha \in [0, 300]$.

3.3 Liquid Bridge Flow Instabilities

The goal of the stability analysis of the liquid bridge is to study the onset of instabilities, specifically 1) the transition point from the base flow state to the first instability, measured by the *critical thermocapillary Reynolds number* $Re_{FZ,cr}$, 2) the flow pattern of the first instability, and 3) the instability mechanism.

By convention, the instability that first alters the base flow state is referred as the *first instability* or *primary bifurcation*. After the flow transitions, it then can become susceptible to a *secondary instability*, then a *tertiary instability etc.*, as the strength of the flow intensifies. This section focuses most on first instabilities that transition from the base flow in small Pr liquid bridges, which are of most relevance to the liquid bridge semiconductor crystal growth community. Higher order instabilities are discussed in Section 3.5.3.

Note that liquid bridges with small compared to large Prandtl numbers have very different instability mechanisms. Liquid bridge flow instabilities for small Pr are *hydrodynamic* in nature, as will be shown. For $Pr < 0.4$, the first instabilities from the base flow state are characterized by three-dimensional, stationary perturbations, rather than time-dependent disturbances [Bouizi et al., 2007]. Within this range, [Houchens and Walker, 2005] further suggested three sub-regimes with different axial symmetries of the perturbations, which were confirmed by [Bouizi et al., 2007], both in Full-Zone

geometries. [Levenstam and Amberg, 1995] and [Leypoldt et al., 2000] found the secondary instability to be three-dimensional and oscillatory in the Half-Zone. This work focuses on flow instabilities of small Pr liquid bridges.

For large Pr liquid bridges, convective heat transfer is dominant and the instability mechanism is *hydrothermal*. The base flow first transitions to oscillatory perturbations (see [Leypoldt et al., 2000] for example). Due to strong thermal convection at high Pr, isotherms are dramatically distorted such that a large temperature gradient exists at the free surface near the top and bottom boundaries. In reality, the melt-solid interfaces deform significantly from rigid planes due to this strong convection. To accurately resolve high Pr liquid bridges, more realistic boundary conditions are needed. High Pr cases are beyond the scope of this study, as they are not relevant to semiconductor crystal growth.

3.3.1 Normal Mode Linear Stability Analysis

The *normal mode linear stability analysis* is a well-known technique for studying flow instabilities.[7] The base flow state is first solved, as in Section 3.2, then infinitesimal perturbations referred to as *instability modes* are introduced into the flow. The flow

[7] Although traditionally been used in hydrodynamic stability studies, the linear stability analysis is recognized in recent decades for failing to match with experiment observation for some flow problems. Mathematically, these problems are governed by matrix or operator lacks an orthogonal basis of eigenvectors, called *non-normal*. First introduced in [Reddy and Trefethen, 1990], the *pseudospectra analysis* provide an alternative for investigating these non-normal matrices and operators. Interested readers are referred to [Trefethen et al., 1993], a classic paper of pseudospectra on hydrodynamic stability, and the *Pseudospectra Gateway* [Embree and Trefethen, 2012] for an introduction of pseudospectra and examples. Nevertheless, Section 3.5 shows that predictions from the linear stability analysis match very well with liquid bridge instability observations from 3D simulation.

is unstable if any perturbation develops to finite magnitude. The flow is stable if all asymptotically small perturbations decay. The flow is neutrally stable, *i.e.* at the transition point from the base flow to instability, if one or more instability modes develop in magnitude and all others decay.

Instability Modes

Normal mode perturbations of the following forms were introduced into the base flow

$$\xi(r,\theta,z,t) = \underbrace{\xi_0(r,z)}_{\text{base flow}} + \underbrace{\varepsilon Real\{\exp(\lambda t + im\theta)\xi_1(r,z)\}}_{\text{perturbation}} \quad \text{for } \xi = v_r, v_z, P, T \text{ and } j_\theta, \tag{3.41}$$

$$\zeta(r,\theta,z,t) = \underbrace{\varepsilon Real\{\exp(\lambda t + im\theta) i\zeta_1(r,z)\}}_{\text{perturbation}} \quad \text{for } \zeta = v_\theta, j_r, j_z \text{ and } \phi, \tag{3.42}$$

where ε is the infinitesimal magnitude of the disturbance. Variables with subscripts 0 and 1 represent base flow and perturbation variables, respectively. Notice that there is no base flow term in Equation 3.42 because $v_{\theta 0} \equiv 0$, $j_{r0} \equiv 0$, $j_{z0} \equiv 0$ and $\phi \equiv 0$ in the base flow solution.

It is crucial to choose instability modes (Equations 3.41 and 3.42) properly such that a wide variety of possible flow instabilities are allowed, while computational costs remain manageable. In the normal mode perturbations used here, any perturbation pattern is allowed in the (r, z) plane, as no limitation is imposed on $\xi_1(r, z)$ or $\zeta_1(r, z)$.

Secondly, similar to the base flow solution, axial symmetry is exploited for numerical efficiency. Perturbations adhere to one of two axial symmetries (Figure 3.14 and Table 3.2). If perturbation variables have the *same* axial symmetry as their corresponding base flow variables, this instability mode is denoted as "symmetric". If perturbation variables have the *opposite* axial symmetry as their corresponding base flow variables, this mode is denoted as "anti-symmetric". Using this symmetry, the

unique computational domain is reduced to $r \in [0, 1]$ and $z \in [0, b]$ and only odd or even Chebyshev polynomials are needed for each variable, in each direction. However, a new code must be developed for each of these two symmetry modes.

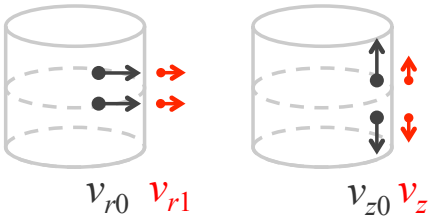

(a) Symmetric mode: perturbation variables have the *same* axial symmetry as their corresponding base flow variables

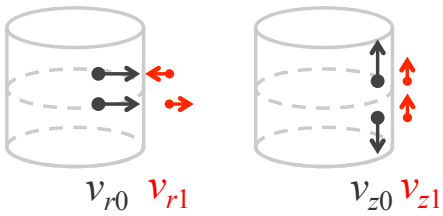

(b) Anti-symmetric mode: perturbation variables have the *opposite* axial symmetry as their corresponding base flow variables

Figure 3.14 : Perturbations adhere to one of two axial symmetries. Variables with subscripts 0 and 1 are for base flow and perturbations, respectively.

Thirdly, perturbations are allowed to vary sinusoidally in θ due to the azimuthal periodicity in the cylindrical domain. The integer valued *azimuthal wave number* m denotes the number of periods of perturbations from $0 \rightarrow 2\pi$. Expensive fully three-dimensional computations are avoided with the caveat that a sufficient range of m must be tracked. For a $Pr = 0.02$ liquid bridge, instability modes for $m = 1$ through 8 were studied in this work. Critical instability modes with $m = 2$ have been observed in similar experimental configurations and confirmed by several numerical studies. For a $Pr = 0.001$ liquid bridge, instability modes were tracked from $m = 1$ to at least $m_{cr} + 4$, where m_{cr} is the critical azimuthal wave number. It has been shown that the base flow is very stable when subject to axisymmetric disturbance modes ($m = 0$), as compared to three-dimensional instability modes ($m > 0$). For

Table 3.2 : Axial symmetries in base flow and perturbations

base flow		perturbations		
			symmetric mode	anti-symmetric mode
variable	axial symmetry	variable	axial symmetry	axial symmetry
v_{r0}	even	v_{r1}	even	odd
$v_{\theta 0}$	$\equiv 0$	$v_{\theta 1}$	even	odd
v_{z0}	odd	v_{z1}	odd	even
P_0	even	P_1	even	odd
T_0	even	T_1	even	odd
j_{r0}	$\equiv 0$	j_{r1}	even	odd
$j_{\theta 0}$	even	$j_{\theta 1}$	even	odd
j_{z0}	$\equiv 0$	j_{z1}	odd	even
ϕ_0	$\equiv 0$	ϕ_1	even	odd

example, Bouizi *et al.* simulated the onset of the transition to an $m = 0$ instability mode at $Re_{FZ} = 11,550$ compared to a much lower $Re_{FZ,cr} = 1,645$ (the *critical thermocapillary Reynolds number*, explained later in this subsection) for $m = 2$ [Bouizi et al., 2007]. therefore $m = 0$ instability modes were not investigated in this work.

In summary, each instability mode exhibits a certain perturbation pattern (eigenmode) in the (r, z) plane, varies sinusoidally for m periods from $\theta = 0 \rightarrow 2\pi$, bears either *symmetric* or *anti-symmetric* axial symmetry, and may or may not oscillate in time (as explained later in this subsection). In this work, for each set of liquid

bridge parameters (Pr and Ha), the number of instability modes allowed was on the order of 10^4 to 10^5. Generally the goal is to find a critical, individual instability mode, though two or more modes can also act as "basis functions" of actual observed instabilities. For example, Section 3.5 demonstrates the transition to a flow instability that is superposition of two linear stability modes.

3.3.2 Numerical Implementation

This subsection presents the numerical methods in the liquid bridge linear stability analysis and explains the underlying physics. Please refer to Appendix D of [Huang, 2009] for formulations and a detailed derivation.

First, the form of the instability modes Equations 3.41 and 3.42 are substituted into the general governing equations 2.32 to 3.4 and boundary conditions 3.7 and 3.8. Terms that satisfy the base flow governing equations cancel out. The normal mode linear stability analysis only investigates the contribution of the linear portion of perturbations (ε terms). All higher order perturbations (ε^2 terms) are neglected.[8]

Then, because continuity, $r-$momentum, $z-$momentum, the energy equation and $\theta-$Ohm's law have the same factor, $\varepsilon Real\{\exp(\lambda t + im\theta)\}$, in every term, and the remaining equations ($\theta-$momentum, conservation of charge, $r-$and $z-$Ohm's law) have the same factor, $i\varepsilon Real\{\exp(\lambda t + im\theta)\}$, in every term, the perturbation magnitude ε, time dependence t, and phase dependence θ are divided out from the governing equations. The linear stability analysis investigates only the onset of

[8] Linear terms in ε represent the perturbations at the onset of instability. These grow in time but obviously should not become infinite in magnitude. As perturbations grow in magnitude (as ε increases), ε^2 terms eventually would become significant and balance the linear contribution of perturbations through *nonlinear saturation*.

instabilities, the perturbation magnitude (ε) is not solved.

Furthermore, because the θ dependence drops out in favor of m, the computational domain is reduced to two-dimensions (r, z). Please note that instability modes are still three-dimensional, with the assumption of sinusoidal variation in θ. A Gauss-Lobatto collocation grid $r \times z = NR \times NZ$ is used for the linear stability analysis. By avoiding expensive 3D computations, this treatment allows finer resolutions in r and z of the flow instabilities (eigenmodes).

Finally, the governing equations and boundary conditions are reformulated in terms of four unknowns: velocity perturbations v_{r1} and v_{z1}, the temperature perturbation T_1, and the electric potential perturbation ϕ_1. To arrive at this 4th order formultion, $v_{\theta 1}$ is solved in terms of v_{r1} and v_{z1} from continuity. Ohm's law is used to describe the electric current density perturbations j_{r1}, $j_{\theta 1}$ and j_{z1} in terms of the electric potential perturbation ϕ_1, and these equations are substituted into conservation of charge, eliminating the electric current density. P_1 is replaced in the $r-$ and $z-$momentum equations using the $\theta-$momentum equation. Readers are referred to Appendix D of [Huang, 2009] for the complete four-variable linear stability analysis formulation.

As explained in Subsection 3.3.1, two codes were developed for the *symmetric* and *anti-symmetric instability modes*, respectively, so that the computational domain is further reduced to $r \in [0, 1]$ and $z \in [0, b]$. For the *symmetric mode*, the four unknowns are expanded using Chebyshev polynomials as

$$v_{r1}\left(r, \frac{z}{b}\right) = r^{m-1} \sum_{L=0}^{NR+1} \sum_{M=0}^{NZ} \mathcal{A}_{LM} T_{2L}(r) T_{2M}\left(\frac{z}{b}\right), \tag{3.43}$$

$$v_{z1}\left(r, \frac{z}{b}\right) = r^{m} \sum_{L=0}^{NR} \sum_{M=0}^{NZ+1} \mathcal{B}_{LM} T_{2L}(r) T_{2M+1}\left(\frac{z}{b}\right), \tag{3.44}$$

$$T_1\left(r, \frac{z}{b}\right) = r^{m} \sum_{L=0}^{NR} \sum_{M=0}^{NZ} \mathcal{C}_{LM} T_{2L}(r) T_{2M}\left(\frac{z}{b}\right), \tag{3.45}$$

$$\phi_1\left(r,\frac{z}{b}\right)=r^m\sum_{L=0}^{NR}\sum_{M=0}^{NZ}\mathcal{D}_{LM}T_{2L}(r)T_{2M}\left(\frac{z}{b}\right). \tag{3.46}$$

For the *anti-symmetric mode*, the four unknowns are expanded as

$$v_{r1}\left(r,\frac{z}{b}\right)=r^{m-1}\sum_{L=0}^{NR+1}\sum_{M=0}^{NZ}\mathcal{A}_{LM}T_{2L}(r)T_{2M+1}\left(\frac{z}{b}\right), \tag{3.47}$$

$$v_{z1}\left(r,\frac{z}{b}\right)=r^{m}\sum_{L=0}^{NR}\sum_{M=0}^{NZ+1}\mathcal{B}_{LM}T_{2L}(r)T_{2M}\left(\frac{z}{b}\right), \tag{3.48}$$

$$T_1\left(r,\frac{z}{b}\right)=r^{m}\sum_{L=0}^{NR}\sum_{M=0}^{NZ}\mathcal{C}_{LM}T_{2L}(r)T_{2M+1}\left(\frac{z}{b}\right), \tag{3.49}$$

$$\phi_1\left(r,\frac{z}{b}\right)=r^{m}\sum_{L=0}^{NR}\sum_{M=0}^{NZ}\mathcal{D}_{LM}T_{2L}(r)T_{2M+1}\left(\frac{z}{b}\right). \tag{3.50}$$

The degrees of freedom of each Chebyshev polynomial representation are set by the summation limits in Equations 3.43 to 3.50 and must match the number of equations applied on the Gauss-Lobatto collocation grid. All governing equations and boundary conditions reduce to $0=0$ at $r=0$ and $z=0$. Their leading order nonzero terms from Taylor series expansions are applied as constraints at $r=0$ and $z=0$, similar to base flow treatment in Subsection 3.2.2.

Each perturbation variable bears even or odd "radial symmetry" under the assumption of sinusoidal variation in θ. This "radial symmetry" refers to the symmetry within the plane consisting of θ and $\theta+\pi$ planes in the cylindrical coordinate system. Take $m=1$, for example. Perturbations vary *one* sinusoidal period from $\theta=0\rightarrow 2\pi$. Therefore, each perturbation variable in θ and $\theta+\pi$ planes are in the opposite direction and of the same magnitude. The azimuthal velocity perturbation is $v_{z1}(\theta)=-v_{z1}(\theta+\pi)$. In other word, v_{z1} has *odd* radial symmetry for $m=1$, which agrees with the *odd* representation $v_{z1}\propto r^1\sum_{L=0}^{NR}T_{2L}(r)$ (Equations 3.44 and 3.48). Similarly, the radial velocity perturbation is $v_{r1}(\theta)=-v_{r1}(\theta+\pi)$. However, in the θ

and $\theta+\pi$ combined plane, $v_{r1}(\theta)$ and $v_{r1}(\theta+\pi)$ point to the *same* direction.[9] Therefore v_{r1} has *even* radial symmetry for $m = 1$, which agrees with the *even* representation $v_{r1} \propto r^0 \sum_{L=0}^{NR+1} T_{2L}(r)$ (Equations 3.43 and 3.47).

With radial and axial symmetries applied, the storage requirements for the perturbation variables are greatly reduced, so that finer grids can be used to investigate liquid bridge flow instabilities. With even or odd radial symmetry, only even or odd Chebyshev term coefficients are non-zero. Thus only half of radial Chebyshev terms, *i.e.* $T_{2L}(r)$ terms, appear in Equations 3.43 to 3.50. Therefore, a representation with NR radial terms in this work is equivalent to a representation with $NR \times 2$ terms if no radial symmetry is assumed. Similarly, with the axial symmetry, only half of axial Chebyshev terms, *i.e.* $T_{2M}(z/b)$ or $T_{2M+1}(z/b)$, present in Equations 3.43 to 3.50. The NZ axial terms for $z \in [0, b]$ in this work are equivalent to a representation with $NZ \times 4$ terms for $z \in [-b, b]$ if no axial symmetry is assumed. Note that with radial and axial symmetries applied, although less storage is needed for each test run, two code are developed and executed, one for symmetric and one for anti-symmetric instability modes, respectively. On top of that, each azimuthal wave number m requires a separate test run. The radial and axial symmetries assumption does not necessarily save on total computational cost. However, aside from better refined perterbation fields, it also allows use of finer grids within computer memory limitations. After discretization, the linear stability analysis is governed by a generalized eigenvalue problem

$$\underline{\underline{\mathbf{AM}}}\,\underline{\mathbf{x}} = \lambda\,\underline{\underline{\mathbf{BM}}}\,\underline{\mathbf{x}}, \tag{3.51}$$

[9] When combining cylindrical planes θ and $\theta + \pi$ into one Cartesian plane, one of these two planes switches its radial direction to align with the other plane.

where $\lambda = \lambda_r + i\lambda_i$ are eigenvalues.

Instability modes can be examined quantitatively by expanding Equation 3.41 as

$$\xi = \xi_0 + \varepsilon \exp(\lambda_r t)[\cos(\lambda_i t + m\theta)\xi_{1,r} - \sin(\lambda_i t + m\theta)\xi_{1,i}], \tag{3.52}$$

where $\xi_1 = \xi_{1,r} + i\xi_{1,i}$. If any $\lambda_r > 0$, the corresponding perturbation grows in time, the base flow transitions to instability. If all $\lambda_r < 0$, perturbations decay in time and the base flow is stable when subject to these perturbations. If one $\lambda_i = 0$ and all other $\lambda_r < 0$, the base flow is at the neutral transition point to instability.[10]

Furthermore, instability modes may oscillate in time (referred as *periodic or oscillatory instability modes* in this work). The frequency of a periodic instability mode is $\lambda_i/2\pi$, as suggested in Equation 3.41. Instability modes with $\lambda_i = 0$ do not oscillate with time (referred as *stationary instability modes*).

Finally, at the onset of the instability, *i.e.* $t = 0$, Equation 3.52 simplifies to

$$\xi = \xi_0 + \varepsilon[\cos(m\theta)\xi_{1,r} - \sin(m\theta)\xi_{1,i}]. \tag{3.53}$$

Equation 3.53 describes the spatial distribution of an instability mode. The perturbation is $\pm\xi_{1,r}(r,z)$ in the θ planes, where $\cos(m\theta) = \pm 1$ and $\sin(m\theta) = 0$. The perturbation is $\mp\xi_{1,i}(r,z)$ in the θ planes, where $\sin(m\theta) = \pm 1$. Between these planes, the perturbation varies sinusoidally in θ.

The analysis for $\zeta(r,\theta,z,t)$ is similar to that for $\xi(r,\theta,z,t)$, but shifted by a factor of i such that the matrices in the eigenvalue problem are purely real.

---

[10] Due to numerical artifacts, some "spurious eigenvalues" emerge in the generalized eigenvalue problem Equation 3.51 bearing no physical meaning regarding system stability. It is crucial to identify and separate these from the remaining legitimate eigenvalues to correctly predict the onset of instability. Please refer to Appendix A.3 for identifying these spurious eigenvalue modes.

Critical Thermocapillary Reynolds Number

The *critical thermocapillary Reynolds number* $Re_{FZ,cr}$ is the quantitative measure of the first instability, indicating the transition point from base flow to perturbed flow. Re_{FZ} measures the thermocapillary driving effect intensity. For each instability mode, a transition point can be found by increasing Re_{FZ} until $\lambda_r = 0$ for this mode. The first instability occurs when one $\lambda_r = 0$ (or one complex pair has $\lambda_r = 0$) and all other $\lambda_r < 0$. This leading eigenvalue mode with $\lambda_r = 0$ is the critical instability mode. The Re_{FZ} associated with the first instability is denoted as the *critical thermocapillary Reynolds number* $Re_{FZ.cr}$.

Finding the $Re_{FZ,cr}$ is an iterative process, because Re_{FZ} resides in the boundary condition. For each instability mode, starting from a stable $Re_{FZ,s}$ (with leading $\lambda_r < 0$) and an unstable $Re_{FZ,u}$ (with leading $\lambda_r > 0$), an approximation $Re_{FZ,3}$ to the critical value is predicted using the *regula falsi* method. The new leading λ_r corresponding to $Re_{FZ,3}$ is computed using the *shifted inverse iteration method*. The $Re_{FZ,3}$ then replaces either $Re_{FZ,s}$ or $Re_{FZ,u}$. In this way the bounds on the neutrally stable Re_{FZ} are narrowed through iterations until convergence. The base flow code and linear stability analysis code are written in FORTRAN 90.

Finally, note that an instability mode with a neutral Re_{FZ} above $Re_{FZ,cr}$ does not necessarily represent an actual transition at such Re_{FZ}. If the base flow is superimposed with the first instability (with proper perturbation magnitude ε), then this is deemed a new base state. Based on this "new base flow state", another linear stability analysis is needed to search for secondary or weakly nonlinear instabilities. However, these slightly stable instability modes provide great insight into potential critical instabilities of similar test conditions. In particular, two competing instability modes are observed in 3D simulations in Section 3.5. It is shown that these correspond

to two distinct linear instability modes.

3.3.3 Instabilities and Magnetic Damping

Here the details of a few representative linear stability cases are presented, first without and then with magnetic damping. Then the entire neutral stability curve is presented for $Pr = 0.02$ and $Pr = 0.001$ cases over the range of Ha studied.

Particle Path of a Representative First Instability for $Ha = 0$

Figure 3.15 shows a streamline in the base flow (black) and the particle path of the first instability (grey). In the base flow state, a weightless fluid particle released at the starting point circulates on the black closed path (*i.e.* the stream function contour) within a fixed θ plane. Above the first instability, a particle released at the same starting point changes its "orbiting radius" as it circulates, while oscillating within a $\theta = \pi/m$ wedge.[11]

Furthermore, the disturbed flow motion in the mid-plane is shown by arrows in the $z = 0$ plane of Figure 3.15. Its dominant radial flow motion is due to the circulation from the liquid bridge interior back to the free surface. Please also notice that perturbed flow crosses the mid-plane into the other half of the liquid bridge.[12] In this example, the instability mode is anti-symmetric ($v_{\theta 1} = 0$ is odd from Table 3.2), therefore the flow at $z = 0$ has no azimuthal component ($v_{\theta 1} = 0$ at $z = 0$).

---

[11] In Figure 3.15 the path line of the first instability is cut off intentionally at the "end" point to better show its spiral structure.

[12] In contrast, the Half-Zone model assumes a no-slip, no-penetration mid-plane.

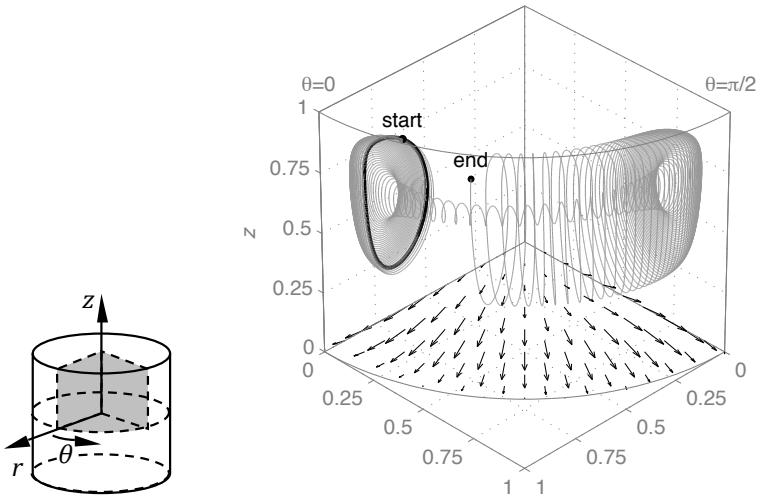

Figure 3.15 : Streamline in the base flow (black closed path) and particle path of the first instability (grey spiral path); disturbed flow (vectors) at the mid-plane (Pr=0.02, Ha=0 at $Re_{FZ,cr}$=1546.58, stationary anti-symmetric disturbances with $m = 2$, flow grid $r \times z = 35 \times 45$, temperature grid $r \times z = 30 \times 30$, linear stability grid $r \times z = 28 \times 28$, $\alpha = 300$, perturbation versus base flow maximum magnitude ratio 5%) [Huang and Houchens, 2011b]; reprinted with permission.

Eigenfuctions of a Representative First Instability for $Ha = 50$

To demonstrate instabilities with magnetic damping in low Pr liquid bridges, results at $Pr = 0.02$ and $Ha = 50$ are shown. Tests at $Pr = 0.02$, the value for molten silicon, are common in the literature allowing for easy comparison. At $Ha = 50$ the flow is not confined excessively in r, allowing for easy visualization of important features.

At $Pr = 0.02$ and $Ha = 50$, the base flow first transitions to a stationary (not periodic), three-dimensional disturbance with azimuthal wave number $m = 4$, and with axial symmetry opposite to the base flow components (the "anti-symmetric mode") at the critical $Re_{FZ,cr} = 21,879.55$.

Velocity disturbances circulate across the mid-plane breaking the axial symmetry and fill the axial extent of the liquid bridge (Figure 3.16a). The most significant velocity perturbations are within the primary cell and outer portion of the secondary cell. In the $\theta = 0$ plane, the upper primary cell center is pushed up and inward, while the lower primary cell center is pushed up and outward. The base flow is mostly reinforced for $z > 0$ and opposed for $z < 0$ by the perturbations in the $\theta = 0$ plane.

Due to the nature of the azimuthal wave, the choice of the $\theta = 0$ plane is arbitrary, and perturbations vary in θ as sinusoidal functions. For example, for $m = 4$, v_{r1} and v_{z1} are maximum at $\theta = 0$, zero at $\theta = \pi/8$, maximum with opposite direction at $\theta = \pi/4$, zero at $\theta = 3\pi/8$ and maximum at $\theta = \pi/2$, etc. Perturbation magnitudes are normalized arbitrarily and should not be compared with base flow magnitudes. The azimuthal velocity perturbation $-v_{\theta 1}$ is shown at $\theta = \pi/8$, where it has maximum magnitude (Figure 3.16c).

As predicted by Ohm's Law, the electric current perturbations and the electric potential perturbations (Figure 3.16e) develop due to velocity perturbations. For example, near the free surface, $j_{r0} = j_{r1} = 0$ and $v_{\theta 1} \neq 0$ (Figure 3.16c). Thus a non-zero electric potential gradient $\partial\phi/\partial r$ is sustained to satisfy the radial component of the Ohm's Law $j_r = -\partial\phi/\partial r + v_\theta$.

The temperature and flow perturbations are plotted on the free surface to investigate the instability mechanism (Figure 3.16b). Perturbation flows are observed from cold to hot spots (for example, near $z = 0.8$), exactly opposite to the Marangoni effect. Also the temperature perturbations are too weak to trip flow instabilities. Combined, these suggest the disturbance is hydrodynamic rather than hydrothermal in nature.

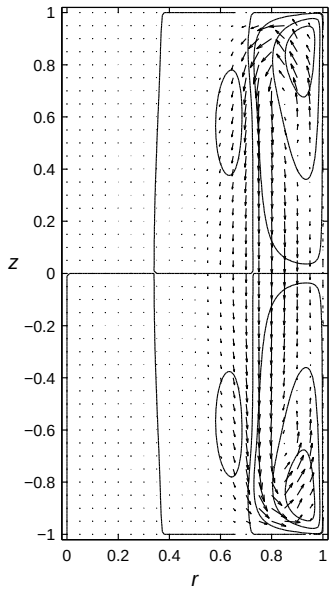

(a) Velocity perturbations (vectors) superimposed on base flow stream function contours in $\theta = 0$ plane

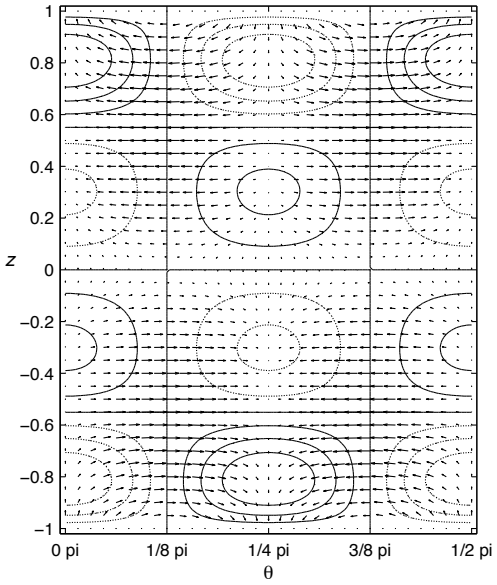

(b) Velocity perturbations (vectors) and temperature perturbations (hot - solid contours, cold - dotted contours) on the free surface

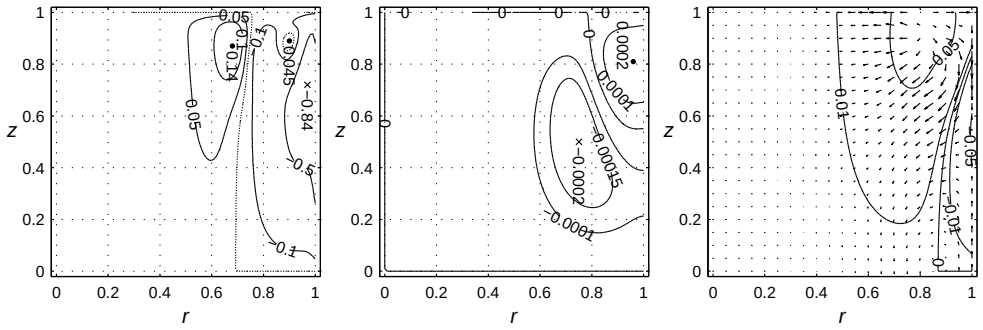

(c) Azimuthal velocity perturbations $-v_{\theta 1}$ in $\theta = \pi/8$ plane (dotted contours: $v_{\theta 1} = 0$)

(d) Temperature perturbations T_1 in $\theta = 0$ plane

(e) $(-j_{r1}) + (-j_{z1})$ vectors superimposed on $-\phi_1$ contours in $\theta = \pi/8$ plane

Figure 3.16 : First instability for $Pr = 0.02$ and $Ha = 50$ at $Re_{FZ,cr} = 21,879.55$ (flow grid $r \times z = 70 \times 100$, temperature grid $r \times z = 40 \times 40$, linear stability grid $r \times z = 40 \times 60$, $\alpha = 1000$) [Huang and Houchens, 2011a]; reprinted with permission.

Critical Curves of First Instability

The first instability is summarized by the critical curves in Figure 3.17 for $Pr = 0.02$ and $Pr = 0.001$. Critical curves mark transition points, measured by $Re_{FZ,cr}$'s, from base flow to instability over a wide range of Ha. The Full-Zone liquid bridge is in the base flow state below the critical curve. The flow transitions to the first instability above the critical curve.

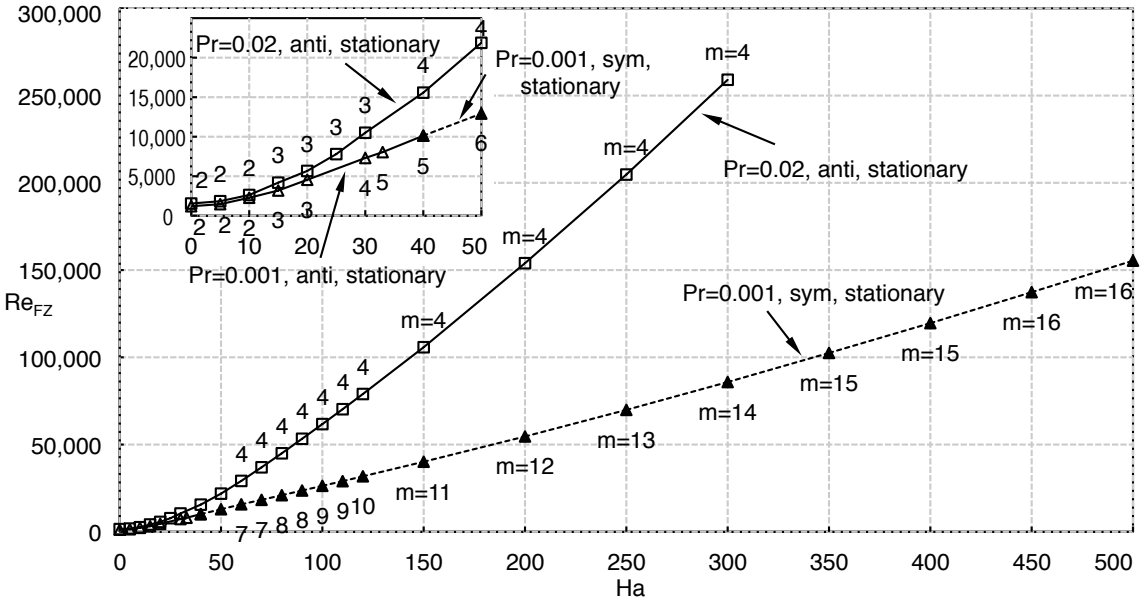

Figure 3.17 : First instability critical curves for $Pr = 0.02$ and $Pr = 0.001$ Full-Zone liquid bridges [Huang and Houchens, 2011b]; reprinted with permission. Complete data is listed in [Huang, 2009].

$Pr = 0.02$ (property of molten silicon) liquid bridges are commonly studied in the literature. By strengthening the magnetic field flux intensity from $Ha = 0 \rightarrow 300$, $Re_{FZ,cr}$ increases two orders of magnitude, as shown in Figure 3.17. When exposed to stronger magnetic fields, more driving energy must be fed in before the flow trips to

an instability.

Magnetic damping not only suppresses the onset of instabilities, but also changes the type of first instability. Numerical labels above the $Pr = 0.02$ critical curve are the critical azimuthal wave numbers m_{cr}'s at these points. Disturbed flow circulates in the azimuthal direction within each of $2m$ wedges. Without magnetic damping ($Ha = 0$), $m_{cr} = 2$ (Figure 3.18). The first instability changes to $m_{cr} = 3$ between $Ha \in [15, 30]$, then $m_{cr} = 4$ from $Ha = 40$ to at least the upper limit $Ha = 300$ tested in this work. The applied axial magnetic field confines most of the Marangoni flow near the free surface. Higher wave numbers indicate flow circulations over smaller azimuthal distances. Here these azimuthal distances remain comparable with the contracted radial extent of the outermost circulation cell. Nevertheless, the first instability for $Pr = 0.02$ Full-Zone liquid bridge is always stationary and in the anti-symmetric disturbance mode for $Ha \in [0, 300]$.

The first instability critical curve for $Pr = 0.001$, representing $Pr \to 0$, effectively marks the lower limit of all critical curves (Figure 3.17). According to [Houchens, 2005], at $Ha = 0$ the $Re_{FZ,cr}$ for $Pr = 10^{-10}$ is less than 1% smaller than $Re_{FZ,cr}$ for $Pr = 0.001$. The $Pr = 0.001$ curve is qualitatively similar to the $Pr = 0.02$ curve, with the difference that the "symmetric disturbance mode" becomes critical beyond $Ha = 40$ for $Pr = 0.001$ until at least the upper limit $Ha = 500$ tested in this work.

For the same Ha, $Re_{FZ,cr}$ for $Pr = 0.001$ is well below that for $Pr = 0.02$. The definition of Pr and Re_{FZ} are important reasons among others. Because $Pr \propto 1/k^*$ (Equation 3.6), a small Pr corresponds to large thermal conductivity k^*. Large k^* leads to a small Re_{FZ}, due to $Re_{FZ} \propto \Delta T^* \propto 1/k^*$ (Equation 3.9).

The critical curve is the lower limit of all *neutral stability branches*. For each instability mode (some wave number m, symmetric or anti-symmetric mode, and

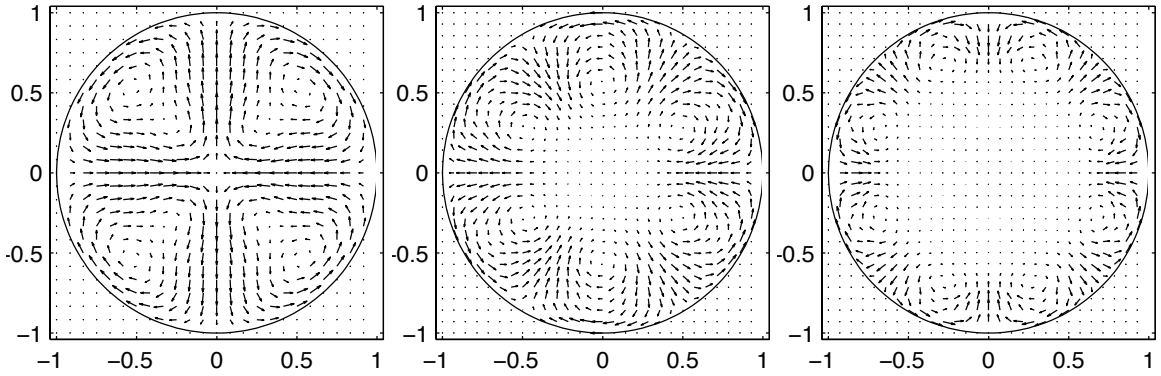

(a) $m_{cr} = 2$ $(Ha = 0, z = 0.5)$ (b) $m_{cr} = 3$ $(Ha = 20, z = 0.7)$ (c) $m_{cr} = 4$ $(Ha = 50, z = 0.8)$

Figure 3.18 : Magnetic damping changes the critical azimuthal wave number m_{cr} of first instability (flow disturbances at cross-sections of $Pr = 0.02$ liquid bridge plotted at z's that best reveal their circulation patterns) [Huang and Houchens, 2011a]; reprinted with permission.

stationary or oscillatory perturbation) and a fixed Ha, the transition point from the base flow to such instability mode, measured by a neutral stable Re_{FZ}, can be found. The neutral stable Re_{FZ} *vs.* Ha curve is referred as the *neutral stability branch* for this instability mode.

Figure 3.19 shows an example of neutral stability branches for the $Pr = 0.02$ liquid bridge. It provides insight into how the critical mode switches from $m = 2$, 3 to 4. But note that the flow is no longer in the base flow state above the critical curve. Therefore neutral stability branches above the critical curve are, at best, qualitative indicators of the other types of modes that may follow the first instability.

Critical instability curves of the liquid bridge help determine sufficient field strengths necessary to avoid the structural imperfections in grown crystals caused by the onset of three-dimensional or oscillatory flow.

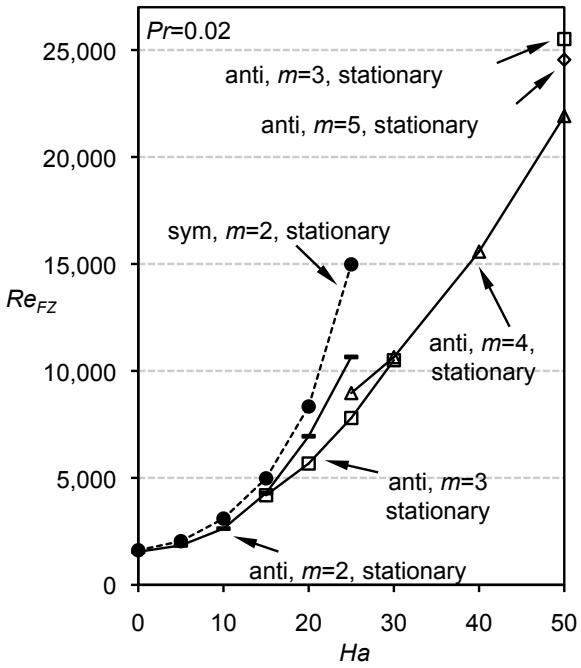

Figure 3.19 : Some neutral stability branches for $Pr = 0.02$ and $Ha \in [0, 50]$ [Huang and Houchens, 2011b]; reprinted with permission. Complete neutral stability data and figures for $Pr = 0.02$ and $Pr = 0.001$ are available in [Huang, 2009].

Validation with Literature

To the author's knowledge, only a few studies on liquid bridge instability with magnetic damping have been published. The Full-Zone instability with magnetic damping is compared with a similar configuration: a Half-Zone with a non-deformable free surface, with unit height to radius aspect ratio, exposed to a static axial magnetic field [Prange et al., 1999]. For $Pr = 0.02$ and $Ha \in [0, 25]$, the first instability is predicted to be stationary and three-dimensional in both configurations. The neutral stability curves are compared in Figure 3.20, with Re_{FZ} renormalized to a representative Re_{HZ} value. This renormalization is necessary due to different nondimensionalizations in these two models. The Full-Zone thermocapillary Reynolds number Re_{FZ} is multiplied by the

maximum nondimensional temperature T_{max} to compare with the Half-Zone Re_{HZ}. The $m = 2$ neutral stability curves from this work and from [Prange et al., 1999] show very similar behavior. The stabilization introduced by the no-slip no-penetration mid-plane in the Half-Zone accounts for its higher critical Re_{HZ} values. Therefore, more energy is needed to trip instabilities in the Half-Zone. However, the critical mode transition from $m = 2$ to $m = 3$ was not observed in this Half-Zone model.

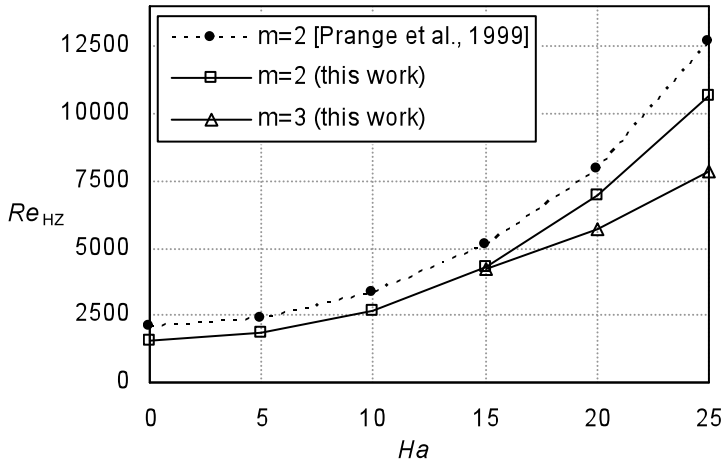

Figure 3.20 : Comparison of critical instability curves with Half-Zone results [Prange et al., 1999] for $Pr = 0.02$, where $Re_{HZ} = Re_{FZ} \times T_{max}$ for the Full-Zone [Huang and Houchens, 2011a]; reprinted with permission.

Readers may have noticed the subscript HZ in Re_{HZ} which refers to the Half-Zone. The thermocapillary Reynolds number Re_{HZ} and Re_{FZ} is defined as (repeating Equation 3.9)

$$Re_{FZ,HZ} = \frac{\rho^* R^* \left|\frac{d\gamma^*}{dT^*}\right| \Delta T^*}{\mu^{*2}}.$$

The difference between the Half-Zone Re_{HZ} and the Full-Zone Re_{FZ} is in the characteristic temperature difference ΔT^*. In the Full-Zone $\Delta T^* = q^* R^*/k^*$. In the Half-Zone

ΔT^* is the temperature difference between the heated and cooled bounding disks. Furthermore, the no-slip and no-penetration heated plane in the Half-Zone introduces extra flow stabilization compared to the "free" mid-plane in the Full-Zone. Therefore, Half-Zone instabilities are tripped at stronger Marangoni convection compared to in the the Full-Zone. Due to above differences, quantitative comparison between critical thermocapillary Reynolds numbers Re_{HZ} and Re_{FZ} (at the onset of instabilities) is less meaningful without understanding of the distinctions between the Half-Zone and the Full-Zone (discussed in Subsection 3.1.1).

Despite the lack of moderate Ha results in the existing literature, liquid bridge instability without magnetic damping ($Ha = 0$) has been benchmarked extensively in the crystal growth research community. Although far from a complete collection, Tables 3.3 and 3.4 summarize results from different research groups using various numerical methods. Some slight differences in configurations are noted.

Full-Zone instability from this work is compared qualitatively with Half-Zone results in Table 3.3. All studies for $Ha = 0$ and $Pr \leq 0.02$ predict the first instability to be stationary with an azimuthal wave number of 2. Quantitative comparisons also provide insights, provided Re_{FZ} is scaled using $Re_{HZ} = Re_{FZ} \times T_{max}$. The Half-Zone $Re_{HZ,cr}$'s are expected to be larger than the Full-Zone $Re_{FZ,cr}$, as explained earlier in this subsection. Some second instability Re_{HZ} values are also listed for comparison.

Full-Zone studies in recent years give more consistent results. The Full-Zone studies listed in Table 3.4 predict the same first instability mode and very similar $Re_{FZ,cr}$ values. Slightly different configurations (for example, variations in heat flux distributions) account for the small differences in results. As Pr decreases, $Re_{FZ,cr}$ also decreases for reasons explained in Subsection 3.2.3. $Re_{FZ,cr} = 1205$ for $Pr = 0.001$ appears to effectively mark the lower $Re_{FZ,cr}$ limit for $Pr \to 0$, at least for $Ha = 0$.

Table 3.3 : Comparison of the first instability with Half-Zone studies in the literature ($Ha = 0$ and unit height-to-radius aspect ratio. The Marangoni number $Ma = Re_{HZ} \times Pr$ is also commonly used in literature. Some second instabilities are listed for reference) [Huang and Houchens, 2011a]; reprinted with permission.

Pr	Re_{HZ}	Ma	instability mode	features and numerical methods
0.02	1548	30.95	stationary, $m = 2$	Chebyshev spectral method, linear stability analysis (this work, where $Re_{HZ} = Re_{FZ} \times T_{max}$)
0.02	2130	42.60	stationary, $m = 2$	deformed free surface, microgravity, finite difference, linear stability analysis [Kuhlmann and Nienhuser, 2002]
0.02	2108	42.16	stationary, $m = 2$	mixed finite volume - pseudo spectral method [Leypoldt et al., 2000]
	7160	143.20	oscillatory	
0.02	2054	41.08	stationary, $m = 2$	finite-difference, linear stability analysis [Chen et al., 1997]
0.02	2062	41.24	stationary, $m = 2$	mixed Chebychev - finite difference, linear stability analysis [Wanschura et al., 1995]
0.01	1960	19.60	stationary, $m = 2$	3D time-dependent finite element method
	6250	62.50	oscillatory	[Levenstam and Amberg, 1995]

These comparisons with previous studies provide confidence that the hydrodynamic nature of the instability for low Pr liquid bridges is correctly captured here.

3.4 Energy Analysis

Following the linear stability analysis, the energy analysis is another common method used in flow instability studies for liquid bridges. It reveals the energy transfer mechanism from base flow to perturbation at the onset of instability.

The dot product of the velocity perturbation vector (v_{r1},$v_{\theta 1}$,v_{z1}) and the time-dependent momentum equation 3.2 gives time evolution of v_{r1}^2, $v_{\theta 1}^2$ and v_{z1}^2

$$\frac{1}{2}\frac{\partial(v_{r1}^2)}{\partial t} = -v_{r1}^2\frac{\partial v_{r0}}{\partial r} - v_{r1}v_{z1}\frac{\partial v_{r0}}{\partial z} - \frac{1}{2}\left[v_{r0}\frac{\partial(v_{r1}^2)}{\partial r} + v_{z0}\frac{\partial(v_{r1}^2)}{\partial z}\right] - v_{r1}\frac{\partial P_1}{\partial r} + \text{diffusive terms}, \tag{3.54}$$

$$\frac{1}{2}\frac{\partial(v_{z1}^2)}{\partial t} = -v_{r1}v_{z1}\frac{\partial v_{z0}}{\partial r} - v_{z1}^2\frac{\partial v_{z0}}{\partial z} - \frac{1}{2}\left[v_{r0}\frac{\partial(v_{z1}^2)}{\partial r} + v_{z0}\frac{\partial(v_{z1}^2)}{\partial z}\right] - v_{z1}\frac{\partial P_1}{\partial z} + \text{diffusive terms}. \tag{3.55}$$

The energy evolution equation for $v_{\theta 1}^2$ drops out due to $v_{\theta 0} = 0$.

Individual terms on the right hand sides of Equations 3.54 and 3.55 are computed locally to show how and where the kinematic energy is transferred from the base flow into perturbations, so that instabilities grow in time. The $-v_{r1}v_{z1}\partial v_{z0}/\partial r$ term in Equation 3.55 feeds the most energy from the base flow to the perturbation (Figure 3.21a). Physically it means that infinitesimal flow perturbations v_{r1} and v_{z1} grow in time within the strong shear flow $\partial v_{z0}/\partial r$ near the $(r, z) = (1, b)$ corner. The second largest contributing term $-v_{r1}^2\partial v_{r0}/\partial r$ is also due to a strong shear flow $\partial v_{r0}/\partial r$ in roughly the same region (Figure 3.21b). Compared to these two leading terms, other terms in Equations 3.54 and 3.55 (figures not shown) either contribute significantly less or pull energy out from the perturbation. These physics demonstrated

Table 3.4 : Comparison of the first instability with Full-Zone studies in the literature ($Ha = 0$ and unit height-to-radius aspect ratio. The Marangoni number $Ma = Re_{FZ} \times Pr$ is also commonly used in literature) [Huang and Houchens, 2011a]; reprinted with permission.

Pr	Re_{FZ}	Ma	instability mode	features and numerical methods
0.02	1547	30.93	stationary, $m = 2$	spectral method (vorticity transport formulation), linear stability analysis (this work)
0.001	1205	1.21	stationary, $m = 2$	
0.02	1548	30.96	stationary, $m = 2$	finite difference, linear stability analysis with no axial symmetry assumed, regularization parameter $\alpha = 200$ [Kahouadji et al., 2011]
0.02	1645	32.90	stationary, $m = 2$	free surface heat flux $q(z) = (1-z^2)^2$, 3D time-dependent spectral method, linear stability analysis [Bouizi et al., 2007]
0.02	1547	30.93	stationary, $m = 2$	spectral method (stream function - temperature formulation), linear stability analysis [Houchens and Walker, 2005]
0.01	1241	12.41	stationary, $m = 2$	deformed free surface, microgravity, radiative condition solved from a ring heater, time-explicit finite-difference method [Lappa, 2005a]

by the $Pr = 0.02$ and $Ha = 50$ liquid bridge (Figure 3.21) are also valid for other Ha's and low Pr's, with only quantitative differences.

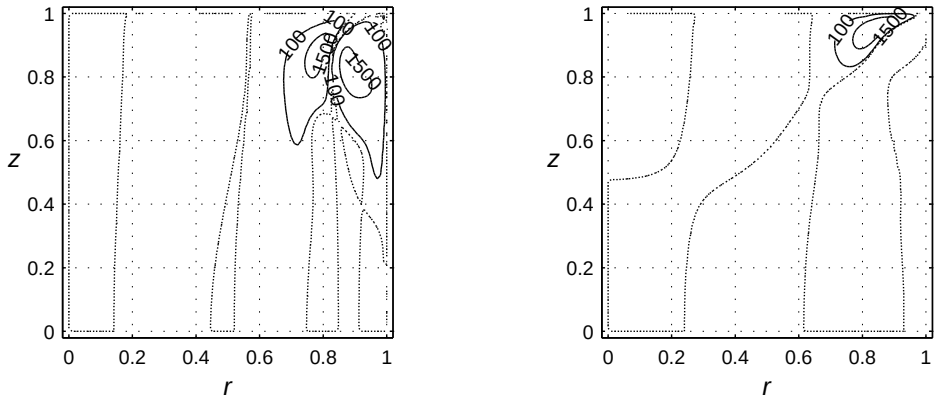

(a) Major contributing term $-v_{r1}v_{z1}\partial v_{z0}/\partial r$ contours

(b) Secondary contributing term $-v_{r1}^2\partial v_{r0}/\partial r$ contours

Figure 3.21 : Energy analysis: $-v_{r1}v_{z1}\partial v_{z0}/\partial r$ feeds the most energy from base flow to perturbations (dotted lines: 0 contours, $Pr = 0.02$, $Ha = 50$ at $Re_{FZ,cr} = 21,879.55$, flow grid $r \times z = 70 \times 100$, temperature grid $r \times z = 40 \times 40$, linear stability grid $r \times z = 40 \times 60$, $\alpha = 1000$) [Huang and Houchens, 2011a]; reprinted with permission.

The *shear flow instability mechanism* shown by the energy analysis confirms the *hydrodynamic* [13] nature of low Pr liquid bridge flow instability, which agrees well with previous studies without magnetic damping [Levenstam and Amberg, 1995, Houchens and Walker, 2005].

[13] As opposed to the *hydrothermal* nature for high Pr liquid bridge flow instability. See Section 3.3 for a discussion.

3.5 Comparison of Normal Mode Linear Stability Analysis and 3D Simulations

The liquid bridge flow instabilities were also simulated using transient three-dimensional (3D) spectral element method [Davis, 2011, Davis et al.,].

First used in 1984 [Patera, 1984], the *spectral element method* is essentially a finite element method that uses high order basis function approximations on elemental grids typical of spectral methods. The finite spectral method combines the flexibility of the finite element method – approximations in complex geometries and basis functions with local support – and the high-order accuracy and spectral convergence of spectral techniques.

The 3D simulation does not assume a flow instability mode, as in the linear stability analysis. A base flow state is allowed to evolve into any flow pattern as long as it satisfies general flow equations and boundary conditions. If Re_{FZ} is ramped up above its critical value for the first instability, the solution is the actual perturbed flow at that Re_{FZ}, obviously. Therefore 3D simulation can verify prediction from the linear stability analysis. Furthermore, 3D simulation also provides information on perturbation magnitudes (that are not available from the linear stability analysis).

On the other hand, the linear stability analysis it provides more insights into flow physics. A wide range of potential instability modes are selected with knowledge of liquid bridge flow instability. The instability mode that most kinematic energy fed into is identified as the critical mode. Also note that instability modes are similar to basis functions in spectral method, such that the actual flow instability could be a combination of multiple instability modes. The example in Subsection 3.5.3 shows that an apparent oscillating instability is, in fact, two competing instability modes.

Furthermore, the critical mode could switch to another instability mode if the test condition (for example, liquid bridge aspect ratio, heat influx distribution and fluid property) varies. Keeping track of these potential instability modes, the linear stability analysis is helpful in explaining experimental observations and even predicting possible flow instabilities under new conditions. Lastly, the linear stability analysis and the energy analysis reveal the instability mechanism for a low Pr liquid bridge to be small perturbations developing within shear flow regions.

3.5.1 First Instability Predicted by Linear Stability Analysis

The linear stability analysis predicts the liquid bridge base flow first transitions to a stationary, $m = 2$, *anti-symmetric mode* at $Re_{FZ,cr} = 1,546.58$ (see Subsection 3.3.3). This critical mode is marked by the rightmost open star symbol labeled A_2^{anti} in the eigenvalue plot Figure 3.22a (at $Re_{FZ} = 1,650$, slightly over $Re_{FZ,cr}$).

The eigenvalue plot Figure 3.22a summarizes leading λ's from the generalized eigenvalue problem (repeating Equation 3.51)

$$\underline{\underline{\mathbf{AM}}}\,\underline{\mathbf{x}} = \lambda\,\underline{\underline{\mathbf{BM}}}\,\underline{\mathbf{x}}$$

in the linear stability analysis, with spurious eigenvalues being discarded (See Appendix A.3). Each eigenvalue represents one instability mode and is labeled as $Letter_m^{symmetry}$. This notation is further explained as follow. The azimuthal wave number m is shown as the subscript. Instability modes with the same m are marked by the same type of symbol. Open symbols denote anti-symmetric instability modes. Solid symbols denote symmetric instability modes.

Disturbances for a given m and given axial symmetry are itemized as A, B and C in descending order of λ_r at a fixed Re_{FZ}. For example, $A_2^{anti} = 2.47$ [14] and

[14] For readability, in the text the numerical values of λ are reported by $Letter_m^{symmetry} = \lambda_r + i\lambda_i$.

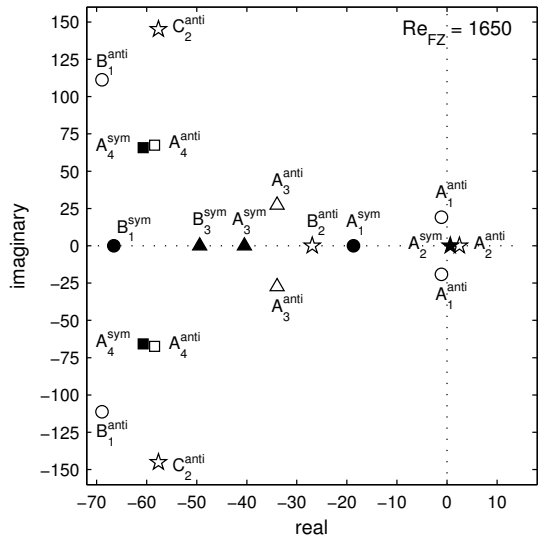

(a) Leading eigenvalues at $Re_{FZ} = 1,650$

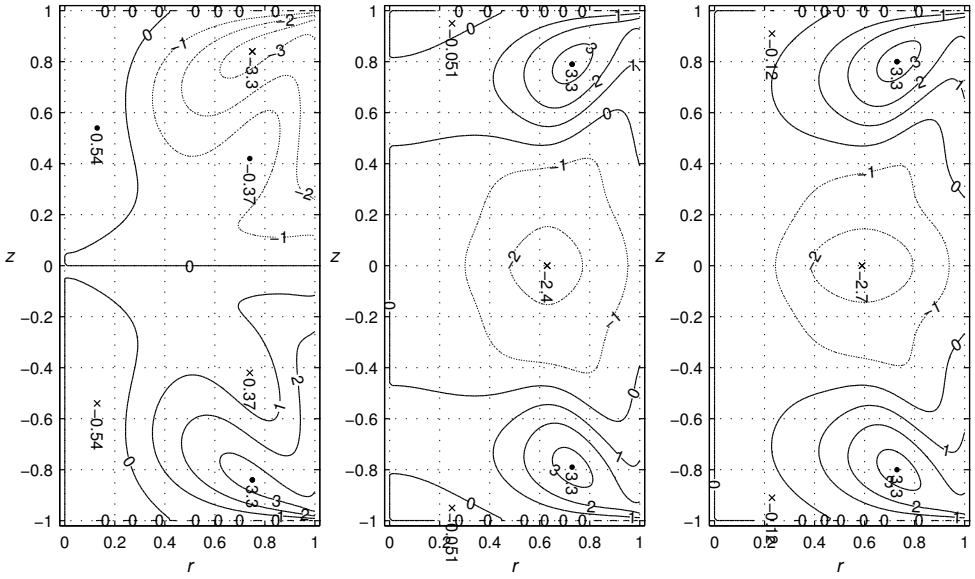

(b) B_2^{anti}, $\lambda_r = -26.9$ (c) A_3^{sym}, $\lambda_r = -40.48$ (d) B_3^{sym}, $\lambda_r = -49.42$

Figure 3.22 : Leading eigenvalues at $Re_{FZ} = 1,650$ and $v_{\theta 1}$ contours of a few real eigenvalue modes from linear stability analysis. Note that A_3^{sym} and B_3^{sym} become a complex pair A_3^{sym} at $Re_{FZ} = 1,750$ in Figure 3.25a. Also notice that the real and imaginary axes are not on the same scale (flow grid $r \times z = 35 \times 45$, temperature grid $r \times z = 30 \times 30$, stability grid $r \times z = 28 \times 28$) [Davis et al.,].

$B_2^{anti} = -26.9$ are different instability modes as shown by their $v_{\theta 1}$ contours (Figures 3.24b and 3.22b, respectively), although they are both $m = 2$ and anti-symmetric.

The linear stability analysis only predicts the onset of instabilities. The disturbance magnitude at nonlinear saturation is not obtained, though perturbation variables that are 5% to 10% of their base flow counterparts is a good estimate [Levenstam and Amberg, 1995]. All disturbance contours from the linear stability analysis in this paper are scaled to best match the corresponding 3D simulations.

[Kahouadji et al., 2011] studied the same problem using linear stability analysis with finite differences and no axial symmetry assumed. Their leading instability modes matched very well with all eigenvalues in Figure 3.22a. Using a very similar numerical scheme to that used in this work, [Bouizi et al., 2007] found that the first instability was a stationary $m = 2$ mode at $Re_{FZ,cr} = 1645$. Their linear stability analysis also predicted a periodic $m = 1$ instability mode at a higher $Re_{FZ} = 1840$. These two leading modes very likely correspond to A_2^{anti} and A_1^{anti} in Figure 3.22a, respectively.

3.5.2 First Instability Predicted by 3D Simulations

[Davis et al.,] simulated Full-Zone instabilities using the spectral element method. The 3D simulations were performed on a Gauss-Legendre-Lobatto collocation grid of 1,600 elements ($r \times \theta \times z = 10 \times 8 \times 20$) with third order velocity interpolations and first order pressure interpolations (in total 45,384 velocity nodes, $r \times \theta \times z = 31 \times 24 \times 61$). For each simulation the time integration begins at a steady, axisymmetric state.

To reproduce the first instability, 3D simulations are run for Re_{FZ} in increments of 50 near the critical value $Re_{FZ,cr} = 1,546.58$ predicted by linear stability analysis. The

---

For example, λ associated with the rightmost eigenvalue in Figure 3.22a is reported as $A_2^{anti} = 2.47+0i$ or simply $A_2^{anti} = 2.47$ rather than $\lambda_{A_{2,r}^{anti}} = 2.47$.

3D simulations bounded the critical value between $Re_{FZ} = 1,600$ and $Re_{FZ} = 1,650$, which is between 3.3% and 6.6% higher than $Re_{FZ,cr}$ predicted from linear stability analysis.

At $Re_{FZ} = 1,650$, the 3D simulations predict a stationary, $m = 2$ anti-symmetric instability, as can be seen in Figure 3.23, the same as predicted by linear stability analysis. Contours of the azimuthal velocity perturbations from the linear stability analysis are compared to the azimuthal velocity extracted from the 3D simulations in a θ plane, where v_θ takes on its maximum magnitude. This comparison is shown in Figure 3.24 and excellent agreement is observed between the eigenmode and the 3D simulation, demonstrating that linear stability analysis accurately predicts all features of the critical instability mode.

3.5.3 Mode Competition above the First Instability

In this subsection, an apparent "periodic instability" above the first instability is observed in 3D simulation. Linear stability analysis reveals that it is actually competition between two stationary instability modes.

Leading Instability Modes at $Re_{FZ} = 1,750$ in Linear Stability Analysis

According to the linear stability analysis, eigenvalues move continuously in the complex plane as the coefficients in the generalized eigenvalue system (Equation 3.51) change. Based on the gradual change in behavior of eigenvalues, the base flow at $Re_{FZ} = 1,750$ ($= Re_{FZ,cr} \times 113\%$, not too large over the critical value) is solved with the axisymmetry assumption to investigate other modes. Leading eigenvalues plots at $Re_{FZ} = 1,750$ (Figure 3.25a) and at $Re_{FZ} = 1,650$ (Figure 3.22a) look very similar, with a few interesting exceptions.

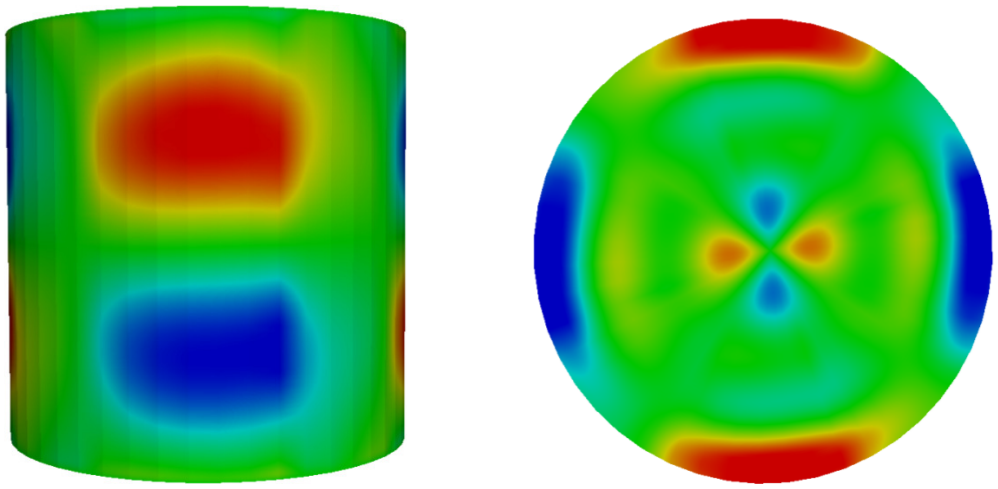

(a) v_θ on the free surface
(red: flow to the right,
blue: flow to the left)

(b) v_θ in the plane $z = 0.5$
(red: flow in counter-closewise direction,
blue: flow in clockwise direction)

Figure 3.23 : The first instability (anti-symmetric, stationary with $m_{cr} = 2$) shown through the azimuthal velocity v_θ plots at $Re_{FZ} = 1,650$ from 3D simulations [Davis et al.,]

The $B_1^{anti} = -68.92 \pm 111.19i$ pair is behind $B_1^{sym} = -66.57$ at $Re_{FZ} = 1,650$, but $B_1^{anti} = -69.33 \pm 118.2i$ surpasses $B_1^{sym} = -71.25$ at $Re_{FZ} = 1,750$. Such relative movements among leading eigenvalues may lead to different instability modes.

Furthermore, two real eigenvalues (stationary instabilities) $A_3^{sym} = -40.48$ and $B_3^{sym} = -49.42$ at $Re_{FZ} = 1,650$ merge into a complex eigenvalue pair (periodic instability) $A_3^{sym} = -44.43 \pm 6.76i$ by $Re_{FZ} = 1,750$. Interestingly, their contours look similar before and after the merger, as indicated in Figures 3.22c, 3.22d, 3.25b and 3.25c. Note that the three-dimensional disturbance corresponding to $A_3^{sym} = -44.43 \pm 6.76i$ at $Re_{FZ} = 1,750$ can be constructed from Figures 3.25b and 3.25c according to Equation 3.53 at $t = 0$.

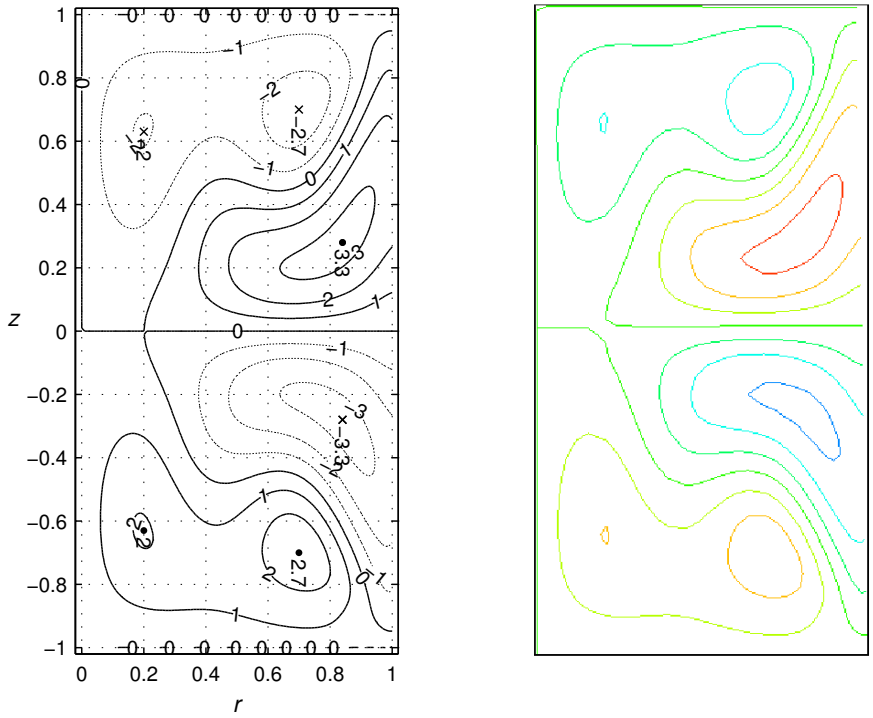

(a) $v_{\theta 1}$ (linear stability analysis) for mode A_2^{anti}, $\lambda_r = 2.47$

(b) v_θ (3D simulation) in the θ plane where its magnitude is maximum

Figure 3.24 : Azimuthal velocity contours at $Re_{FZ} = 1,650$ for the first instability (anti-symmetric, stationary with $m_{cr} = 2$) [Davis et al.,]

"Periodic Instability" at $Re_{FZ} = 1,750$ in 3D Simulations

Whereas the 3D simulation at $Re_{FZ} = 1,650$ found the stationary, anti-symmetric $m = 2$ mode as expected, simulations at $Re_{FZ} \geq 1,700$ exhibit far different behavior.

Initially, the steady and axisymmetric base state at $Re_{FZ} = 1,750$ first transitions into a *symmetric* $m = 2$ mode. This mode grows until the maximum azimuthal velocity reaches $v_\theta = 0.14$ (which occurs slightly interior to the free surface) during the initial transient shown in Figure 3.26.

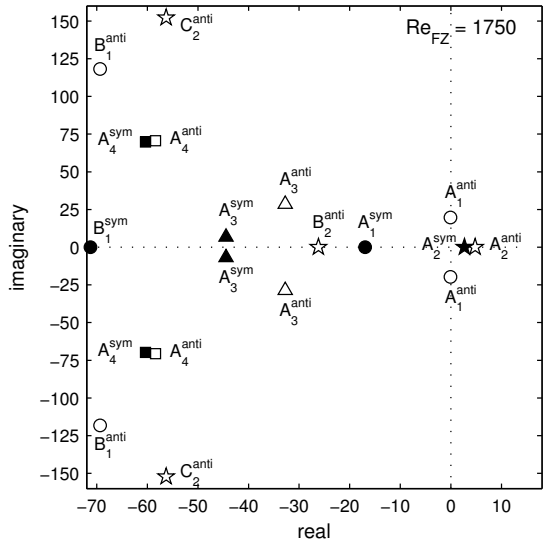

(a) Leading eigenvalues at $Re_{FZ} = 1,750$

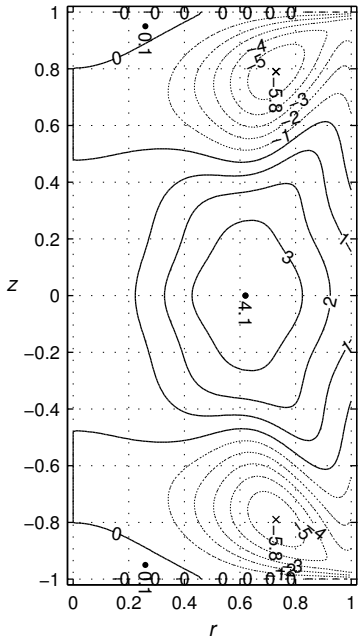

(b) $v_{\theta 1}$ at $\theta = -\pi/6$ for A_3^{sym} with $\lambda = -44.43 \pm 6.76i$ (*i.e.* $v_{\theta 1,i}$ in Equation 3.53)

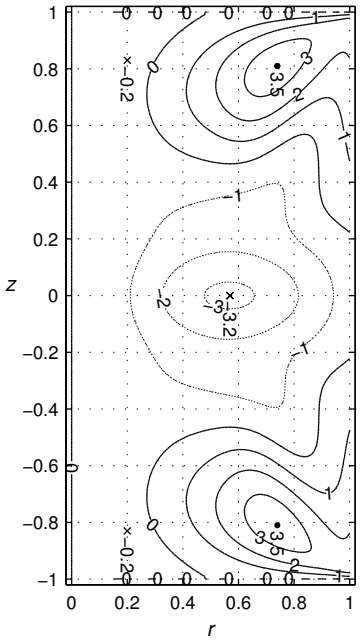

(c) $v_{\theta 1}$ at $\theta = 0$ and $t = 0$ for A_3^{sym} with $\lambda = -44.43 \pm 6.76i$ (*i.e.* $v_{\theta 1,r}$ in Equation 3.53)

Figure 3.25 : Leading eigenvalues at $Re_{FZ} = 1,750$ and $v_{\theta 1}$ contours for a complex pair of eigenvalues with $m = 3$ from linear stability analysis [Davis et al.,]

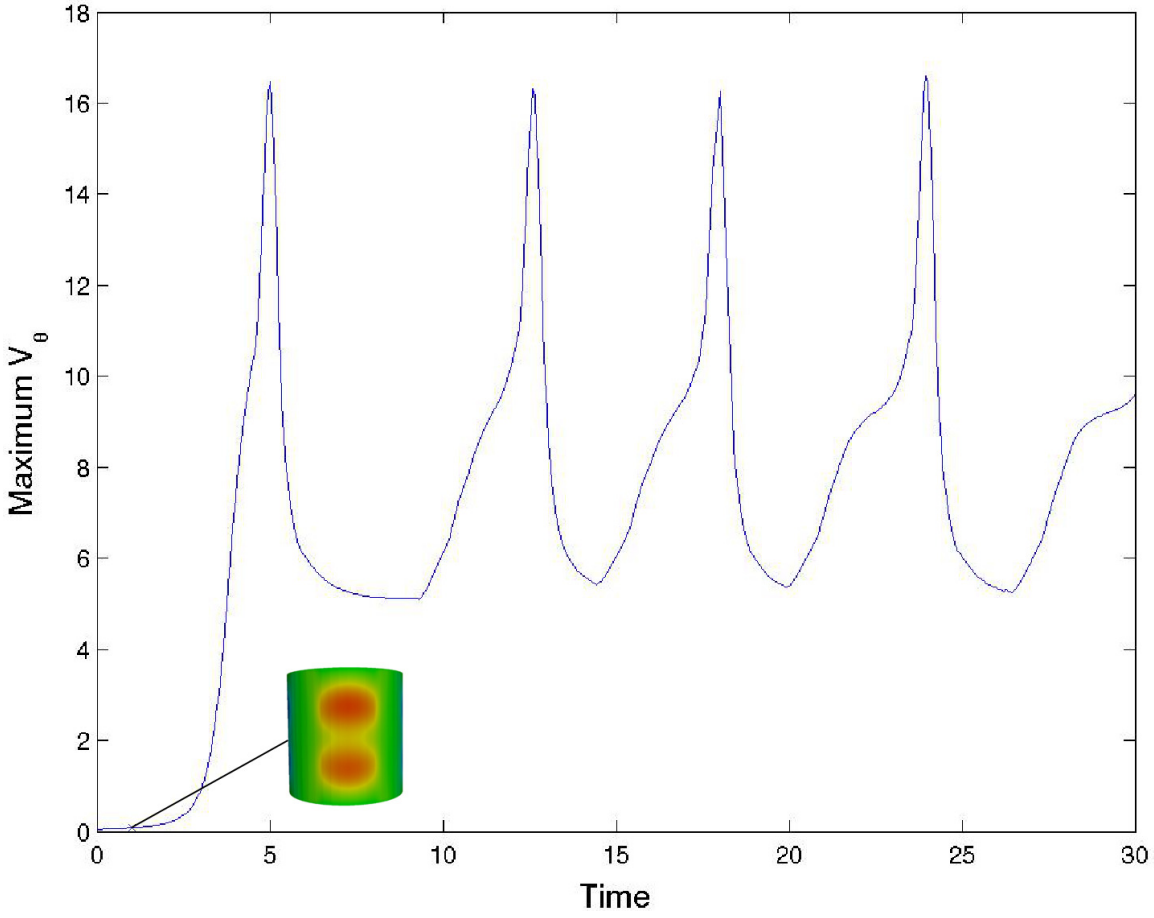

Figure 3.26 : 3D simulation: "periodic instability" at $Re_{FZ} = 1,750$ shown by the maximum azimuthal velocity v_θ time history (blue curve, nondimensional time resolution $\Delta t = 0.05$). Initial transitioning to symmetric $m = 2$ mode shown by v_θ color map on the free surface (red: flow to the right, green: no azimuthal flow). Recall that $v_\theta \equiv 0$ in the base flow state [Davis et al.,].

Then, the flow begins transitioning to an *anti-symmetric* $m = 2$ mode. After that, this $m = 2$ anti-symmetric mode does not reach the steady state. Instead, the anti-symmetric mode competes with the symmetric mode as v_θ on the free surface peaks, and eventually transitions back to a *symmetric* $m = 2$ mode as v_θ approaches a local minimum.

Thereafter, from this symmetric state, the perturbation cells migrate in opposite directions with respect to the axial mid-plane until the *anti-symmetric* mode has once again been reached. From this point, alternating between the *symmetric* and the *anti-symmetric* $m = 2$ instability modes repeats (see Figure 3.27).

"Periodic Instability" at $Re_{FZ} = 1,750$ Interpreted by Linear Stability Analysis

The 3D simulation seems to indicate a periodic $m = 2$ mode above $Re_{FZ,cr}$. However, comparison with linear stability analysis reveals that this "periodic instability" is actually two competing $m = 2$ stationary modes: A_2^{anti} and A_2^{sym}, giving the appearance of periodicity (Figure 3.28).

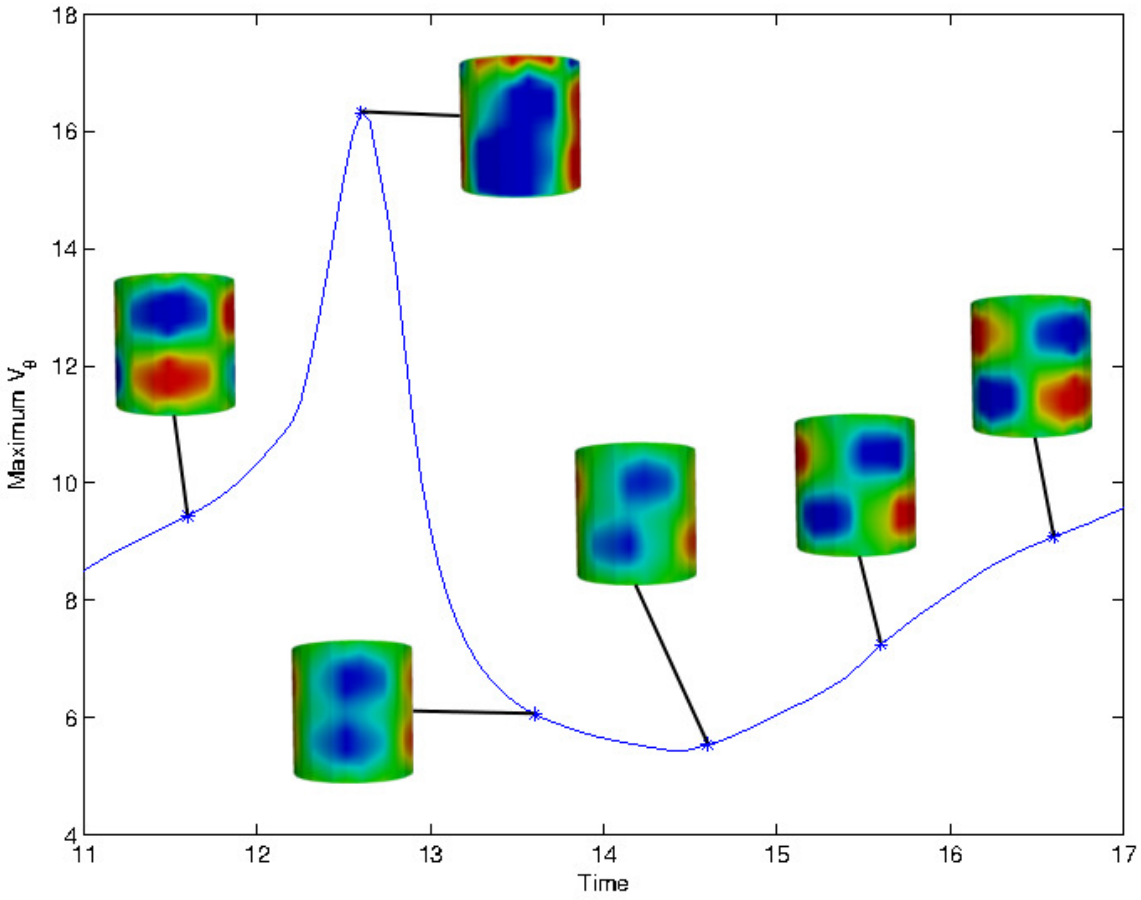

Figure 3.27 : 3D simulation: one period of "periodic instability" at $Re_{FZ} = 1,750$ (blue curve: maximum azimuthal velocity v_θ; color maps: v_θ on the free surface, red: flow to the right, blue: flow to the left). This figure is one cycle of the curve Figure 3.26. Recall that $v_\theta \equiv 0$ in the base flow state [Davis et al.,].

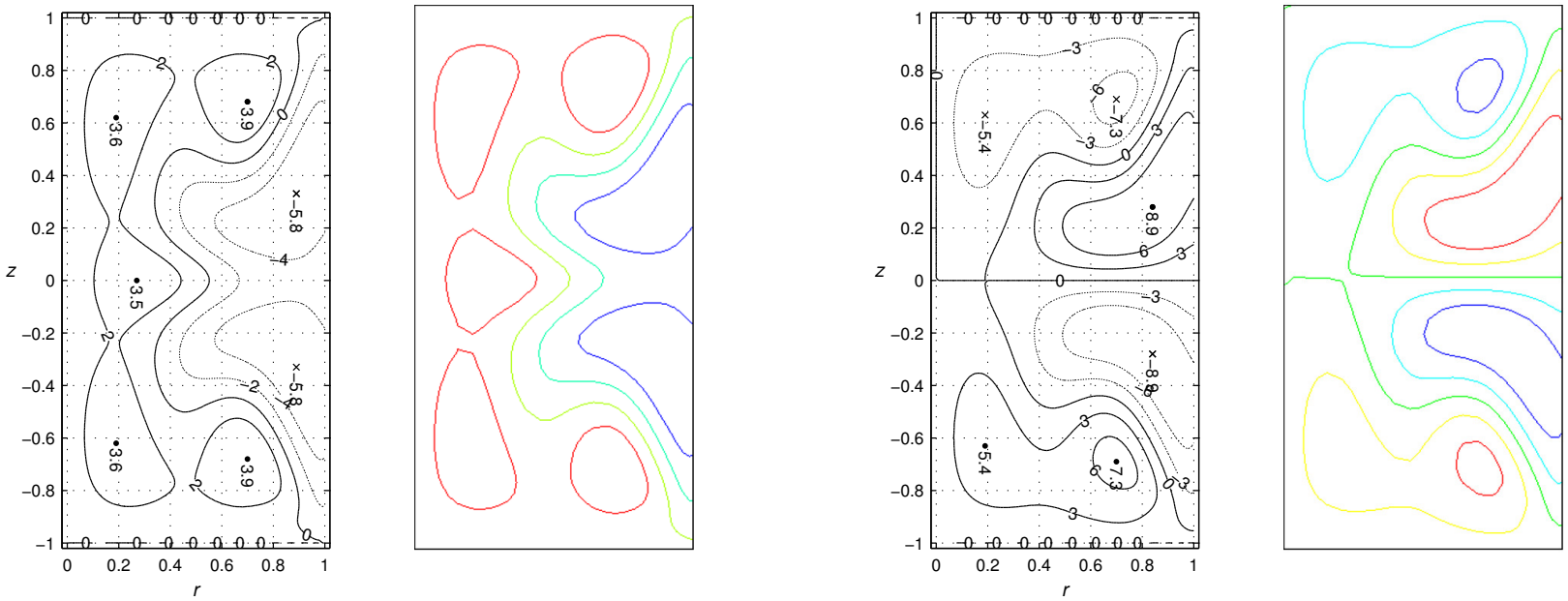

(a) $v_{\theta 1}$ (linear stability analysis) for mode A_2^{sym}, $\lambda_r = 2.7$

(b) v_θ (3D simulation) of symmetric instability

(c) $v_{\theta 1}$ (linear stability analysis) for mode A_2^{anti}, $\lambda_r = 4.8$

(d) v_θ (3D simulation) of anti-symmetric instability

Figure 3.28 : Linear stability analysis (a and c) reveals that the "periodic instability" at $Re_{FZ} = 1,750$ in 3D simulation (b and d) is actually alternating between two stationary instability modes. v_θ contours in 3D simulation are plotted in θ plane, where v_θ is maximum [Davis et al.,].

At $t = 11.6$ in Figure 3.27, the perturbation flow is in the anti-symmetric mode A_2^{anti}. For the anti-symmetric instability, axial flow perturbations v_{z1} are able to cross the mid-plane into the other half of the liquid bridge (black arrows in Figure 3.29a).

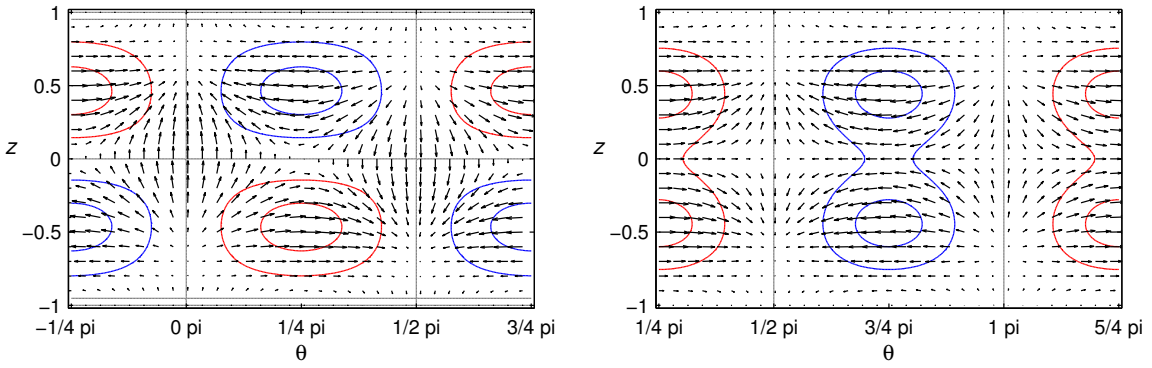

(a) A_2^{anti} (b) A_2^{sym}

Figure 3.29 : Linear stability analysis: flow perturbations on the free surface at $Re_{FZ} = 1,750$. Color contours: $v_{\theta 1}$ (red: flow to the right, blue: flow to the left); black arrows: velocity disturbances $v_{\theta 1} + v_{z1}$ [Davis et al.,].

Recall that mass and momentum exchange across the mid-plane is not allowed in the base flow. This anti-symmetric advection allows flow disturbances in the top and bottom halves of the liquid bridge to spread over the entire height $z \in [-b, b]$ of the liquid bridge (but within a π/m azimuthal wedge). This is shown at $t = 12.6$ in Figure 3.27.

At $t = 13.6$ in Figure 3.27, above transitional state ($t = 12.6$) decays into the symmetric instability A_2^{sym}, due to the symmetric base flow advection associated with v_{z0}.

In the symmetric instability mode, flow does not cross the mid-plane (black arrows in Figure 3.29b). Perturbations in θ gradually develop a shift between the upper and

lower half of the liquid bridge ($t = 14.6$ and 15.6 in Figure 3.27), causing it to cycle back to the anti-symmetric mode at $t = 16.6$.

At the lower $Re_{FZ} = 1,650$, $A_2^{anti} = 2.47$ is the leading eigenvalue (Figure 3.22a), which predicts the transition into a stationary anti-symmetric $m = 2$ instability mode. Although the linear stability analysis also predicts a slightly positive $A_2^{sym} = 0.65$ at $Re_{FZ} = 1,650$, this symmetric mode is not observed in 3D simulations at $Re_{FZ} = 1,650$. The 3D simulation tends to predict transitions at higher Re_{FZ}, partly due to its lower resolution and partly because perturbation growth rates at $Re_{FZ,cr}$ (the value predicted from linear stability analysis) are still very small. At $Re_{FZ} = 1,750$, the $A_2^{sym} = 2.7$ instability mode gains enough energy and has sufficient growth rate to compete with the leading $A_2^{anti} = 4.8$ instability mode. Due to their similar energy states and the ability to convect one mode into the other across the mid-plane, neither mode saturates to a steady state and cyclical competition is observed.

Chapter 4

Flow Stirring by Alternating Magnetic Field

This chapter investigates how an alternating magnetic field enhances convection in confined crystal growth. Induced by magnetic stirring, the forced convection transports fluid particles at a much faster rate in contrast to the slow diffusion rate (see Subsection 2.1.2). The enhanced convection is especially desirable for ternary semiconductor growth, because it reduces the time to achieve uniformity in element composition within the molten material. As a consequence, the growth rate of ternary seminconductors can be accelerated.

The *Bridgman crystal growth technique* and the *traveling heater growth method* are excellent examples where magnetic stirring is often applied. Confined within an ampule, the molten region is approximated by a cylindrical domain. The cylindrical wall represents the inner surface of the ampule. Feed material melts at one end of the cylinder and re-solidifies as a crystal at the other. Both ends are represented by rigid discs in the model.

When the melt is exposed to a weak, external, transverse, slowly rotating magnetic field, such that the external field is always perpendicular to the axis of the ampule, a net electromagnetic body force is induced in the azimuthal direction. This drives a flow in the azimuthal direction. In addition, a secondary meridional circulation also develops.

A stronger, higher frequency transverse magnetic field, or a more complicated alternating magnetic field can induced significant electromagnetic body forces in both

the azimuthal and axial directions. The axial body force is especially desirable to enhance transport of replenishing elements from the melting interface to the growth front in the traveling heater method.

Independent of the complexity of the applied field, the alternating frequency not only affects the electromagnetic body force magnitude, but also impacts the body force distribution through the *magnetic skin depth* (introduced in Subsection 2.2.4).

Note a few key differences exist between the confined crystal growth discussed in this chapter and the liquid bridge models (the main topic of Chapter 3). The liquid bridge has a free cylindrical gas-melt interface where Marangoni convection originates, and flow control for the liquid bridge often aims at suppression of detrimental convection through application of a steady magnetic field. Highest purity is typically the goal for liquid bridge growth. In comparison, the confined crystal growth examined in this chapter has a no-slip, rigid cylindrical wall, which draws the kinetic energy out of the flow through the viscous boundary layer. These processing techniques are being developed for growth of new semiconductor materials, especially ternary alloys where segregation is the major obstacle to overcome. Diffusion and natural convection are often not sufficient to mix the chemical elements, at least not in a controlled way, and therefore forced convection induced by application of an external alternating magnetic field is desired in these growth systems. As in the liquid bridge, gravitational effects are neglected in favor of focusing on the electromagnetic stirring.

4.1 Rotating Magnetic Field

The flow domain is a cylindrical melt of radius R^* and total length $2bR^*$, where b is the aspect ratio (see Figure 4.1). The origin of the cylindrical coordinate system is at the center of the melt. All surfaces surrounding the flow domain are assumed to

be no-slip, no-penetration surfaces. Gravitational and buoyancy effects are neglected and the flow is treated as isothermal to focus the investigation on the impact of the rotating magnetic field.

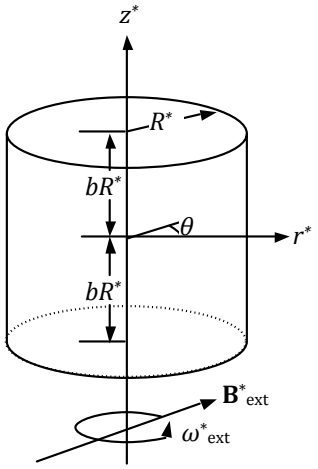

Figure 4.1 : A cylindrical flow domain exposed to an external transverse magnetic field $\mathbf{B}^*_{\text{ext}}$ rotating with frequency $f^* = \omega^*_{\text{ext}}/(2\pi)$. Note that the cylinder is completely immersed in the uniform external magnetic field $\mathbf{B}^*_{\text{ext}}$, although it will be shown (in Figure 4.13) that the magnetic field $\mathbf{B}^*$ within the melt and in nearby space may differ from $\mathbf{B}^*_{\text{ext}}$.

The flow is exposed to an external rotating magnetic field

$$\mathbf{B}^*_{\text{ext}} = B^*_0[\cos(\theta - \omega^*_{\text{ext}} t^*)\hat{\mathbf{e}}_r - \sin(\theta - \omega^*_{\text{ext}} t^*)\hat{\mathbf{e}}_\theta], \tag{4.1}$$

where B^*_0 and ω^*_{ext} are the magnitude and the rotation angular frequency of the external rotating magnetic field, respectively. The azimuthal coordinate is θ, and $\hat{\mathbf{e}}_r$ and $\hat{\mathbf{e}}_\theta$ are the radial and azimuthal unit vectors, respectively. The dimensional time is t^*. The external magnetic field $\mathbf{B}^*_{\text{ext}}$ alternates at AC frequency $f^*_{\text{ext}} = \omega^*_{\text{ext}}/(2\pi)$.

Subsection 2.2.4 demonstrates that the magnetic field $\mathbf{B}^*$ in the melt is not necessarily the same as the external magnetic field $\mathbf{B}^*_{\text{ext}}$. Furthermore, $\mathbf{B}^*$ is decoupled from the flow field for small magnetic Reynolds number Re_m in crystal growth applications. $\mathbf{B}^*$ in the melt is determined by

$$\underbrace{\frac{\mu_p^* \sigma^* R^{*2}}{1/\omega^*_{\text{ext}}}}_{R_\omega} \frac{\partial \mathbf{B}}{\partial t} = \nabla^2 \mathbf{B}, \tag{4.2}$$

where the *shielding parameter* R_ω is defined as

$$R_\omega = \mu_p^* \sigma^* \omega^*_{\text{ext}} R^{*2}. \tag{4.3}$$

In addition, the nondimensional governing equations include incompressible continuity (repeating Equation 2.32)

$$\nabla \cdot \mathbf{v} = 0,$$

and the incompressible Navier-Stokes equations with the electromagnetic body force term (repeating Equation 2.29)

$$\frac{\partial \mathbf{v}}{\partial t} + (\mathbf{v} \cdot \nabla)\mathbf{v} = -\nabla P + \underbrace{\frac{\mu^*}{\rho^* V_0^* R^*}}_{\frac{1}{Re_{\text{classic}}}} \nabla^2 \mathbf{v} + \underbrace{\frac{\sigma^* \omega^*_{\text{ext}} B_0^{*2} R^{*4}}{\rho^* \nu^{*2}}}_{2 \times Ta_m} (\mathbf{v}_{\text{rel}} \times \mathbf{B}) \times \mathbf{B},$$

where P is the pressure, σ^* is the electrical conductivity, and $\nu^* = \mu^*/\rho^*$ is the kinematic viscosity. $V_0^* = \nu^*/R^* = \mu^*/(\rho^* R^*)$ is the characteristic flow velocity. B_0^* and ω^*_{ext} are the magnitude and the angular frequency of the external rotating magnetic field, respectively. R^* is the radius and $\mathbf{v}_{\text{rel}}$ is the relative velocity between the magnetic field rotation and the flow velocity $\mathbf{v}$. The *magnetic Taylor number* (repeating Equation 2.30)

$$Ta_m = \frac{\sigma^* \omega^*_{\text{ext}} B_0^{*2} R^{*4}}{2\rho^* \nu^{*2}}$$

measures the electromagnetic body force of a rotating magnetic field over the viscous force.

4.1.1 Generating a Rotating Magnetic Field in the Opera Solver

Decoupled from the flow field for crystal growth applications, the electromagnetic field is first solved using a finite element electromagnetic solver, *Opera* [Vector Fields Limited, 2007]. Benchmarks against analytical solutions show that Opera predicts magnetic fields generated by solenoids very well (see Appendix B).

The rotating magnetic field is generated by six alternating current (AC) solenoids (red rings in Figure 4.2) evenly spaced around the melt (essentially the working principle of the stator of an AC motor). Adjacent solenoids have 60 degree phase shifts, *i.e.* if one solenoid is at 0 degrees of an AC cycle at a time instance, other solenoids are at 60, 120, 180, 240, 320 degrees, respectively, in counter-clockwise arrangement when looking in $-\hat{\mathbf{e}}_z$ direction, at the same time instance.

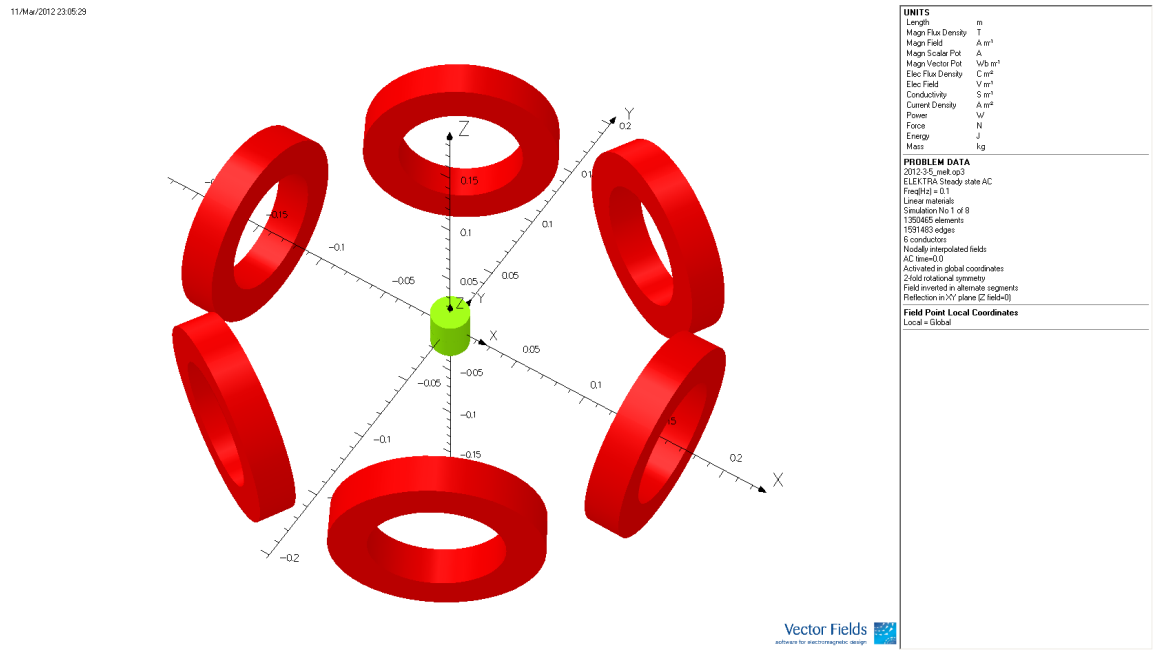

Figure 4.2 : Six AC solenoids (red rings) generate a rotating magnetic field in the center where the melt (green cylinder) is located, as modeled in Opera.

Properties of these six solenoids are not of primary interest so long as the desired rotating magnetic field is produced at the location of the melt. However, the values used are listed here for reference. The inner and outer radius of each solenoid is 0.042 m and 0.066 m, respectively. The cross-sectional area of each solenoid is a 0.024 m by 0.024 m square. The AC electric current is 391.68 A at peak. The equivalent peak electric current density is 680,000 A/m^2. The AC frequency f^*_{ext} is the same in all solenoids, but varies between tests to investigate the magnetic shielding effect in the melt. All six solenoids are at the same distance away from the melt ($\sim$0.13 m) and are relatively far away (more than 10 times the radius of the melt) to produce a relatively-uniform rotating magnetic field.

The melt, located at the center of the six solenoid arrangement, is a cylinder of radius $R^* = 0.01275$ m (diameter 0.0255 m) and total length of $2bR^* = 0.03$ m, where the aspect ratio is $b \approx 1.176$.

First, the melt is replaced with an "air conductor" to examine the rotating magnetic field generated by these six solenoids. In Opera, an "air conductor" is a conductor whose properties are set to air. It acts as air with no electric conductivity or induced magnetic field, but also allows meshing techniques to be applied in the space where it holds.

The unique solution domain for the magnetic field is $r \in [0, \infty)$, $z \in [0, \infty)$ and $\theta \in [0, \pi)$. The finite element computational domain cuts off at about $r^* = 0.1$ m (about $7.8 \times R^*$) and $z^* = 0.1$ m (about $6.7 \times bR^*$). Axial symmetry is assumed with respect to the $z^* = 0$ plane.[1] Rotational symmetry around the axial axis is set between the $\theta = 0$ and $\theta = \pi$ planes.[2] Therefore the computational domain is reduced

[1] by selecting the "Tangential magnetic" option for reflection in the XY coordinate plane in Opera

[2] by selecting "2" symmetry copies of "Negative" rotational symmetry around Z in Opera

to 1/4 of a cylinder shown in Figure 4.3a.[3]

The computational domain is discretized by unstructured finite element meshes. The maximum element size for the melt (the innermost 1/4 cylinder) is 0.0005 m. Surrounding the melt, multiple layers of "air conductors" are specified to ensure sufficient mesh resolution near the melt and manageable total element numbers (about 1.56 million elements and 0.27 million nodes). Maximum element sizes of "air conductors" are 0.001 m, 0.002 m, 0.004 m and 0.008 m, respectively, from the innermost layer contacting the melt to the outermost gray layer.[4]

In addition, these "air conductors" are further divided into smaller volumes by five *cutting sheets* of zero thickness. It is advised to build simple and small volumes in Opera to improve meshing performance and to minimize meshing failures. This test was run on a desktop PC in about 12 minutes using the ELECTRA Steady State solver in Opera. Estimated memory usage was about 1.5 GB.

The rotating magnetic field generated by six solenoids is shown at several time instances during an AC cycle in Figure 4.4. The $\mathbf{B}^*$ field magnitude (colormap) and direction (vectors) is shown in a cutting plane at the center of the domain

---

[3] In Opera, solenoids do not need to be discretized by the finite element mesh and can be located outside of the computational domain. The magnetic field is calculated on each node by integrating over all solenoids using the Biot-Savart law.

[4] Differences between green and gray regions are less significant. The outermost gray region is generated automatically by Opera when creating the computational domain with symmetries. This gray region is always set to air. Only the size and the element size can be specified for this region.

In comparison, the interior green regions are generally conductors, for which electrical and magnetic properties can be set (here these are set to the properties of air). More sophisticated meshing controls such as cutting sheets are available for conductors, and can be used to divide them into smaller volumes preferred by the mesher. All colors are arbitrary and can be changed in Opera.

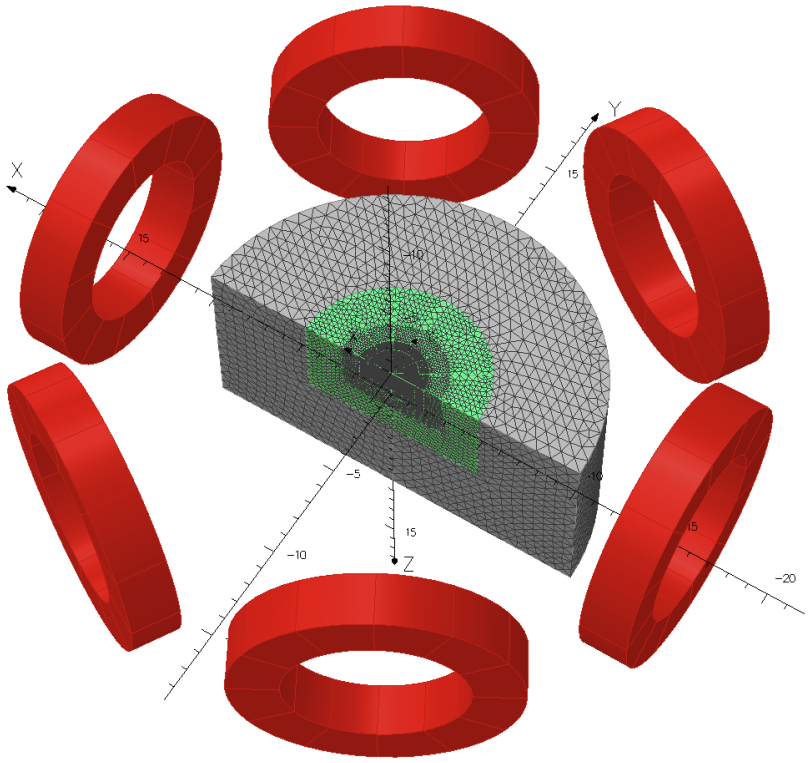

(a) Computational domain is 1/4 of a cylinder (colored in gray and green) due to axial symmetry and rotational symmetry around the axial axis.

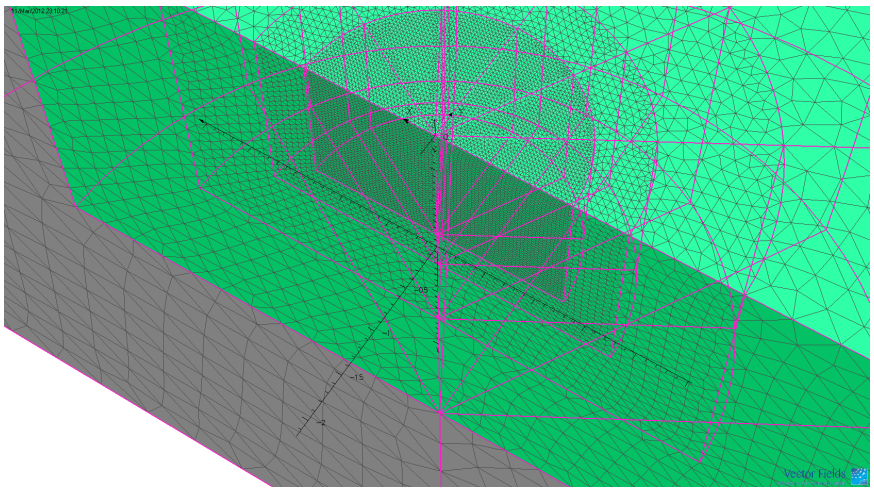

(b) Close-up to the origin showing meshes near the melt.

Figure 4.3 : Computational domain and the finite element mesh for a rotating magnetic field generated by six solenoids. The length unit is centimeters in both figures.

($x^* \in [-R^*, R^*]$ and $y^* \in [-R^*, R^*]$ at $z^* = 0$)[5] where the mid-plane of the melt is located. Note that the "melt" is replaced by an "air conductor" in this example.

Figure 4.4 shows that the generated rotating magnetic flux density is about $\mathbf{B}^* = 5 \times 10^{-4}$ Tesla in magnitude. The $\mathbf{B}^*$ field magnitude is quite uniform over the cutting plane. Within the orange circle (where the melt mid-plane will be located), the magnitude of $\mathbf{B}^*$ varies by at most 1.3% in the cross-section, at any time instance. During the entire AC cycle, the $\mathbf{B}^*$ magnitude varies by at most 7.4% at very limited locations. The field uniformity could be further improved by increasing the number of solenoids (*i.e.* number of *poles* in the stator of the AC motor) surrounding the melt.

4.1.2 Electromagnetic Body Force Induced by a Rotating Magnetic Field at Low Frequency

The innermost cylinder is now set to the approximate properties of a GaInSb melt (no longer an "air conductor") to allow electric current to be induced. The melt density ρ^* and kinematic viscosity ν^* are estimated to be 6.135 kg/m^3 and 1.74×10^{-7} m^2/s, respectively, from values reported in [Houchens et al., 2010]. The electric conductivity is $\sigma^* = 945,000$ S/m (siemens per meter). The permeability is $\mu_p^* = \mu_0 = 4\pi \times 10^{-7}$ N/A^2. The characteristic magnetic flux density is $B_0^* = 5.3 \times 10^{-4}$ Tesla. The melt is a cylinder of radius $R^* = 0.01275$ m (diameter 0.0255 m) and total length of $2bR^* = 0.03$ m, where the aspect ratio is $b \approx 1.176$. These dimensional values are chosen to match GaInSb crystal growth experiments using the traveling heater method.

The external magnetic field $\mathbf{B}^*$ rotates in $+\hat{\mathbf{e}}_\theta$ direction (*i.e.* counter-clockwise rotation if looking into the $-\hat{\mathbf{e}}_z$ direction) at the AC frequency $f_{\text{ext}}^* = 1$ Hz, which corresponds to a maximum azimuthal velocity of 0.08 m/s near the cylindrical surface.

[5] Note that Opera uses the Cartesian coordinate system.

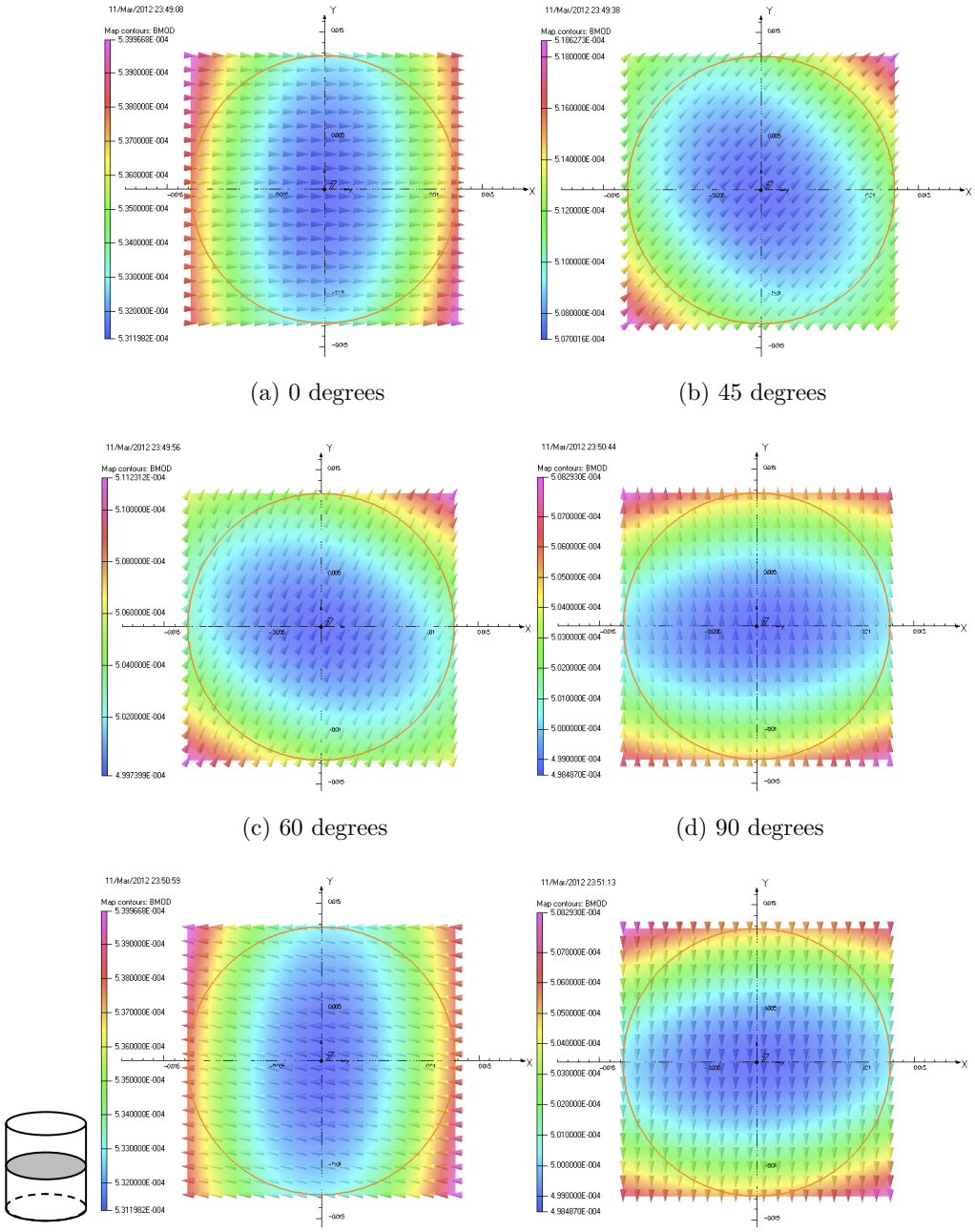

(a) 0 degrees

(b) 45 degrees

(c) 60 degrees

(d) 90 degrees

(e) 180 degrees

(f) 270 degrees

Figure 4.4 : Several time instances during an AC cycle of a rotating magnetic field generated by six solenoids in Opera. Colormap: $\mathbf{B}^*$ magnitude, vectors: $\mathbf{B}^*$ directions, orange circle: the boundary of the melt mid-plane (here set to air).

At the slow rotation frequency $f^*_{\text{ext}} = 1$ Hz in this example, the magnetic shielding effect is negligible. The magnetic shielding parameter $R_\omega = \mu^*_p \sigma^* 2\pi f^*_{\text{ext}} R^{*2} = 1.2\times10^{-3}$ is much smaller than 1. The magnetic skin depth $\delta^*_m = \sqrt{2/(\mu^*_p \sigma^* 2\pi f^*_{\text{ext}})} = 0.52$ m, which is much greater than the melt cylinder radius $R^* = 0.01275$ m. Therefore the external magnetic field diffuses completely into the melt. The $\mathbf{B}^*$ field distribution within the melt (Figure 4.5a) is almost the same as if the melt were not present (Figure 4.4a) due to $\mu^*_p = \mu_0$ and the very slow rotation rate. $\mathbf{B}^*$ is about 5.3×10^{-4} Tesla. At 0 degrees of the AC cycle, the $\mathbf{B}^*$ field points into the $+x$ direction .

Because of the relative motion (primarily in the $-\hat{\mathbf{e}}_\theta$ direction) between the melt fluid and $\mathbf{B}^*$, an electric current is induced within the melt (Figure 4.5b). Predicted by Ohm's law, the electric flux density $\mathbf{j}^*$ circulates towards the $+\hat{\mathbf{e}}_z$ direction in the positive x region in Figure 4.5b, and towards the $-\hat{\mathbf{e}}_z$ direction in the negative x region. The electric current density $\mathbf{j}^*$ is strongest near the cylindrical surface near the x axis (red zone in Figure 4.5b), where the relative motion between $\mathbf{v}^*$ and $\mathbf{B}^*$ is most significant. The $\mathbf{j}^*$ magnitude varies little in the direction perpendicular to $\mathbf{B}^*$ (the y direction in Figure 4.5b). Along the $\mathbf{B}^*$ direction (the x direction in Figure 4.5b), $\mathbf{j}^*$ magnitude quickly drops to a third of the maximum value half way into the cylinder. Please note that vectors only show field directions not magnitude in all figures.

Subsequently, the Lorentz force $\mathbf{F}^*_{\text{EM}} = \mathbf{j}^* \times \mathbf{B}^*$ is dominantly in the $+\hat{\mathbf{e}}_\theta$ direction. Figure 4.5c shows the electromagnetic body force is strongest near the cylindrical surface and near the equator (red zone in Figure 4.5c). Therefore, when exposed to a magnetic field rotating in the $+\hat{\mathbf{e}}_\theta$ direction, the melt is stirred primarily in the same $+\hat{\mathbf{e}}_\theta$ direction (Figure 4.8). Note that the force field $\mathbf{F}^*_{\text{EM}}$ is not axisymmetric and is time-dependent, because $\mathbf{F}^*_{\text{EM}}$ is always perpendicular to $\mathbf{B}^*$, which constantly changes its direction. Figure 4.6 shows the time-averaged body force, which is primarily in

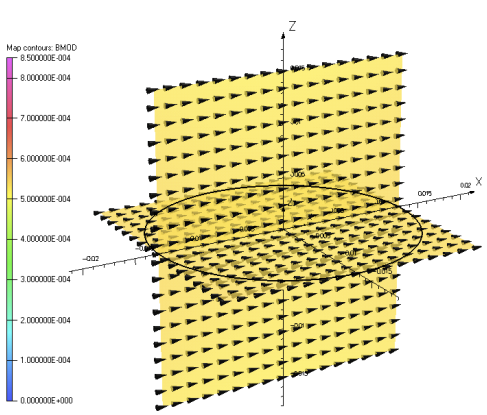

(a) $\mathbf{B}^*$ field (transverse and uniform)

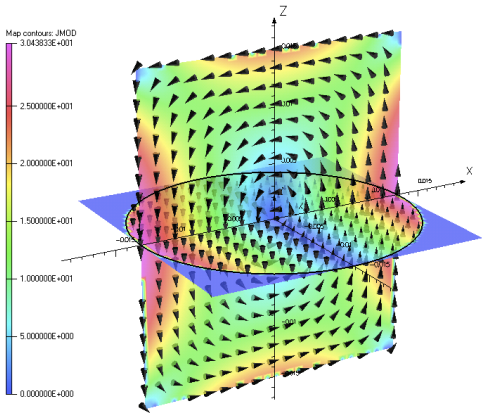

(b) Induced $\mathbf{j}^*$ field (primarily in $\pm\hat{\mathbf{e}}_z$)

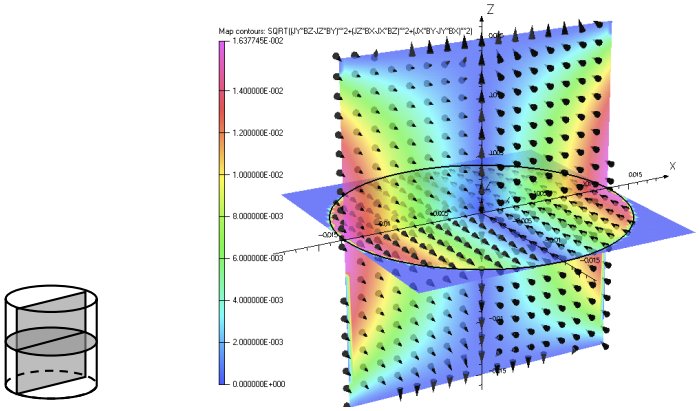

(c) Induced $\mathbf{F}^*_{\mathrm{EM}}$ field (primarily in $+\hat{\mathbf{e}}_\theta$)

Figure 4.5 : Electromagnetic field and body force distribution within the GaInSb melt at one time instance (not time-averaged) at 0 degrees of an AC cycle, with AC frequency $f^*_{\mathrm{ext}} = 1$ Hz. Colormap: magnitudes, vectors: directions.

the azimuthal direction at the low frequency of $f^*_{\text{ext}} = 1$ Hz. The radial and axial components are one order of magnitude weaker than the azimuthal component. Time-averaging has the effect of making the body force seem axisymmetric. At such low frequencies, it is necessary to consider whether the time-averaging is meaningful.

However, magnetic stirring for crystal growth usually is carried out at much higher AC frequencies ($f^*_{\text{ext}} \sim$O(1 kHz)) than in this example. The relative motion between the melt and the external magnetic field is then very high (the field rotates much faster than the flow). The flow can not respond instantaneously to such fast changes in the body force. Therefore, at high AC frequencies, only the time-averaged electromagnetic body force $\langle \mathbf{F}^*_{\text{EM}} \rangle$ matters, and is axisymmetric.

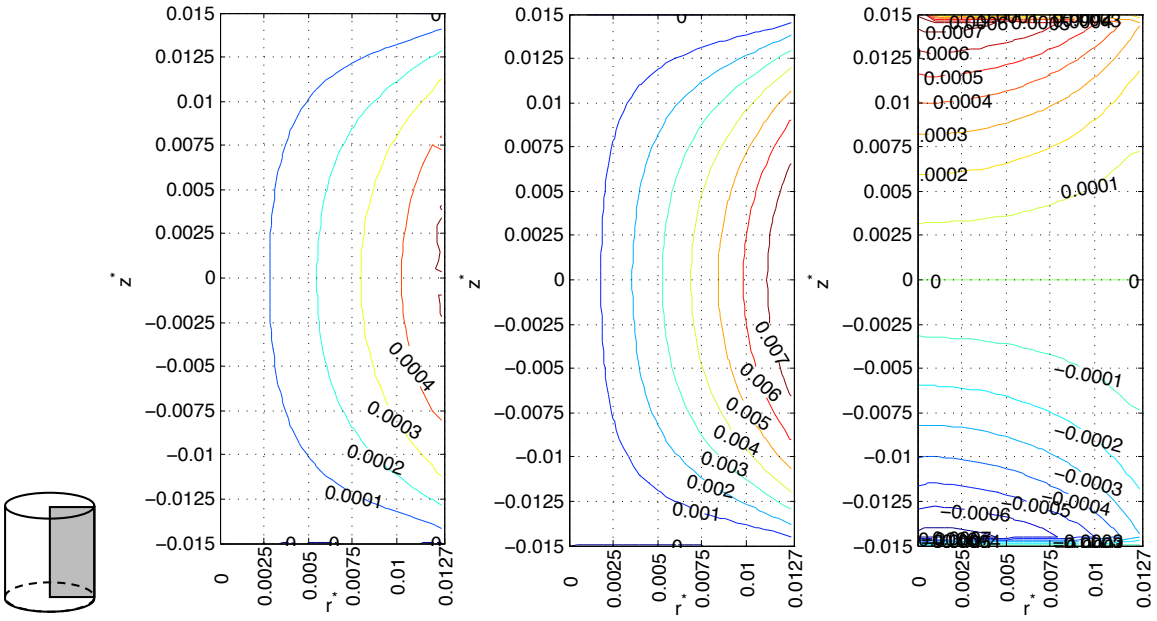

(a) $\langle F^*_{\text{EM},r} \rangle$ (b) $\langle F^*_{\text{EM},\theta} \rangle$ (c) $\langle F^*_{\text{EM},z} \rangle$

Figure 4.6 : Dimensional time-averaged electromagnetic body force $\langle \mathbf{F}^*_{\text{EM}} \rangle$ primarily in the azimuthal direction at the low frequency $f^*_{\text{ext}} = 1$ Hz. $\langle \mathbf{F}^*_{\text{EM}} \rangle$ is axisymmetric.

Low Frequency Approximation

The *low frequency approximation* refers to sufficiently low AC frequencies such that the magnetic shielding effect is weak, and the magnetic skin depth is much thicker than the melt radius. The induced $\mathbf{B}^*$ is negligible (*i.e.* $\mathbf{B}^*$ is practically the same as $\mathbf{B}^*_{\text{ext}}$). Recall from Subsection 2.2.4, the shielding parameter is small, $R_\omega \ll 1$ in the low frequency case.

In addition, for crystal growth applications, the magnetic field alternates much faster than the advection due to the relatively slow flow motion. Therefore, the transport equation for $\mathbf{B}$

$$\underbrace{\overbrace{\mu_p^*\sigma^* R^{*2}\omega_{\text{ext}}^*}^{R_\omega}\frac{\partial \mathbf{B}}{\partial t}}_{\text{variation in time}} + \underbrace{\overbrace{\mu_p^*\sigma^* V_0^* R^*}^{R_m}(\mathbf{v}\cdot\nabla)\mathbf{B}}_{\text{advection}} = \underbrace{\nabla^2\mathbf{B}}_{\text{diffusion}} + \underbrace{\overbrace{\mu_p^*\sigma^* V_0^* R^*}^{R_m}\mathbf{B}\cdot(\nabla\mathbf{v})}_{\substack{\mathbf{B}\text{ field production}\\ \text{by stretching of}\\ \text{magnetic flux lines}}} \tag{4.4}$$

suggests another limit $R_\omega \gg R_m$, which is almost always satisfied in crystal growth applications. As a consequence, although the AC frequency is assumed low, the flow advection is even slower. As a result, the flow still "feels" a time-averaged stirring body force, even in relatively low frequency stirring.[6]

The shielding parameter in the low frequency approximation is bounded by

$$\underbrace{R_m \ll}_{\substack{\text{negligible induced}\\ \text{magnetic field}}} R_\omega \underbrace{\ll 1}_{\substack{\text{low frequency}\\ \text{assumption}}} . \tag{4.5}$$

Substituting the definitions of R_m and R_ω, Equation 4.5 becomes

$$\mu_p^*\sigma^* V_0^* R^* \ll \mu_p^*\sigma^* R^{*2}\omega_{\text{ext}}^* \ll 1. \tag{4.6}$$

[6] If the flow velocity is on the same order as the rotation rate of the magnetic field, then the body force should not be time-averaged, and must be solved in three-dimensions and with time variation considered. However, Equation 4.8 shows that the practical low AC frequency limit is very broad for crystal growth applications, therefore the time-average assumption almost always holds.

Then, induced magnetic fields can be neglected *and* the low frequency approximation is valid if ω^*_{ext} satisfies (after substituting in the choice of characteristic velocity $V_0^* = \nu^*/R^*$ in this work)

$$\frac{\nu^*}{R^{*2}} \ll \omega^*_{\text{ext}} \ll \frac{1}{\mu^*_p \sigma^* R^{*2}}. \tag{4.7}$$

In the current problem, the low frequency approximation is valid in a fairly wide range of ω^*_{ext}, determined by substituting $\nu^* = 1.74 \times 10^{-7}$ m^2/s, $R^* = 0.01275$ m, $\mu^*_p = \mu_0 = 4\pi \times 10^{-7}$ N/A^2 and $\sigma^* = 945,000$ S/m

$$1.07 \times 10^{-3} \text{ rad/s} \ll \omega^*_{\text{ext}} \ll 5,180 \text{ rad/s}. \tag{4.8}$$

Analytical Solution of an Infinitely-Long Conducting Cylinder in the Low Frequency Approximation

For an infinitely-long conducting cylinder stirred by a uniform rotating magnetic field, the time-averaged electromagnetic body force is axisymmetric and has no axial variation. Its analytical solution can be derived as

$$\langle F^*_{\text{EM},\theta} \rangle = \sigma^* B_0^{*2} \omega^*_{\text{ext}} r^*/2, \tag{4.9}$$

which is a linear function of the radial coordinate r^* [Davidson, 2001]. Notice that the stirring body force $\langle F^*_{\text{EM},\theta} \rangle$ is proportional to the magnetic flux density squared, which is similar to the magnetic *damping* body force (also proportional to B_0^{*2}, see Equation 2.23).

More importantly, the stirring body force is also proportional to the AC frequency ω^*_{ext}. Thus, the body force can be strengthened simply by increasing the AC frequency ω^*_{ext}. Therefore, a high AC frequency external magnetic field at weak intensity can be used to save energy while maintaining the same stirring body force. Furthermore, a high AC frequency alternating magnetic field can also be used to stir less conductive

(small σ^*) fluids such as aqueous solutions. Please note though that the analytical solution is valid in the low frequency approximation only, though in practice this only requires $R_\omega \ll 1$ which can often be achieved at moderate ω^*_{ext}. At higher AC frequencies, the stirring body force is absent in the interior due to the magnetic shielding effect.

For laminar flow,[7] the flow velocity only has an azimuthal component and is axisymmetric. The analytical solution can be derived [Davidson, 2001],

$$v^*_\theta = \frac{B^{*2}_0 \sigma^* \omega^*_{\text{ext}}}{16\mu^*} r^* (R^{*2} - r^{*2}). \tag{4.10}$$

Notice that the flow velocity is proportional to the magnetic flux density squared, and is also proportional to the AC frequency.

Electromagnetic Body Force in a Conducting Cylinder of Finite Length in the Low Frequency Approximation

For a conducting cylinder of *finite* length, a more realistic model for confined crystal growth, the analytical solution of the time-averaged electromagnetic body force is available in the low frequency approximation. The body force is axisymmetric and assumed to have only an azimuthal component [Mazuruk et al., 1997, Witkowski et al., 1999]

$$\langle F_{\text{EM},\theta} \rangle = r - 2 \sum_{N=1}^{\infty} \frac{J_1(\lambda_N r) \cosh(\lambda_N z)}{(\lambda_N^2 - 1) J_1(\lambda_N) \cosh(b\lambda_N)}, \tag{4.11}$$

where J_k is the Bessel function of the first kind and k^{th} order, r and z are the nondimensional radial and axial coordinates, respectively, b is the aspect ratio of the

[7] Similar swirling flows are also observed in metallurgical processes. These flow are always turbulent in practice, and analytical solutions are not necessarily available. However, the flow solution in an infinitely-long conducting cylinder has been derived with a proper turbulence model [Davidson, 2001].

melt cylinder, and λ_N are roots of

$$\lambda_N J_0(\lambda_N) - J_1(\lambda_N) = 0. \tag{4.12}$$

Time-averaged $\langle F_{\mathrm{EM},\theta} \rangle$ for $f^*_{\mathrm{ext}} = 0.1$ Hz and $f^*_{\mathrm{ext}} = 100$ Hz from Opera simulations are compared with the analytical prediction in Figure 4.7. Simulated body force values are first computed as $\mathbf{F}^*_{\mathrm{EM}} = \mathbf{j}^* \times \mathbf{B}^*$ in Opera, time-averaged within an AC cycle, then nondimensionalized as $\langle \mathbf{F}_{\mathrm{EM}} \rangle = \langle \mathbf{F}^*_{\mathrm{EM}} \rangle / (\sigma^* \omega^*_{\mathrm{ext}} R^* B_0^{*2}/2)$. The stirring body force is strongest near the cylindrical surface and near the half length of the melt cylinder. In Figure 4.7, the agreement between the analytical solution and simulation results for $f^*_{\mathrm{ext}} = 0.1$ Hz and $f^*_{\mathrm{ext}} = 100$ Hz demonstrates that the low frequency approximation is valid in a fairly wide range of AC frequencies (recall Equation 4.8). Even at $f^*_{\mathrm{ext}} = 100$ Hz, the radial and axial body force components (not shown) are at least a couple of orders of magnitude weaker than the dominant azimuthal component. Nevertheless, the dimensional body force is much stronger at $f^*_{\mathrm{ext}} = 100$ Hz than at $f^*_{\mathrm{ext}} = 0.1$ Hz due to the redimensionalization $\langle F^*_{\mathrm{EM},\theta} \rangle = (\sigma^* \omega^*_{\mathrm{ext}} R^* B_0^{*2}/2) \times \langle F_{\mathrm{EM},\theta} \rangle$.

4.1.3 Flow Stirred by a Rotating Magnetic Field at Low Frequency

Subsection 2.2.3 demonstrated the decoupling of the electromagnetic field from the flow field at small magnetic Reynolds number R_m in most crystal growth applications. Therefore, the electromagnetic body force is completely determined in Opera, and then time-averaged yielding $\langle \mathbf{F}^*_{\mathrm{EM}} \rangle = \langle \mathbf{j}^* \times \mathbf{B}^* \rangle$. Then the flow solver reads in this body force as an input into the Navier-Stokes equations (Equation 2.31). The flow field is solved using a steady three-dimensional spectral element method [Davis, 2011].

At low AC frequencies, the body force, which is dominantly in the azimuthal direction, drives a *primary flow* also in the azimuthal direction. An example at

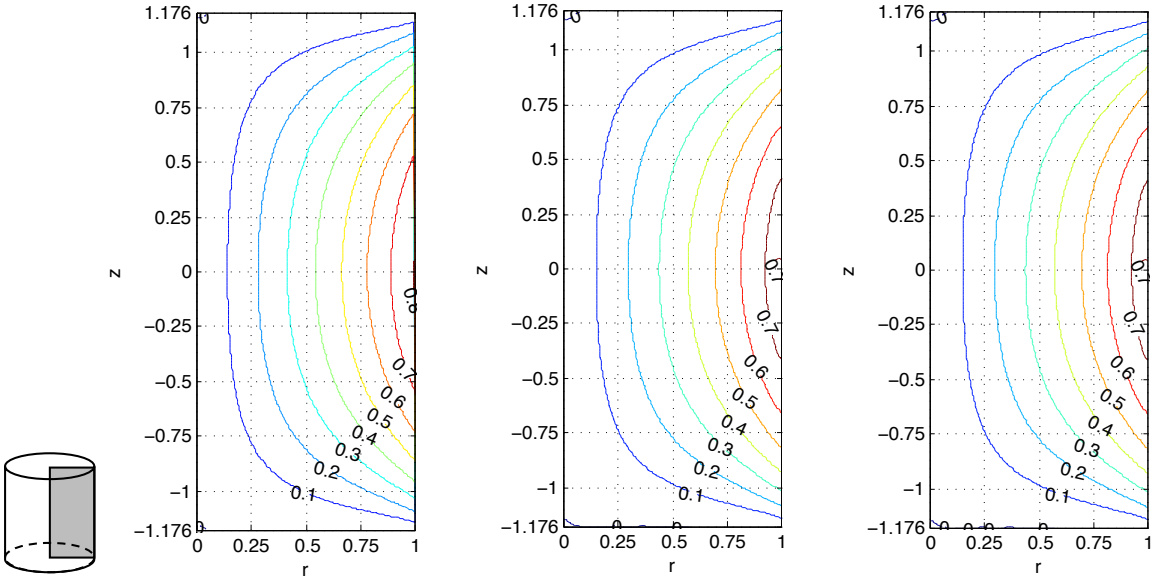

(a) $\langle F_{\mathrm{EM},\theta} \rangle$ analytical solution from Equation 4.11

(b) $\langle F_{\mathrm{EM},\theta} \rangle$ Opera simulation at $f^*_{\mathrm{ext}} = 0.1$ Hz

(c) $\langle F_{\mathrm{EM},\theta} \rangle$ Opera simulation at $f^*_{\mathrm{ext}} = 100$ Hz

Figure 4.7 : Validation of the azimuthal component of the nondimensional, time-averaged electromagnetic body force at "low" AC frequencies.

$f^*_{\mathrm{ext}} = 1$ Hz is shown in Figure 4.8, whose velocity components are shown in Figure 4.9. The stirring body force is strongest near the cylindrical surface and the mid-plane (Figure 4.6). But due to the viscous boundary layer near the cylindrical surface, the fastest flow does not occur at the maximum-body-force region. Instead, the primary azimuthal flow is most significant at a distance away from the cylindrical surface and near the mid-plane (Figure 4.11b). The flow centrifugal acceleration is balanced by a radial pressure gradient. Due to continuity, flow particles gradually circulate out of their orbiting z plane, and gain axial velocity away from the mid-plane, then return through the cylinder interior back to the mid-plane. The meridional flow motion superimposed onto the primary flow is often called the *secondary flow*. The flow in

a conducting cylinder is steady, axisymmetric, and symmetric with respect to the mid-plane, when stirred at low frequencies (slower than $f^*_{\text{ext}} = 1,068$ Hz for the current GaInSb melt cylinder, according to a linear stability study [Grants and Gerbeth, 2002]).

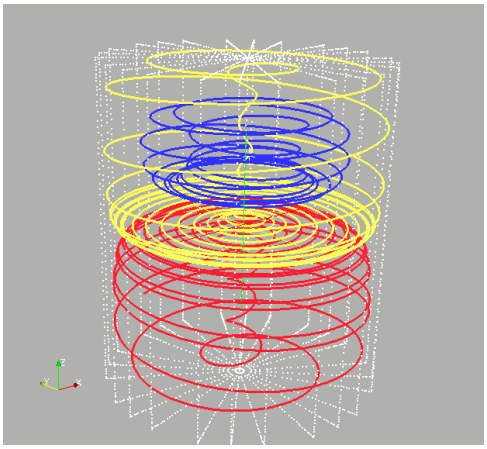

Figure 4.8 : Axisymmetric flow $\mathbf{v}^*$ (primarily in $+\hat{\mathbf{e}}_\theta$) within the GaInSb melt stirred by the rotating magnetic field at a low frequency, $f^*_{\text{ext}} = 1$ Hz. The three path lines are colored differently to distinguish them. Color does not indicate flow velocity. The resolution of the finite element grid is $r \times \theta \times z = 10 \times 8 \times 20$. Gauss-Legendre-Lobatto spectral elements are 3^{rd} order for velocity and 1^{st} order for pressure.

4.1.4 Effects of AC Frequency

The stirring body force is stronger at higher AC frequency. The magnetic Taylor number Ta_m measures the electromagnetic body force of a rotating magnetic field over the viscous force. By definition (Equation 2.30), Ta_m is proportional to the AC frequency f^*_{ext}. Ta_m values are listed in Table 4.1 for various AC frequencies. Because Ta_m is the scaling of the electromagnetic body force in the Navier-Stokes

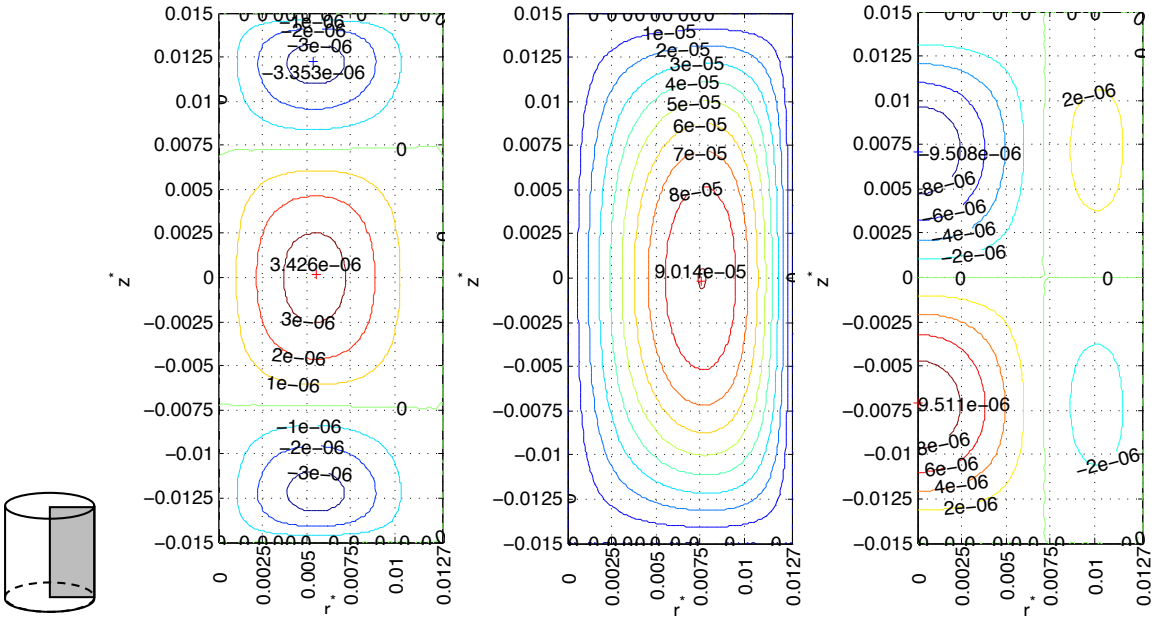

(a) v_r^* (b) v_θ^* (c) v_z^*

Figure 4.9 : Dimensional flow velocity $\mathbf{v}^*$ is most significant in θ stirred by the low frequency ($f_{\text{ext}}^* = 1$ Hz) rotating magnetic field. $\mathbf{v}^*$ is axisymmetric.

equations 2.31, and the nondimensional $\langle F_{\mathrm{EM},\theta} \rangle$ is almost invariant at least up to $f^*_{\mathrm{ext}} = 100$ Hz (recall Figure 4.7), Figure 4.10 shows that the dimensional azimuthal body force $\langle F^*_{\mathrm{EM},\theta} \rangle$ increases linearly from $f^*_{\mathrm{ext}} = 0.1$ Hz to 100 Hz.

Table 4.1 : AC-frequency related quantities of the GaInSb cylindrical melt (calculations based on melt properties in Subsection 4.1.2) and melt radius $R^* = 0.01275$ m

AC frequency	angular frequency	magnetic Taylor number	shielding parameter	skin depth
f^*_{ext}	$\omega^*_{\mathrm{ext}} = 2\pi f^*_{\mathrm{ext}}$	Ta_m	R_ω	δ^*_m
0.1 Hz	0.63 rad/s	11.86	0.00012	1.64 m
1 Hz	6.28 rad/s	118.6	0.0012	0.52 m
10 Hz	62.8 rad/s	1,186	0.0121	0.16 m
100 Hz	628 rad/s	11,865	0.12	0.052 m
1 kHz	6,283 rad/s	1.19×10^5	1.21	0.0164 m
5 kHz	31,416 rad/s	5.93×10^5	6.06	0.0073 m
50 kHz	3.14×10^5 rad/s	5.93×10^6	60.65	0.0023 m

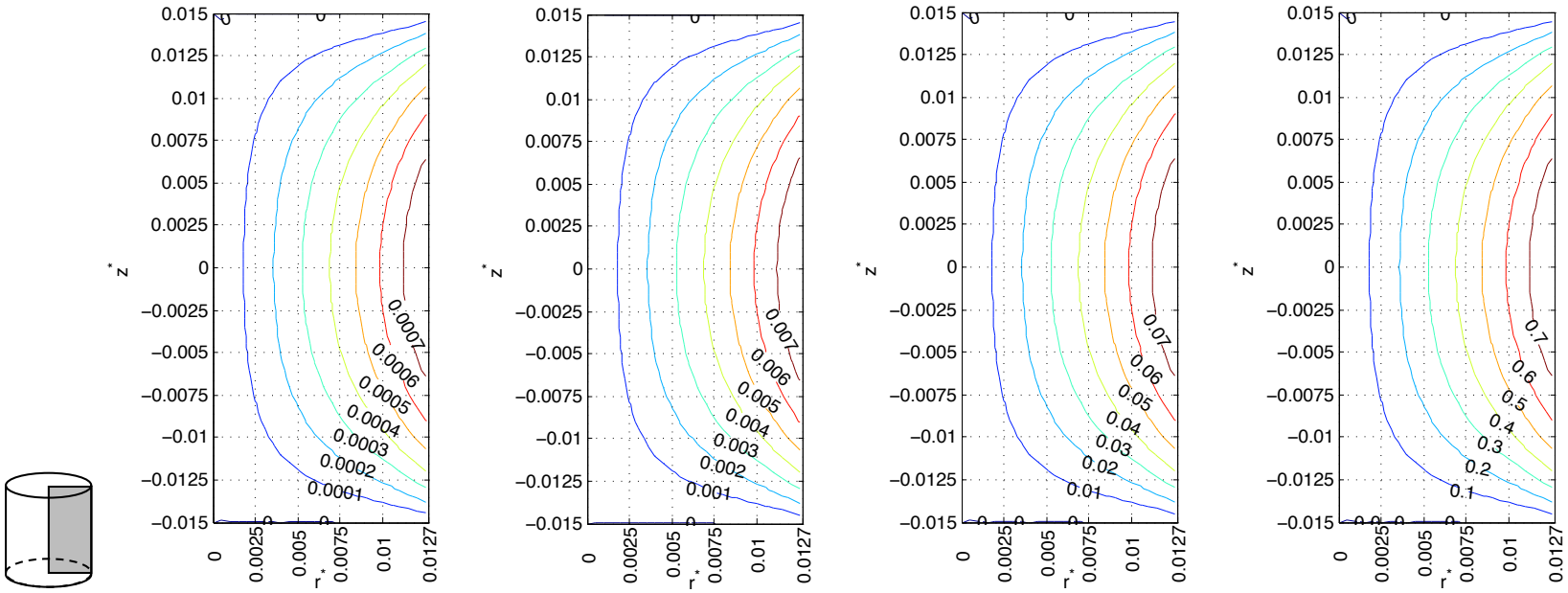

(a) $\langle F^*_{\mathrm{EM},\theta} \rangle$ at $f^*_{\mathrm{ext}} = 0.1$ Hz (b) $\langle F^*_{\mathrm{EM},\theta} \rangle$ at $f^*_{\mathrm{ext}} = 1$ Hz (c) $\langle F^*_{\mathrm{EM},\theta} \rangle$ at $f^*_{\mathrm{ext}} = 10$ Hz (d) $\langle F^*_{\mathrm{EM},\theta} \rangle$ at $f^*_{\mathrm{ext}} = 100$ Hz

Figure 4.10 : The dimensional azimuthal body force $\langle F^*_{\mathrm{EM},\theta} \rangle$ strengthens linearly with the AC frequency f^*_{ext}. $\langle F^*_{\mathrm{EM},\theta} \rangle$ is axisymmetric. Notice that color contours are scaled differently in the subfigures.

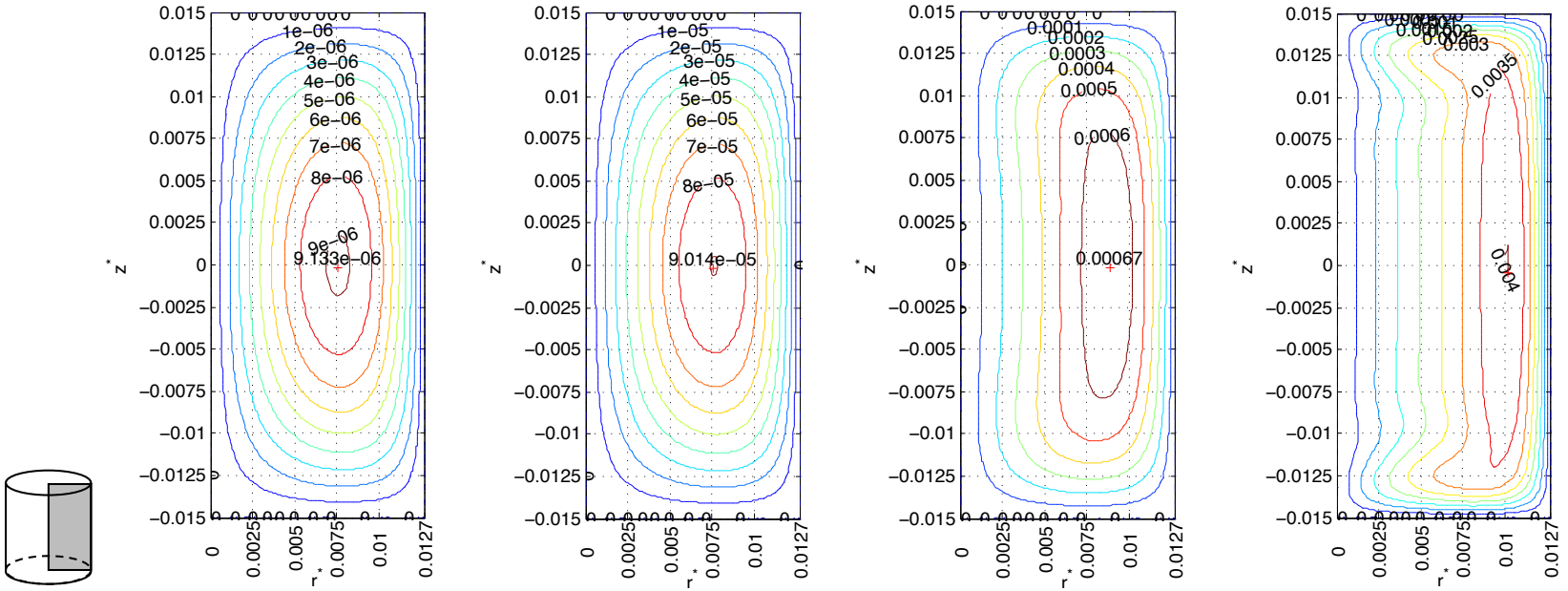

(a) v_θ^* at $f_{\text{ext}}^* = 0.1$ Hz (b) v_θ^* at $f_{\text{ext}}^* = 1$ Hz (c) v_θ^* at $f_{\text{ext}}^* = 10$ Hz (d) v_θ^* at $f_{\text{ext}}^* = 100$ Hz

Figure 4.11 : The dimensional azimuthal flow velocity v_θ^* strengthens sub-linearly with the AC frequency f_{ext}^*. v_θ^* is axisymmetric. Notice that the color contours are scaled differently in the subfigures.

At a result, the azimuthal primary flow is greatly enhanced at higher AC frequencies. Figure 4.11 shows the maximum v_θ^* values increase sub-linearly with f_{ext}^*. Also notice that the strongest flow region is closer to the boundries at higher AC frequencies, because the viscous boundary layer is thinned due to the enhanced azimuthal flow when magnetic stirring intensifies. A similar trend is observed for the meridional secondary flow (*i.e.* v_r^* and v_z^*). Figure 4.12 shows that the center of the meridional flow circulation moves closer to the cylindrical surface and two ends at higher AC frequencies. The meridional flow stream function ψ_θ^* is defined as

$$v_r^* = \frac{1}{r^*}\frac{\partial \psi_\theta^*}{\partial z^*} \qquad \text{and} \qquad v_z^* = -\frac{1}{r^*}\frac{\partial \psi_\theta^*}{\partial r^*}, \tag{4.13}$$

where v_r^* and v_z^* are radial and axial flow velocity, respectively.

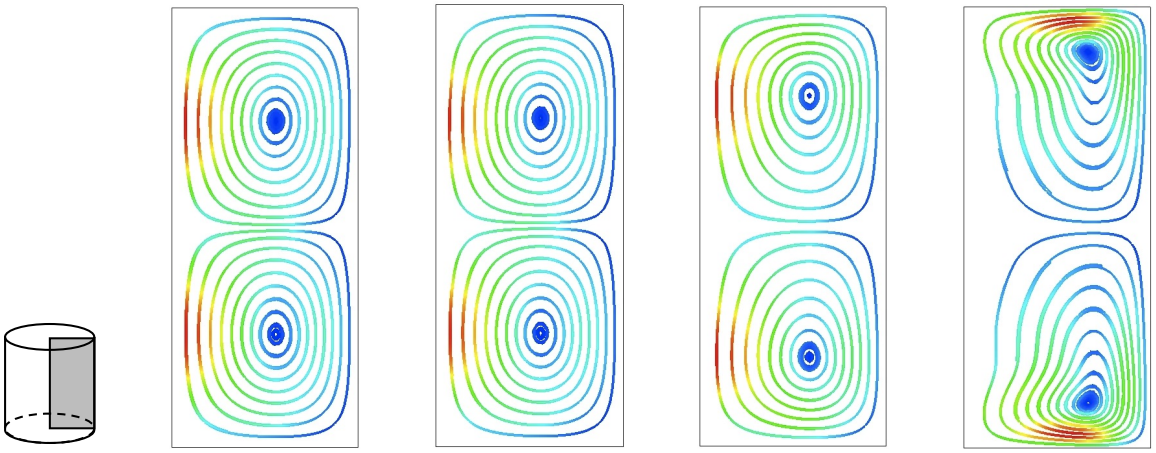

(a) $f_{\text{ext}}^* = 0.1$ Hz (b) $f_{\text{ext}}^* = 1$ Hz (c) $f_{\text{ext}}^* = 10$ Hz (d) $f_{\text{ext}}^* = 100$ Hz

Figure 4.12 : Meridional flow stream function ψ_θ^* contours show that the secondary flow is compressed to the boundaries at higher AC frequencies. (Color contours are scaled differently in the subfigures.)

Furthermore, Table 4.1 also shows that skin depths up to $f_{\text{ext}}^* = 1$ kHz are larger

than the melt radius $R^* = 0.01275$ m. At these "low" AC frequencies, the external magnetic field has sufficient time to diffuse into the conducting cylinder. $\mathbf{B}^*$ is practically the same as $\mathbf{B}^*_{\text{ext}}$. The same physics is also indicated by the small magnetic shielding parameter R_ω at these AC frequency values, as shown in Table 4.1. R_ω measures the magnetic diffusion time over the alternating period of the external magnetic field.

4.1.5 Magnetic Shielding Effect at High AC Frequency

The magnetic shielding effect refers to the fact that the external alternating magnetic field only diffuses into a skin depth into the electrical-conducting media at high AC frequencies – when the diffusion time of the magnetic field is less than or comparable to the short AC period.

Table 4.1 shows that, at high AC frequencies such as $f^*_{\text{ext}} = 5$ kHz and 50 kHz, the skin depth is smaller than the melt radius. $\mathbf{B}^*$ is much weaker than or even virtually absent from $\mathbf{B}^*_{\text{ext}}$ under the skin depth. The strong magnetic shielding effect is also indicated by the larger values of the shielding parameter R_ω, which measures the diffusion time over the AC period.

Figure 4.13 compares the effect of low to high AC frequencies on the $\mathbf{B}^*$ field within and surrounding the melt. At a "low" AC frequency, such as $f^*_{\text{ext}} = 100$ Hz, the external magnetic field $\mathbf{B}^*_{\text{ext}}$ diffuses thoroughly into the melt. The magnetic field $\mathbf{B}^*$ within the melt is practically the same as $\mathbf{B}^*_{\text{ext}}$, as shown by Figures 4.13a and 4.13b. The magnetic flux lines extend uniformly through the conducting material, as if it were air.

An AC frequency of $f^*_{\text{ext}} = 5$ kHz is near the upper limit (or slightly above) of the practical range in crystal growth applications. Figure 4.13c shows that the magnetic

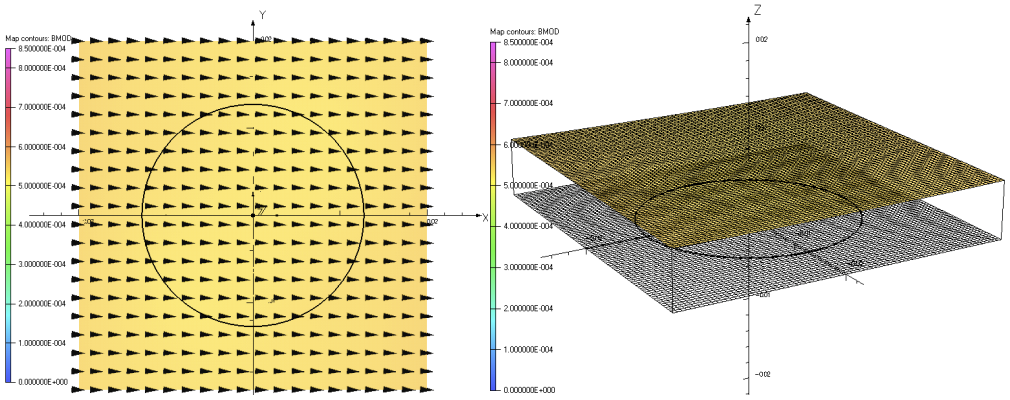

(a) Uniform magnetic flux $\mathbf{B}^*$ at $f^*_{\text{ext}} = 100$ Hz (b) Uniform $\mathbf{B}^*$ magnitude at $f^*_{\text{ext}} = 100$ Hz

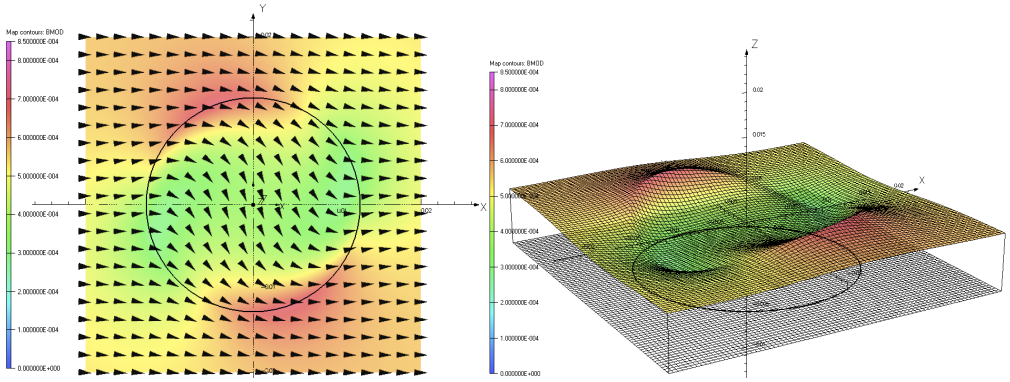

(c) Twisted magnetic flux $\mathbf{B}^*$ at $f^*_{\text{ext}} = 5$ kHz (d) Disturbed $\mathbf{B}^*$ magnitude at $f^*_{\text{ext}} = 5$ kHz

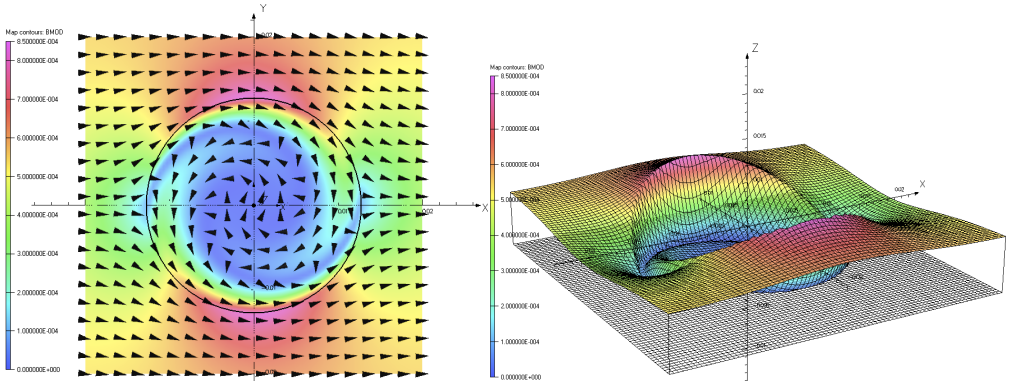

(e) Magnetic shielding effect at $f^*_{\text{ext}} = 50$ kHz(f) Almost zero $\mathbf{B}^*$ at the interior at $f^*_{\text{ext}} = 50$ kHz

Figure 4.13 : $\mathbf{B}^*$ within and surrounding the melt when exposed to an external rotating magnetic field with "low" to high AC frequencies, at 0 degrees of the AC cycle when $\mathbf{B}^*_{\text{ext}}$ points to the $+\hat{\mathbf{e}}_x$ direction. The black circle marks the mid-plane of the melt.

flux lines are twisted significantly within the melt. The $\mathbf{B}^*$ magnitude is also disturbed (Figure 4.13d), which indicates that magnetic flux lines (not shown) are not uniformly spaced. $\mathbf{B}^*$ is weaker than $\mathbf{B}^*_{\text{ext}}$ in the core of the melt (green area near the center in Figure 4.13d). The $\mathbf{B}^*$ magnitude fluctuates above or below the $\mathbf{B}^*_{\text{ext}}$ magnitude near the melt boundary.

The magnetic shielding effect is most prominent at the highest AC frequency $f^*_{\text{ext}} = 50$ kHz in Figure 4.13. During the very short AC period (2×10^{-5} s), the external magnetic field hardly diffuses into the melt, such that $\mathbf{B}^*$ is almost zero in the core region (blue area in Figure 4.13f). As a result, electric current $\mathbf{j}^*$ is only induced within a narrow depth of the melt boundary (red areas in Figure 4.14a). Furthermore, the magnetic flux lines are twisted drastically within the melt (Figure 4.13e) due to the fast rotation. Please note that vectors only show $\mathbf{B}^*$ directions, with no information about magnitude.

Subsequently, the electromagnetic body force $\mathbf{F}^*_{\text{EM}}$ is only present within a shallow skin depth into the melt (red areas in Figure 4.15) at $f^*_{\text{ext}} = 50$ kHz. Please note that Figure 4.14 shows $\mathbf{j}^*$ and $\mathbf{F}^*_{\text{EM}}$ fields at a time instance. The flow only "feels" the time-averaged body force, which is axisymmetirc. The skin depth is merely $\delta^*_m = 0.0023$ m (Table 4.1) compared to the melt diameter $R^* = 0.01275$ m. Thus, $\mathbf{F}^*_{\text{EM}}$ is not present in the majority of the melt.

However, higher AC frequencies f^*_{ext} do increase the maximum $\mathbf{F}^*_{\text{EM}}$. For example, the estimated maximum $\langle \mathbf{F}^*_{\text{EM}} \rangle$ magnitude increases from a very weak 0.008 N/m^3 at $f^*_{\text{ext}} = 0.1$ Hz (Figure 4.6), to a strong 106 N/m^3 at $f^*_{\text{ext}} = 50$ kHz (Figure 4.15). Taking advantage of higher AC frequencies, the $\mathbf{B}^*_{\text{ext}}$ magnitude can be reduced (compared to lower AC frequencies) while achieving the same strong body force.

Moreover, the induced electromagnetic body force is fully three-dimensional at

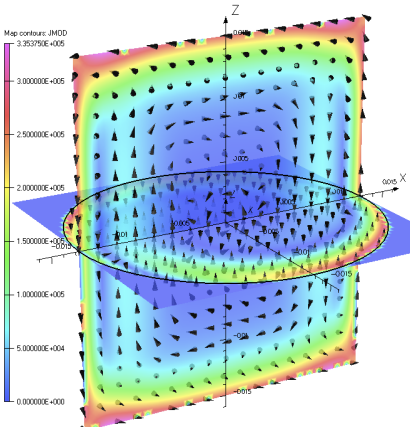

(a) $\mathbf{j}^*$ induced near the surface

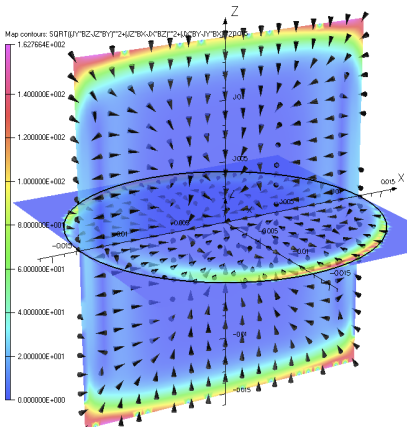

(b) $\mathbf{F}^*_{\mathrm{EM}}$ within a shallow skin depth

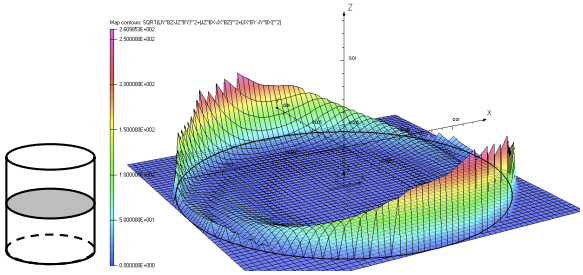

(c) $\mathbf{F}^*_{\mathrm{EM}}$ magnitude is largest within the skin depth but almost zero at the interior of the melt.

Figure 4.14 : The induced $\mathbf{j}^*$ and $\mathbf{F}^*_{\mathrm{EM}}$ fields within the melt when exposed to a rotating magnetic field of a very high $f^*_{\mathrm{ext}} = 50$ kHz (at 0 degrees of an AC cycle when $\mathbf{B}^*_{\mathrm{ext}}$ points to the $+\hat{\mathbf{e}}_x$ direction).

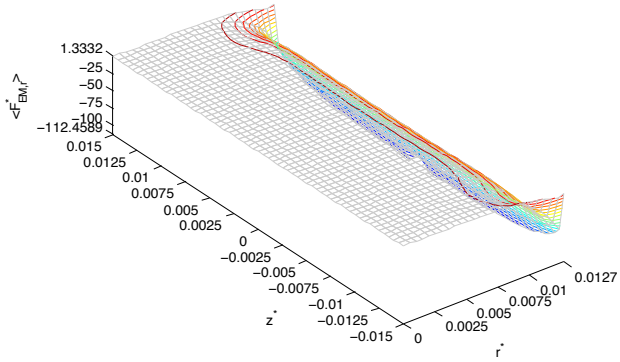

(a) $\langle F^*_{\mathrm{EM},r} \rangle$

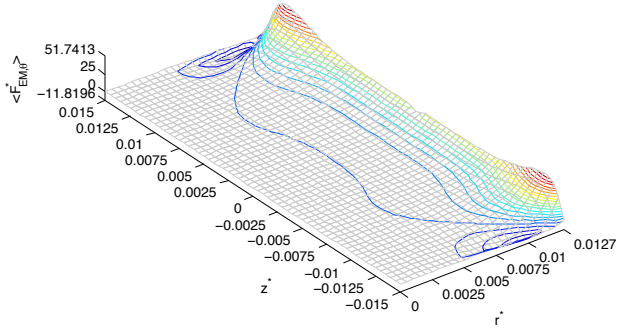

(b) $\langle F^*_{\mathrm{EM},\theta} \rangle$

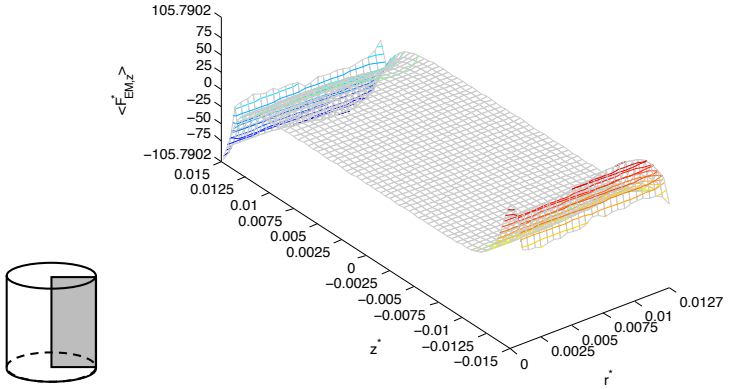

(c) $\langle F^*_{\mathrm{EM},z} \rangle$

Figure 4.15 : The time-averaged electromagnetic body force $\langle \mathbf{F}^*_{\mathrm{EM}} \rangle$ has significant components in all three directions, but only near the boundaries, at the very high AC frequency $f^*_{\mathrm{ext}} = 50$ kHz. All three vertical axes are scaled by the same magnitude.

very high AC frequency (see Figure 4.15). The flow is driven not only in the azimuthal direction by also in axial and radial directions by forced convection. The secondary meridional flow may be as strong as the primary azimuthal flow, which enhances radial and axial composition uniformity of components during crystal growth, but may also be well into the turbulent flow region.

Therefore, for magnetic stirring in crystal growth applications, the desired AC frequency should be high enough to induce a sufficiently strong body force, but not so high as to succumb to excessive magnetic shielding effects.

Chapter 5

Conclusions

Flow control by an electromagnetic body force during crystal growth from a melt is modeled numerically in this work. Two magnetic control mechanisms are discussed – *magnetic damping* and *magnetic stirring*.

Magnetic Damping

Magnetic damping is useful when excess flow within the melt is undesirable. For example, during the *optically-heated float-zone crystal growth process*, a quiescent molten region provides ideal growth conditions, so long as the temperature gradient is sufficient to avoid the morphological instability. If total quiescence cannot be achieved, an axisymmetric steady base flow state is acceptable for single crystalline growth, especially if a stagnant core region can be formed. Unfortunately, more complex three-dimensional and/or time-dependent flow patterns develop due to the inevitable *Marangoni convection* originated at the free surface. To damp these unwanted flow motions, an external steady magnetic field in the axial direction can be employed for float-zone crystal growth. The induced electromagnetic body force opposes flow motion perpendicular to the external magnetic field direction. As a result, the convection in the interior is opposed and the flow is confined in a narrow layer near the free surface of the liquid bridge. More importantly, a quiescent interior region results where uniform, defect-free crystal growth can occur.

The *Marangoni effect*, important physics for crystal growth with a free surface,

refers to the development of surface tension gradients along the melt-gas interface. During the optically-heated float-zone crystal growth process, this surface tension gradient results from a temperature gradient along the free surface. Therefore it is specifically referred to as the *thermocapillary effect*. During experiments, the Marangoni convection is directly related to the overall heat input, which is controlled by the heating lamp wattage. It drives a flow within the liquid bridge, *i.e.* the Marangoni convection, for which the intensity is measured by the *thermocapillary Reynolds number* Re_{FZ}, where the subscript FZ refers to the Full-Zone model of the liquid bridge. The nondimensional number Re_{FZ} measures the thermocapillary-induced shear stress intensity relative to the viscous effects. Intuitively, $Re_{FZ} \to 0$ represents a stagnant melt with virtually no thermocapillary driving. Re_{FZ} up to 2×10^5 are studied, which correspond to very intense but still laminar flow motion with the melt.

The material property *Prandtl number*, Pr, characterizes the heat transfer mechanism in the melt. Molten semiconductors grown using the float-zone technique typically have small Pr, for which heat conduction is dominant. For example, the Prandtl number of molten silicon, a material commonly studied and of great commercial value, is 0.02. In the limit of $Pr \to 0$, the thermal energy is distributed purely by conduction. In other words, the temperature distribution is unaffected by the flow convection (which would simplify computational efforts because the temperature field decouples from the flow field). Simulations presented here suggest that the $Pr = 0.001$ liquid bridge is a good representation for the limit of $Pr \to 0$, at least over the range $Ha \in [0, 300]$. To the contrary, convective heat transfer is dominant for $Pr > 1$ materials, often used in Marangoni studies in the Half-Zone liquid bridge configuration.

The *magnetic damping* effectively confines the Marangoni convection to near the free surface when the melt is exposed to a steady axial magnetic field of sufficient strength. Any radial or azimuthal flow motion in the liquid bridge is damped by the electromagnetic body force. The electromagnetic body force increases quadratically with the magnetic flux density $\mathbf{B}^*_{\text{ext}}$. As a consequence, the thickness of the (outermost) primary "circulation layer" or "circulation cell" is found to shrink with the external magnetic field strength approximately as $Ha^{-0.51}$ for $Pr = 0.02$ and $Ha^{-0.66}$ for $Pr = 0.001$. This observation is of great practical importance, because after a crystal rod is grown, experimentalists will often remove the outermost layer, which inevitably develops defects due to the local intense flow. Only the more uniform interior is processed into electro-optical devices. Magnetic damping reduces the thickness of the outermost layer and leaves more space for the uniform interior region. The magnetic damping effect is quantified by the *Hartmann number*, Ha, which measures the electromagnetic force relative to viscous effects. Aside from the primary circulation cell near the free surface, more circulation cells developed in the interior due to viscous effects when the liquid bridge is subject to magnetic damping. However the local extremum (maximum or minimum) value of the stream function in each circulation cell drops one to two orders of magnitude as compared to its outer neighbor. This suggests that the interior of the liquid bridge can be made effectively quiescent with a sufficiently strong magnetic field, ideal for crystal growth.

Flow instabilities in the context of the thermocapillary liquid bridge refer to more complex flow patterns that emerge above the steady axisymmetric base flow state due to enhanced Marangoni driving. The onset of instabilities, measured by the *critical thermocapillary Reynolds number* $Re_{FZ,cr}$, provides a quantitative reference for float-zone crystal growers on the upper limit of heat input allowable. $Re_{FZ,cr}$

is obtained within the range $Ha \in [0, 300]$ for $Pr = 0.02$, and also $Ha \in [0, 500]$ for $Pr = 0.001$ for a typical Full-Zone liquid bridge. For both Pr's, at their upper limits of Ha, $Re_{FZ,cr}$ increases by two orders of magnitude compared to ones without magnetic damping (*i.e.* at $Ha = 0$). This demonstrates that, with magnetic damping, flow instabilities are greatly suppressed so that much more thermal energy is allowed into the liquid bridge while the base flow state is still maintained.

In addition, flow instabilities in the Full-Zone liquid bridge are investigated with regard to developing a fundamental understanding of Marangoni convection. Using *normal mode linear stability analysis*, a wide range of basis instability modes are allowed to perturb the base state. Each basis instability mode is allowed to 1) perturb in any pattern within the $r \times z$ plane, 2) vary sinusoidally in the azimuthal direction, denoted by the *azimuthal wave number* m, 3) exhibit axial symmetries of perturbations which are either the same as the base flow variables (the *symmetric modes*), or the opposite (the *anti-symmetric modes*), and 4) oscillate in time, or be stationary.

Results show that the $Pr = 0.02$ liquid bridge always first transitions into stationary, anti-symmetric, three-dimensional instabilities for $Ha \in [0, 300]$. However, within this range, the critical azimuthal wave number m_{cr} increases from 2 for $Ha \leq 10$, to $m_{cr} = 3$ for $15 < Ha < 30$, to $m_{cr} = 4$ for $Ha \geq 40$. In other words, magnetic damping not only suppresses the onset of instabilities, but also changes the type of the first instability.

Flow instabilities for the $Pr = 0.001$ liquid bridge, representing $Pr \to 0$, are also investigated up to $Ha = 500$. The base flow first transitions to stationary, *anti-symmetric*, three-dimensional instabilities below $Ha = 40$. Above $Ha = 50$ and until $Ha = 500$ (the upper limit in this work), the base flow first transitions to stationary, *symmetric*, three-dimensional instabilities. The critical azimuthal wave

number increases from $m_{cr} = 2$ at $Ha = 0$ to $m_{cr} = 16$ at $Ha = 500$ due to magnetic damping.

The linear stability analysis also provides fundamental insights into liquid bridge flow instabilities. The knowledge on potential instability modes is helpful in explaining experimental observations and even predicting possible flow instabilities under new conditions. For example, the linear stability analysis indicates that an apparent secondary "periodic instability" observed in transient three-dimensional simulations is actually competition between two stationary basis instability modes. Moreover, the linear stability analysis and the energy analysis reveal the instability mechanism for the low Pr liquid bridge to be small perturbations which develop within the shear flow regions – instabilities which are *hydrodynamic* in nature. In contrary, for large Pr liquid bridges studied elsewhere, convective heat transfer is dominant and the instability mechanism is *hydrothermal*, resulting in periodic flow.

Magnetic Stirring

Magnetic stirring is useful to enhance mixing between components during binary and ternary semiconductor crystal growth. Elements in molten ternary semiconductors, such as GaInSb, often exhibit very slow diffusion rates, but are required to equilibrate at the growth front such that compositional homogeneity in the grown crystal can be maintained. Without magnetic stirring, typical growth rates are merely a few millimeters per hour or even per day.

When the electrically conducting melt is exposed to an external alternating magnetic field, an electric current is induced in a direction perpendicular to the magnetic field at any time instance. Subsequently, the Lorentz body force is induced within the molten material, which also alternates in time. Alternating current (AC) frequencies in

crystal growth applications are typically moderate, $O(100\text{ Hz})$, to high, $O(1\text{ kHz})$. The electromagnetic field alternates much faster than the flow can instantaneously respond. Instead, the flow "feels" a time-averaged electromagnetic body force. This electromagnetic body force drives convection within the molten material, which transports elements at a much faster rate than diffusion.

The *Bridgman technique* and the *traveling heater method* are excellent examples of crystal growth methods where magnetic stirring is applicable. Molten semiconductor materials are confined within an ampule, which is exposed to an external, transverse (parallel to the growth front) rotating magnetic field. Similar to magnetic damping, the stirring body force increases quadratically with $\mathbf{B}^*_{\text{ext}}$. Moreover, the rotating (AC) frequency f^*_{ext} is another key parameter, which affects:

1. the *magnetic skin depth* $\delta^*_m = \sqrt{2/(\mu^*_p \sigma^* 2\pi f^*_{\text{ext}})}$, which measures how deep into the electrically conducting media the external magnetic field penetrates. The skin depth decreases as AC frequency increases, $\delta^*_m \sim (f^*_{\text{ext}})^{-1/2}$. When the skin depth is smaller than the melt radius at high AC frequencies, the *magnetic shielding effect* emerges, *i.e.* the interior region below the skin depth is not directly impacted by the external magnetic field. The magnetic field takes time to propagate into the electrically conducting media, analogous to the time required for heat conduction. At very high AC frequencies, the magnetic field only diffuses into a thin skin depth into the melt within the very short AC cycle. The magnetic flux lines are also drastically distorted at high AC frequencies, such that the magnetic field is almost absent in the interior.

2. the magnitude of the electromagnetic body force, which is strongest near the boundaries, where the magnetic field and induced electric current are strongest.

In the *low frequency approximation* the analytical solution of the electromagnetic body force is available for a few simple geometries, so long as the when induced magnetic fields are also negligible, *i.e.* the magnetic Reynolds number is also small. For an infinitely-long, electrically conducting, cylindrical melt exposed to a uniform transverse rotating magnetic field, the time-averaged body force is axisymmetric and purely in the azimuthal direction, $\langle F^*_{\mathrm{EM},\theta} \rangle = \sigma^* B_0^{*2} \omega^*_{\mathrm{ext}} r^*/2$, where the angular frequency $\omega^*_{\mathrm{ext}} = 2\pi f^*_{\mathrm{ext}}$. For a conducting cylindrical melt with finite length, the time-averaged body force is also axisymmetric and only in the azimuthal direction. This body force is strongest at the half-length of the melt near the wall of the ampule. Furthermore, the body force increases linearly with the AC frequency, at least in the low AC frequency range. Therefore with a moderate AC frequency, a weaker magnetic field can maintain the same magnitude of body force as a slower, stronger field. Thus magnetic stirring at moderate AC frequencies can be more energy efficient.

3. the direction of the electromagnetic body force, which is primarily azimuthal at low AC frequencies. In contrary, the force field is fully three-dimensional at high AC frequencies. In the example of $f^*_{\mathrm{ext}} = 50$ kHz, the axial and radial forces are even stronger than the azimuthal force in some areas. However the body forces only present near the boundaries due to the strong magnetic shielding effect at high AC frequencies. Fully three-dimensional stirring can enhance mixing between chemical elements in the melt, especially in the axial direction.

Therefore, for magnetic stirring in crystal growth applications, the desired AC frequency should be high enough to induce a sufficiently strong body force, but not too high such that excessive magnetic shielding is avoided.

The dominant azimuthal body force drives a *primary flow* in the azimuthal direction. Due to the viscous boundary layer near the ampule wall, the fastest flow does not occur at the location of the maximum body force. Instead the fastest flow is slightly interior from the ampule wall and near the mid-plane. Moreover, the azimuthal flow strengthens less than linearly with the AC frequency, observed at least up to 100 Hz for a typical melt configuration. The primary flow also gradually shifts toward the ampule wall and melting and solidification fronts as the AC frequency increases. The centripetal acceleration of the primary flow is balanced by a radial pressure gradient.

Superimposed onto the primary flow, a *secondary flow* in the meridional plane (v_r^* and v_z^*) develops due to continuity. This secondary flow circulations from the mid-plane toward the two end walls near the outer radius of the melt, then circulates back to the mid-plane in the interior. When stirred at low to moderate AC frequencies (up to about 1 kHz for a typical melt cylinder, and confirmed up to 100 Hz in this work), the flow in a conducting cylindrical melt is steady, axisymmetric, and symmetric with respect to the mid-plane.

In summary, two "contradicting" control mechanisms – magnetic damping and magnetic stirring – have distinct purposes in bulk crystal growth from a melt. For example, magnetic damping helps to minimize striations in the grown crystal by creating a quiescent region in the interior of the melt. Magnetic stirring can be used to enhance compositional (and dopant) uniformity within the melt and subsequently in the grown crystal. These two fundamental mechanisms open up possibilities for more refined magnetic control for melt crystal growth. For example, in the traveling heater method, more sophisticated magnetic stirring may be arranged to drive specific forced convection to effectively transport preferentially solidified elements to the growth front. Moreover, the molten material could be first stirred for an accelerated mixing

between chemical components, then damped to quiescent for crystallization with minimal defects. This alternating process may be repeated if necessary. By regulating the flow in the melt, magnetic control can improve grown-crystal properties in new materials, and achieve economically viable growth rates for commercial production of novel crystalline semiconductors and alloys.

Bibliography

[Anderson et al., 1999] Anderson, E., Bai, Z., Bischof, C., Blackford, S., Demmel, J., Dongarra, J., Du Croz, J., Greenbaum, A., Hammarling, S., McKenney, A., and Sorensen, D. (1999). Linear Algebra PACKage.

[Bouizi et al., 2007] Bouizi, O., Delcarte, C., and Kasperski, G. (2007). Stability study of the floating zone with respect to the Prandtl number value. *Physics of Fluids*, 19(11):114102.

[Brown et al., 1963] Brown, G. V., Flax, L., Itean, E. C., and Laurence, J. C. (1963). Axial and radial magnetic fields of thick, finite-length solenoids. Technical Report NASA-TR-R-170, Lewis Research Center, National Aeronautics and Space Administration, Cleveland, Ohio.

[Byrappa and Pushcharovsky, 1992] Byrappa, K. and Pushcharovsky, D. (1992). Crystal chemistry and its significance on the growth of technological materials: Part I; silicates, phosphates and their analogues. *Progress in Crystal Growth and Characterization of Materials*, 24(4):269–359.

[Callaghan and Maslen, 1960] Callaghan, E. E. and Maslen, S. H. (1960). The magnetic field of a finite solenoid. Technical Report NASA-TN-D-465, Lewis Research Center, National Aeronautics and Space Administration, Cleveland, Ohio.

[Capper, 2005] Capper, P. (2005). *Bulk crystal growth of electronic, optical & optoelectronic materials*. John Wiley and Sons.

[Chen et al., 1997] Chen, G., Lizée, A., and Roux, B. (1997). Bifurcation analysis of the thermocapillary convection in cylindrical liquid bridges. *Journal of Crystal Growth*, 180(3-4):638 – 647.

[Cröll et al., 1994] Cröll, A., Dold, P., and Benz, K. W. (1994). Segregation in Si floating-zone crystals grown under microgravity and in a magnetic field. *Journal of Crystal Growth*, 137(1-2):95 – 101.

[Cröll et al., 1998a] Cröll, A., Kaiser, T., Schweizer, M., Danilewsky, A. N., Lauer, S., Tegetmeier, A., and Benz, K. W. (1998a). Floating-zone and floating-solution-zone growth of GaSb under microgravity. *Journal of Crystal Growth*, 191(3):365–376.

[Cröll et al., 1998b] Cröll, A., Szofran, F. R., Dold, P., Benz, K. W., and Lehoczky, S. L. (1998b). Floating-zone growth of silicon in magnetic fields. ii. strong static axial fields. *Journal of Crystal Growth*, 183(4):554 – 563.

[Davidson, 1999] Davidson, P. A. (1999). Magnetohydrodynamics in materials processing. *Annual Review of Fluid Mechanics*, 31(1):273–300.

[Davidson, 2001] Davidson, P. A. (2001). *An introduction to magnetohydrodynamics*. Cambridge University Press.

[Davis, 2011] Davis, K. E. (2011). Three-dimensional, time-dependent spectral element simulations of a thermocapillary liquid bridge with magnetic stabilization. Master's thesis, Rice University.

[Davis et al.,] Davis, K. E., Huang, Y., and Houchens, B. C. Transitions predicted by three-dimensional time integration compared with linear stability theory for a thermocapillary driven full-zone liquid bridge. *In revision for Physics of Fluids*.

[Davis, 1993] Davis, S. H. (1993). *Handbook of Crystal Growth*. Elsevier Science Publisher, New York, NY.

[Dhanaraj et al., 2010] Dhanaraj, G., Byrappa, K., Prasad, V., and Dudley, M. (2010). *Springer Handbook of Crystal Growth*. Springer.

[Dold, 2004] Dold, P. (2004). Analysis of microsegregation in RF-heated float zone growth of silicon – comparison to the radiation-heated process. *Journal of Crystal Growth*, 261(1):1–10.

[Embree and Trefethen, 2012] Embree, M. and Trefethen, L. N. (2012). Pseudospectra gateway. http://www.comlab.ox.ac.uk/pseudospectra.

[Eyer et al., 1985] Eyer, A., Leiste, H., and Nitsche, R. (1985). Floating zone growth of silicon under microgravity in a sounding rocket. *Journal of Crystal Growth*, 71(1):173 – 182.

[Grants and Gerbeth, 2002] Grants, I. and Gerbeth, G. (2002). Linear three-dimensional instability of a magnetically driven rotating flow. *Journal of Fluid Mechanics*, 463:229–239.

[Houchens, 2005] Houchens, B. C. (2005). *Multi-scale model of the stability of a laterally heated liquid bridge under the influence of an axial magnetic field*. PhD thesis, University of Illinois at Urbana-Champaign.

[Houchens et al., 2009] Houchens, B. C., Becla, P., Tritchler, S. E., Goza, A. J., and Bliss, D. F. (2009). Crystal growth of bulk ternary semiconductors. In *American Crystal Growth Conference*, Lake Geneva, WI.

[Houchens et al., 2010] Houchens, B. C., Becla, P., Tritchler, S. E., Goza, A. J., and Bliss, D. F. (2010). Crystal growth of bulk ternary semiconductors: Comparison of GaInSb growth by horizontal bridgman and horizontal traveling heater method. *Journal of Crystal Growth*, 312(8):1090–1094.

[Houchens and Walker, 2001] Houchens, B. C. and Walker, J. S. (2001). Magnetic damping of the thermocapillary instability during floating-zone crystal growth in space. In *Conference and Exhibit on International Space Station Utilization- 2001, Cape Canaveral, FL*.

[Houchens and Walker, 2005] Houchens, B. C. and Walker, J. S. (2005). Modeling the floating zone: Instabilities in the Half Zone and full Zone. *Journal of Thermophysics and Heat Transfer*, 137(2):186 – 198.

[Huang, 2009] Huang, Y. (2009). High resolution numerical study of a liquid bridge Marangoni flow with applied axial magnetic field for low Prandtl number fluids. Master's thesis, Rice University.

[Huang and Houchens, 2011a] Huang, Y. and Houchens, B. C. (2011a). Magnetic stabilization, transition and energy analysis in the Marangoni driven Full-Zone at low Prandtl numbers. *The European Physical Journal Special Topics*, 192(1):47–61.

[Huang and Houchens, 2011b] Huang, Y. and Houchens, B. C. (2011b). Numerical modeling of thermocapillary driven liquid bridge with magnetic stabilization. *Journal of Mechanics of Materials and Structures*, 6(7-8):995–1061.

[Intel®, 2008] Intel®(2008). Intel® Math Kernel Library.

[Kahouadji et al., 2011] Kahouadji, L., Houchens, B. C., and Witkowski, L. M. (2011). Thermocapillary instabilities in a laterally heated liquid bridge with end wall rotation. *Physics of Fluids*, 23(10):104104–104104–16.

[Kasperski et al., 2000] Kasperski, G., Batoul, A., and Labrosse, G. (2000). Up to the unsteadiness of axisymmetric thermocapillary flows in a laterally heated liquid bridge. *Physics of Fluids*, 12:103–119.

[Kawamura et al., 2010] Kawamura, H., Nishino, K., Matsumoto, S., and Ueno, I. (2010). Space experiment of Marangoni convection on International Space Station. In *Proceedings of the 2010 14th International Heat Transfer Conference, ASME paper IHTC14-23346*, volume 8, pages 343–362, Washington, DC, USA.

[Kimura et al., 1983] Kimura, H., Harvey, M. F., O'Connor, D. J., Robertson, G. D. J., and Valley, G. C. (1983). Magnetic field effects on float-zone si crystal growth. *Journal of Crystal Growth*, 62(3):523–531.

[Kuhlmann and Nienhuser, 2002] Kuhlmann, H. C. and Nienhuser, C. (2002). Dynamic free-surface deformations in thermocapillary liquid bridges. *Fluid Dynamics Research*, 31(2):103–127.

[Lappa, 2005a] Lappa, M. (2005a). Analysis of flow instabilities in convex and concave floating zones heated by an equatorial ring under microgravity conditions. *Computers & Fluids*, 34(6):743–770.

[Lappa, 2005b] Lappa, M. (2005b). Review: Possible strategies for the control and stabilization of Marangoni flow in laterally heated floating zones. *Fluid Dynamics & Materials Processing*, 1(2):171–188.

[Levenstam and Amberg, 1995] Levenstam, M. and Amberg, G. (1995). Hydrodynamical instabilities of thermocapillary flow in a half-zone. *Journal of Fluid Mechanics*, 297:357–372.

[Levenstam et al., 2001] Levenstam, M., Amberg, G., and Winkler, C. (2001). Instabilities of thermocapillary convection in a half-zone at intermediate Prandtl numbers. *Physics of Fluids*, 13(4):807–816.

[Leypoldt et al., 2000] Leypoldt, J., Kuhlmann, H. C., and Rath, H. J. (2000). Three-dimensional numerical simulation of thermocapillary flows in cylindrical liquid bridges. *Journal of Fluid Mechanics*, 414:285–314.

[Li et al.,] Li, H., Huang, Y., and Houchens, B. C. Spectral collocation numerical issues in cylindrical domains, investigated via the laterally heated Full-Zone with an applied magnetic field. under review for Fluid Dynamics & Materials Processing.

[Martinez and Eyer, 1986] Martinez, I. and Eyer, A. (1986). Liquid bridge analysis of silicon crystal growth experiments under microgravity. *Journal of Crystal Growth*, 75(3):535–544.

[Mazuruk et al., 1997] Mazuruk, K., Ramachandran, N., Volz, M. P., and Gillies, D. C. (1997). Study of frequency effects of a rotating magnetic field on fluid flow in vertical cylinders. *Proceedings of SPIE*, 3123(1):262–271.

[Moreau, 1990] Moreau, R. (1990). *Magnetohydrodynamics*. Springer.

[Nakamura et al., 1998] Nakamura, S., Hibiya, T., Kakimoto, K., Imaishi, N., Nishizawa, S., Hirata, A., Mukai, K., Yoda, S., and Morita, T. S. (1998). Temperature fluctuations of the marangoni flow in a liquid bridge of molten silicon

under microgravity on board the TR-IA-4 rocket. *Journal of Crystal Growth*, 186(1-2):85–94.

[Patera, 1984] Patera, A. T. (1984). A spectral element method for fluid dynamics: Laminar flow in a channel expansion. *Journal of Computational Physics*, 54(3):468–488.

[Prange et al., 1999] Prange, M., Wanschura, M., Kuhlmann, H. C., and Rath, H. J. (1999). Linear stability of thermocapillary convection in cylindrical liquid bridges under axial magnetic fields. *Journal of Fluid Mechanics*, 394(1):281 – 302.

[Reddy and Trefethen, 1990] Reddy, S. C. and Trefethen, L. N. (1990). Lax-stability of fully discrete spectral methods via stability regions and pseudo-eigenvalues. *Computer Methods in Applied Mechanics and Engineering*, 80(1-3):147–164.

[Robertson and O'Connor, 1986] Robertson, G. D. J. and O'Connor, D. (1986). Magnetic field effects on float-zone Si crystal growth: III. strong axial fields. *Journal of Crystal Growth*, 76(1):111 – 122.

[Schwabe et al., 2007] Schwabe, D., Mizev, A. I., Udhayasankar, M., and Tanaka, S. (2007). Formation of dynamic particle accumulation structures in oscillatory thermocapillary flow in liquid bridges. *Physics of Fluids*, 19:072102.

[Shen et al., 1996] Shen, X. F., Anilkumar, A. V., Grugel, R. N., and Wang, T. G. (1996). Utilizing vibration to promote microstructural homogeneity during floating-zone crystal growth processing. *Journal of Crystal Growth*, 165(4):438–446.

[Shyy and Rao, 1995] Shyy, W. and Rao, M. M. (1995). Calculation of meniscus shapes and transport processes in float zone. *International Journal of Heat and Mass Transfer*, 38(12):2281–2295.

[Simic-Stefani et al., 2006] Simic-Stefani, S., Kawaji, M., and Yoda, S. (2006). Onset of oscillatory thermocapillary convection in acetone liquid bridges: The effect of evaporation. *International Journal of Heat and Mass Transfer*, 49(17-18):3167–3179.

[Takagi et al., 2001] Takagi, K., Otaka, M., Natsui, H., Arai, T., Yoda, S., Yuan, Z., Mukai, K., Yasuhiro, S., and Imaishi, N. (2001). Experimental study on transition to oscillatory thermocapillary flow in a low Prandtl number liquid bridge. *Journal of Crystal Growth*, 233(1-2):399–407.

[Tanaka et al., 2006] Tanaka, S., Kawamura, H., Ueno, I., and Schwabe, D. (2006). Flow structure and dynamic particle accumulation in thermocapillary convection in a liquid bridge. *Physics of Fluids*, 18:067103.

[Teng et al., 2010] Teng, Y., Chen, J., Lu, C., and Chen, C. (2010). The carbon distribution in multicrystalline silicon ingots grown using the directional solidification process. *Journal of Crystal Growth*, 312(8):1282–1290.

[Trefethen et al., 1993] Trefethen, L. N., Trefethen, A. E., Reddy, S. C., and Driscoll, T. A. (1993). Hydrodynamic stability without eigenvalues. *Science*, 261(5121):578–584.

[Vector Fields Limited, 2007] Vector Fields Limited (2007). Vector Fields Opera 3D Reference Manual. `http://www.vectorfields.com`.

[Wanschura et al., 1995] Wanschura, M., Shevtsova, V. M., Kuhlmann, H. C., and Rath, H. J. (1995). Convective instability mechanisms in thermocapillary liquid bridges. *Physics of Fluids*, 7(5):912.

[Witkowski et al., 1999] Witkowski, M. L., Walker, J. S., and Marty, P. (1999). Non-axisymmetric flow in a finite-length cylinder with a rotating magnetic field. *Physics of Fluids*, 11(7):1821.

[Yang and Kou, 2001] Yang, Y. K. and Kou, S. (2001). Temperature oscillation in a tin liquid bridge and critical Marangoni number dependency on Prandtl number. *Journal of Crystal Growth*, 222(1-2):135–143.

[Yano et al., 2011] Yano, T., Nishino, K., Kawamura, H., Ueno, I., Matsumoto, S., Ohnishi, M., and Sakurai, M. (2011). Space experiment on the instability of Marangoni convection in large liquid bridge - MEIS-4: effect of Prandtl number -. *Journal of Physics: Conference Series*, 327:012–029.

Appendix A

Numerical Considerations in Liquid Bridge Modeling

A.1 Regularization Dependence

The vorticity singularity at the corner $(r, z) = (1, b)$ is removed by applying a *regularization function* $F(z)$ in Subsection 3.2.2 (repeating Equation 3.18 here)

$$F(z) = 1 - \exp\left\{-\alpha\left[1 - \left(\frac{z}{b}\right)^2\right]^2\right\}.$$

An optimum *regularization parameter* α is found when increasing α further has no measurable impact on the flow and the singularity is effectively removed. Figure A.1 shows an example of searching for the "desired range" of α. The v_{r0} contours at $\alpha = 50,000$ bear wiggles and circles, which suggests insufficient regularization. Therefore $\alpha = 50,000$ is too large. With even larger α's (less smoothing), the vorticity singularity may cause the numerical solver to predict incorrect physics, indicated by the sudden drop of the critical Re_{FZ} beyond $\alpha = 100,000$. On the other hand, if α is too small, the regularization effectively reduces the heat input at the free surface, which reduces the driving force. This explains the increase of the critical Re_{FZ} in the small α range ("too much regularization") in Figure A.1. The "desired range" of α is found between 300 to 8,000 for this test where the physics is considered independent of α.[1]

[1] Let us define z being "affected" if $F(z)$ drops below 0.99. Then $\alpha = 300$ affects $z/b \in [0.938, 1]$ (5

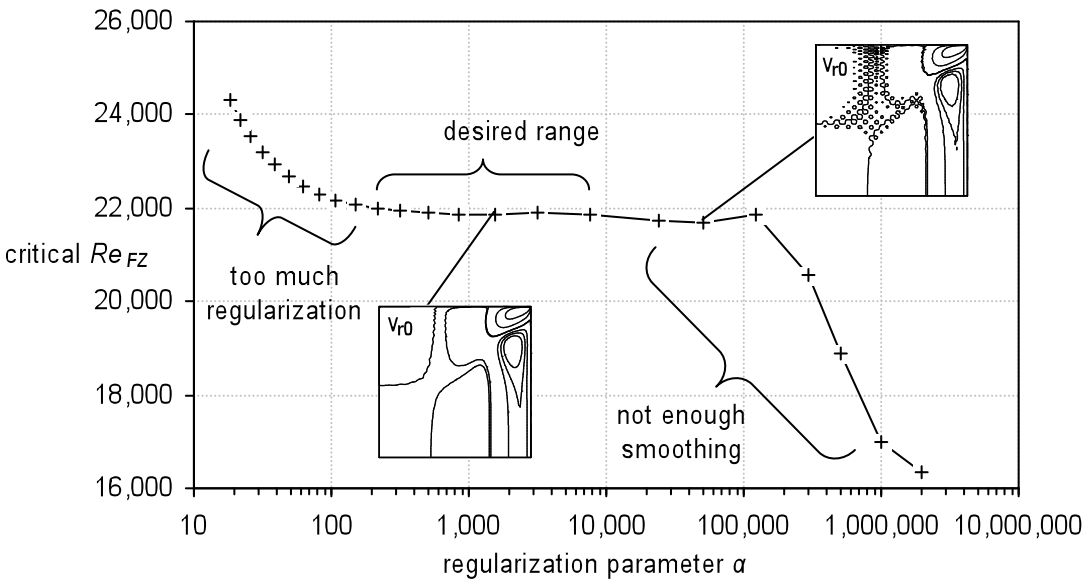

Figure A.1 : Searching for the desired range of regularization parameter α in Equation 3.18 (a semi-log plot, $Pr = 0.02$, $Ha = 50$, flow grid $NRF \times NZF = 40 \times 40$, temperature grid $NRT \times NZT = 30 \times 30$, stability grid $NR \times NZ = 40 \times 40$) [Huang and Houchens, 2011b]; reprinted with permission.

A fast decaying regularization function is especially important for larger Pr's. Due to strong heat convection at large Pr, the free surface temperature varies slowly along $r = 1$ until very close to $(r, z) = (1, b)$. This physics is best preserved by a regularization function that decays quickly near $(r, z) = (1, b)$. The choice of regularization function is arbitrary, as long as the singularity is removed with minimum alternation to the physics. For example, [Bouizi et al., 2007] adopted a power function regularization function $F(z) = (1 - z^{2n})^2$, where n is a regularization parameter.

collocation points including $z = b$). $\alpha = 8,000$ affects $z/b \in [0.988, 1]$ (10 collocation points including $z = b$). Note there are 41 Gauss-Lobatto collocation points for $z \in [0, b]$.

A.2 Grid Dependence

A solution which does not vary with significant further grid refinement indicates that the grid resolution is sufficient and the results are reliable. Table A.1 shows such a test based on the critical thermocapillary number $Re_{FZ,cr}$. Significant resolution increases are introduced for the base flow grids and the linear stability analysis grid, but the $Re_{FZ,cr}$ barely changes, demonstrating grid independence being achieved.

Table A.1 : A grid dependence study based on $Re_{FZ,cr}$ for $Pr = 0.02, Ha = 100$ and $\alpha = 400$ [Huang and Houchens, 2011b]; reprinted with permission.

$Re_{FZ,cr}$ for		stability grid $(r \times z)$ 34×60	50×70	% difference
flow grid, temperature grid	30×75, 25×25	61,775.37	61,840.74	**0.11%**
$(r \times z)$	70×100, 40×40	61,789.51	61,841.79	**0.08%**
% difference		**0.02%**	**0.002%**	

Nevertheless, more subtle inferences can be made from Table A.1. $Re_{FZ,cr}$ increased slightly on finer grids. This is expected because a fixed regularization parameter ($\alpha = 400$) affects more grid points on a finer axial grid than on a coarser axial grid. The thermocapillary effect is weakened at more collocation points on finer grids, therefore a higher $Re_{FZ,cr}$ is expected. However if this regularization effect were eliminated, $Re_{FZ,cr}$ would be lower on finer grids, because coarser grids tend to smear out the largest gradients, which contribute energy to the instability mechanism. On coarser grids, $Re_{FZ,cr}$ increases to compensate for this smearing effect until the energy is sufficient to trip the instability. Thus, in practice, it is necessary to carry out both grid and regularization dependence studies simultaneously. The regularization

parameter α must be increased as the grid is refined.

Furthermore, the coefficient series of Chebyshev polynomials for unknowns is another indication if the grid resolution is sufficient, because the grid resolution determines the number of terms (*i.e.* degrees of freedom) in these Chebyshev polynomials.

Two coefficient series of stream function ψ Chebyshev polynomials are plotted in Figure A.2. $|A_{LM}|$ is the absolute value of Chebyshev polynomial coefficients A_{LM} for stream function ψ in the liquid bridge base flow (repeating Equation 3.35)

$$\psi\left(r, \frac{z}{b}\right) = r^2 \sum_{L=0}^{NRF+1} \sum_{M=0}^{NZF+1} A_{LM} T_{2L}(r) T_{2M+1}\left(\frac{z}{b}\right).$$

As Figure A.2 shows, both coefficient series decay sub-exponentially. The Chebyshev term $T_{2L}(r)T_{2M+1}(z/b)$ in Equation 3.35 is always between -1 and 1, therefore leading polynomial terms with the largest coefficients contribute most to ψ. This translates to the most significant flow being represented by leading Chebyshev polynomial terms. As observed in experiments, the liquid bridge base flow is characterized by low spatial frequency flow pattern (comparable to the size of the liquid bridge). Higher order Chebyshev polynomial terms represent more subtle flow patterns of higher spatial frequencies. Figure A.2 demonstrates that these truncated Chebyshev polynomial series are sufficient spectral representations of the stream function. The *spectral convergence* is achieved.

A.3 Identifying Spurious Eigenvalues

In the normal mode linear stability analysis, unstable systems are identified by positive leading eigenvalues. However, some "spurious eigenvalues" (due to numerical artifacts, often with very large magnitudes) emerge in the generalized eigenvalue problem Equation 3.51, bearing no physical meaning regarding system stability. It is crucial

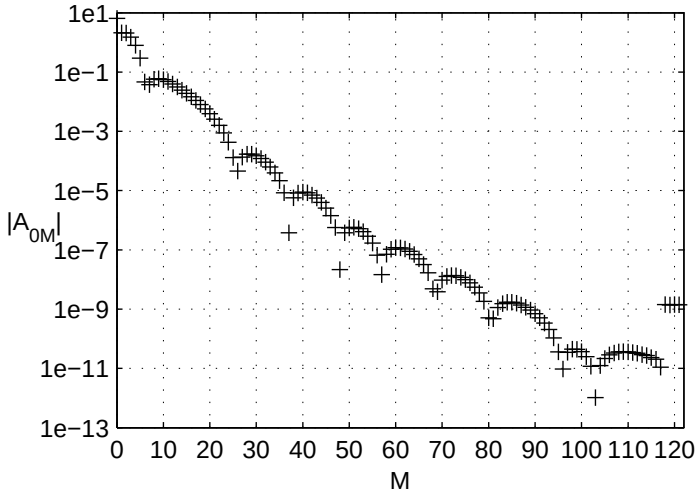

(a) $Pr = 0.02$ and $Ha = 100$ at $Re_{FZ,cr} = 61,747.38$, flow grid $r \times z = 110 \times 120$, temperature grid $r \times z = 80 \times 80$, $\alpha = 1200$

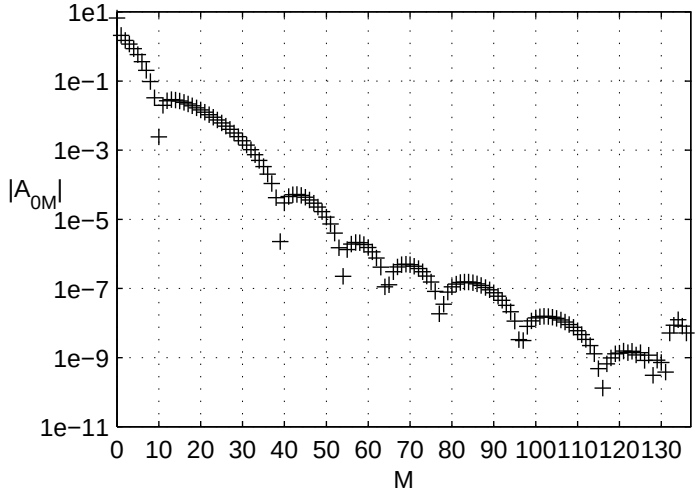

(b) $Pr = 0.02$ and $Ha = 300$ at $Re_{FZ,cr} = 259,068.47$, flow grid $r \times z = 125 \times 135$, temperature grid $r \times z = 80 \times 80$, $\alpha = 3000$

Figure A.2 : Sub-exponential decay of Chebyshev polynomial coefficients series A_{0M} demonstrates sufficient spectral representation of stream function ψ (a semi-log plot) ([Huang and Houchens, 2011a]; reprinted with permission).

to identify and separate them from the remaining legitimate eigenvalues to correctly predict the onset of instability.

Legitimate eigenvalues are independent of linear stability grid resolution. In Table A.2, to test if the leading eigenvalue pair $350.47 \pm 7542.09i$ on a $r \times z = 30 \times 40$ stability grid is legitimate or spurious, the linear stability code was run on two other grid sizes 28×28 and 40×50. The fact that $350.47 \pm 7542.09i$ not presented on these other two grids indicates it being a spurious eigenvalue. All other eigenvalues agree well across different grid sizes.

Table A.2 : Identification of a spurious eigenvalue (underlined in the table) through grid independence study of the linear stability analysis ($Pr = 0.001$, $Ha = 0$, $Re_{FZ} = 1000$, $m = 1$, $\alpha = 400$, symmetric instability mode) [Huang and Houchens, 2011b]; reprinted with permission.

grid size	$r \times z = 28 \times 28$	$r \times z = 30 \times 40$	$r \times z = 40 \times 50$
leading eigenvalues		$\underline{350.47 \pm 7542.09i}$	
	$-34.61 \pm 9.25i$	$-34.61 \pm 9.26i$	$-34.61 \pm 9.25i$
	$-94.58 \pm 110.75i$	$-94.58 \pm 110.75i$	$-94.58 \pm 110.75i$
	$-113.45 \pm 56.60i$	$-113.46 \pm 56.59i$	$-113.46 \pm 56.60i$
	$-129.35 \pm 175.31i$	$-129.35 \pm 175.31i$	$-129.35 \pm 175.31i$
	$-140.05 \pm 72.15i$	$-140.04 \pm 72.15i$	$-140.04 \pm 72.15i$
	$-197.10 \pm 320.75i$	$-197.10 \pm 320.75i$	$-197.10 \pm 320.75i$
	...	...	...

Flow perturbations corresponding to the spurious eigenvalue pair $350.47 \pm 7542.09i$ are plotted in Figure A.3a as another proof of the spuriousness. The checkerboard flow

pattern has no physical justification, but is rather an oscillation of high order modes in each direction between Gauss-Lobatto collocation points. This is clearly shown in its coefficient series plot (Figure A.3b). $\mathcal{A}_{LM}$'s are the Chebyshev polynomial coefficients of radial velocity perturbation v_{r1} (repeating Equation 3.43)

$$v_{r1}\left(r, \frac{z}{b}\right) = r^{m-1} \sum_{L=0}^{NR+1} \sum_{M=0}^{NZ} \mathcal{A}_{LM} T_{2L}(r) T_{2M}\left(\frac{z}{b}\right).$$

Figure A.3b shows that coefficients of the highest order Chebyshev terms have the largest magnitudes, which are responsible for the high spatial frequency oscillating contours. It has been shown in Appendix A.2 that, for a legitimate eigenvalue mode, Chebyshev polynomial coefficients decay sub-exponentially when the spectral representation is sufficient.

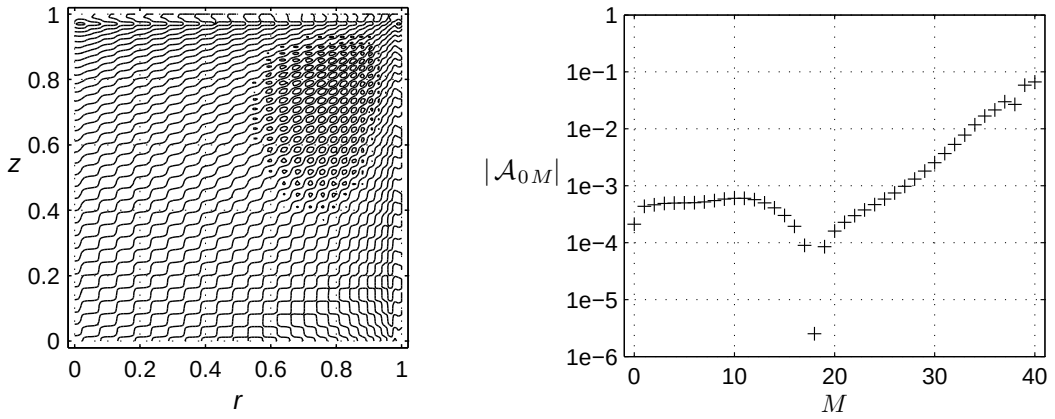

(a) v_{r1} contours

(b) Chebyshev polynomial coefficients plot for v_{r1}

Figure A.3 : Perturbation contours and Chebyshev polynomial coefficients associated with the spurious eigenmode $350.47 \pm 7542.09i$ in Table A.2 ($Pr = 0.001$, $Ha = 0$, $Re_{FZ} = 1000$, $m = 1$, $\alpha = 400$, linear stability grid $r \times z = 30 \times 40$) [Huang and Houchens, 2011b]; reprinted with permission.

Therefore for $Pr = 0.001$ and $Ha = 0$, the legitimate leading eigenvalue is a

complex pair with negative real part $-34.61 \pm 9.26i$ as shown in Table A.2. The base flow is stable at $Re_{FZ} = 1000$ for the branch of $m = 1$ symmetric instability mode.

Appendix B

Validations of the Opera Solver

It was necessary to validate the Opera Modeler in the Vector Fields software before using the resulting electromagnetic body forces for the rotating and traveling magnetic field cases. Several fundamental validation studies were carried out including: 1) determination of the magnetic flux density around a thin, finite-length solenoid (AC or DC), with the numerical solution compared to the analytical solution for an infinitely thin solenoid, 2) determination of the magnetic flux density around a thick, finite-length solenoid (AC or DC), with the numerical solution compared to an analytical solution 3) verification of the proper superposition of fields generated by multiple solenoids or coils, and 4) determination of the field between two and three sets of coils, driven out of phase at relatively low frequency to produce a rotating magnetic field in a short cylindrical conductor, with the numerical solution compared to an analytical solution. The last case is addressed in Subsection 4.1.1. The acceptable use of wedge symmetry and appropriate conditions on the boundaries were verified in all cases, allowing for mesh refinement. All studies validated Opera's ability to simulate the fields of interest, with the only deviation occurring very near the edges of the coils, which is not a critical location for the crystal growth systems studied.

A critical point relevant to all cases is that Opera requires some region to be specified as a "conductor." However, it is still possible to set the properties of the conductor to be essentially nonconducting. For example, in several cases presented here, the conductor was set to have the electric conductivity of air.

B.1 Magnetic Field of a Thin Solenoid with Finite Length

A solenoid generates a surrounding $\mathbf{B}^*$ field as in Figure B.1. This $\mathbf{B}^*$ field can be calculated by integrating over all electric current within the solenoid using the Biot-Savart law. An analytical solution has been derived for an infinitely thin solenoid with finite length, for example in [Callaghan and Maslen, 1960]. This section compares the $\mathbf{B}^*$ field of such a solenoid predicted in Opera with the analytical solution.

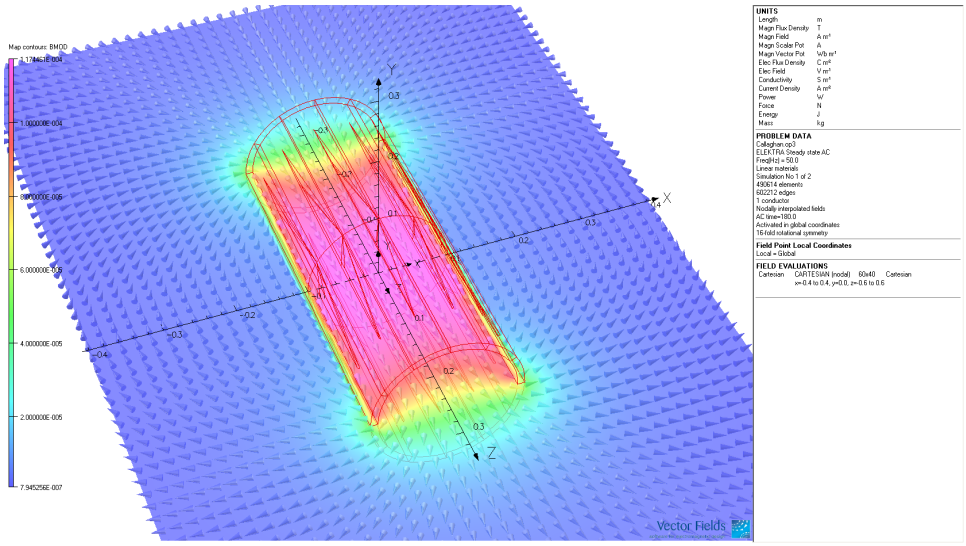

Figure B.1 : Magnetic flux density on a cutting plane generated by a thin, finite-length solenoid simulated in Opera. The solenoid is shown as the red cylinder framework (aspect ratio $L^*/R^* = 5$). The $\mathbf{B}^*$ on the cutting plane is shown by vectors (direction) and colors map (magnitude).

The radius of the cylindrical solenoid is R^*. Its length L^* is chosen to be $L^* = 5 \times R^*$. Because Opera does not allow a zero thickness solenoid, a small thickness, equal to $1/10^{\text{th}}$ of the radius R^*, is used in this benchmark. Using Opera, the $\mathbf{B}^*$ field is computed in the air surrounding the solenoid. Opera requires the existence of at least one conductor in the model, therefore a cylindrical "air conductor" (shown as

the green wedge in Figure B.2) is specified, but its properties are set to air (the sole purpose of which is to bypass the requirement that a conductor exists in the model). Later it is shown that this "air conductor" has no impact on the $\mathbf{B}^*$ field, as expected.

All result comparisons are nondimensionalized, but values used in the model are listed here for reference. The radius of the solenoid is $R^* = 0.1$ m. The length is $L^* = 0.5$ m and its thickness is 0.01 m. The (maximum) electric current density is 10,000 A/m^2 with alternating current (AC) frequency $f^*_{\text{ext}} = 50$ Hz.[1] The electric conductivity of the air is σ^*=0 S/m (siemens per meter, where siemens is the reciprocal of ohm) and the permeability is set to $\mu^*_p = \mu_0$. Therefore the magnetic Reynolds number $Re_m = 0$.

Due to axisymmetry, the computational domain is taken to be a $1/16^{\text{th}}$ cylindrical wedge (the gray wedge in Figure B.2[2]) with periodic boundary conditions set on both planar surfaces.[3] The computational domain has radius 0.42 m and length 2.4 m. The maximum mesh size is 0.01 m in both the "air conductor" and the rest of the domain

The magnetic flux density predicted by Opera is compared with the analytical solu-

---

[1] Readings are based on the maximum electric current density (10,000 A/m^2) within an AC cycle. Because the electric conductivity σ^* of the air is zero, the AC frequency f^*_{ext} has no impact on the $\mathbf{B}^*$ field distribution. The $\mathbf{B}^*$ field is perfectly diffused throughout the entire domain, because the magnetic shielding parameter $R_\omega = \mu^*_p \sigma^* \omega^*_{\text{ext}} L_0^{*2} = 0$, and the magnetic skin depth $\delta^*_m = \sqrt{2/(\mu^*_p \sigma^* \omega^*_{\text{ext}})} \to \infty$, thus ω^*_{ext} and f^*_{ext} is not important in this benchmark.

[2] Note the solenoid is not at the center of the computational domain in Figure B.2. Opera automatically centers the computational domain on the conductor. In fact, Opera computes $\mathbf{B}^*$ field values at each finite element node based on the solenoid(s) arrangement. In this benchmark, these $\mathbf{B}^*$ field values are independent of the computational domain size. The solenoid(s) itself does not need to be discretized with a finite element mesh. In Subsection 4.1.1 it is demonstrated that solenoids may be located outside of the computational domain.

[3] by choosing the "Tangential magnetic" option in Opera

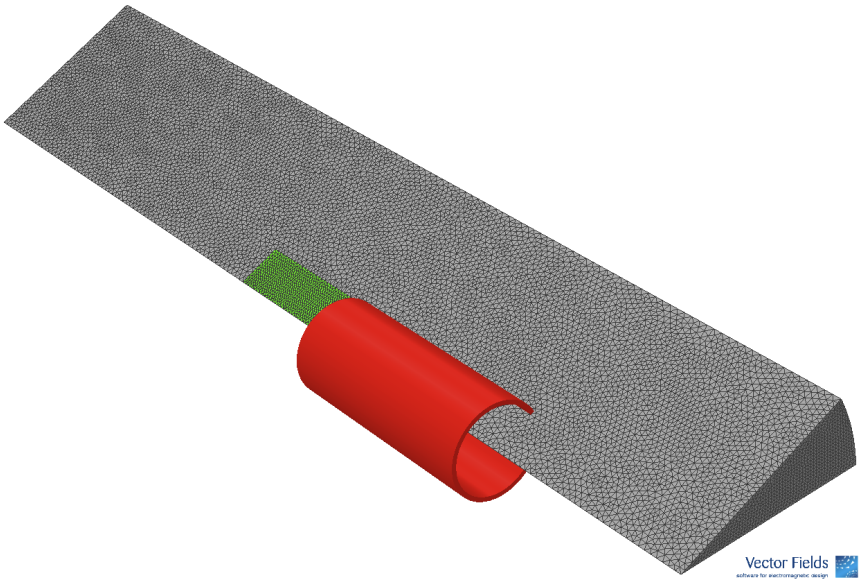

Figure B.2 : Model with finite element meshes of a thin solenoid with finite length in Opera (red tube: solenoid with aspect ratio $L^*/R^* = 5$, green wedge: $1/16^{\text{th}}$ wedge of a cylindrical "air conductor" (properties set to air), large gray wedge: $1/16^{\text{th}}$ wedge of the air domain (the computational domain))

tion in cylindrical coordinates. Following [Callaghan and Maslen, 1960], with the origin at the center of the solenoid, the axial magnetic flux density B_z^* is nondimensionalized as $B_z = 4B_z^*/(\mu_p^* j_L^*)$, where μ_p^* is the permeability and j_L^* is the electric current density per unit length of the solenoid (ampere per meter). The radial magnetic flux density B_r^* is nondimensionalized as $B_r = 4B_r^*/(\mu_p^* j_L^*)$. The nondimensional axial location is $z = 2z^*/L^*$, where $z^* = 0$ is at the half-length of the solenoid. One end of the solenoid is at $z^* = L^*/2$. The radial location r^* is nondimensionalized as $r = r^*/R^*$. The axial and radial components of the magnetic flux density are compared in Figure B.3 and B.4, respectively. The azimuthal component B_θ is exactly zero.

Figure B.3 summarizes the axial magnetic flux density B_z at some discrete locations

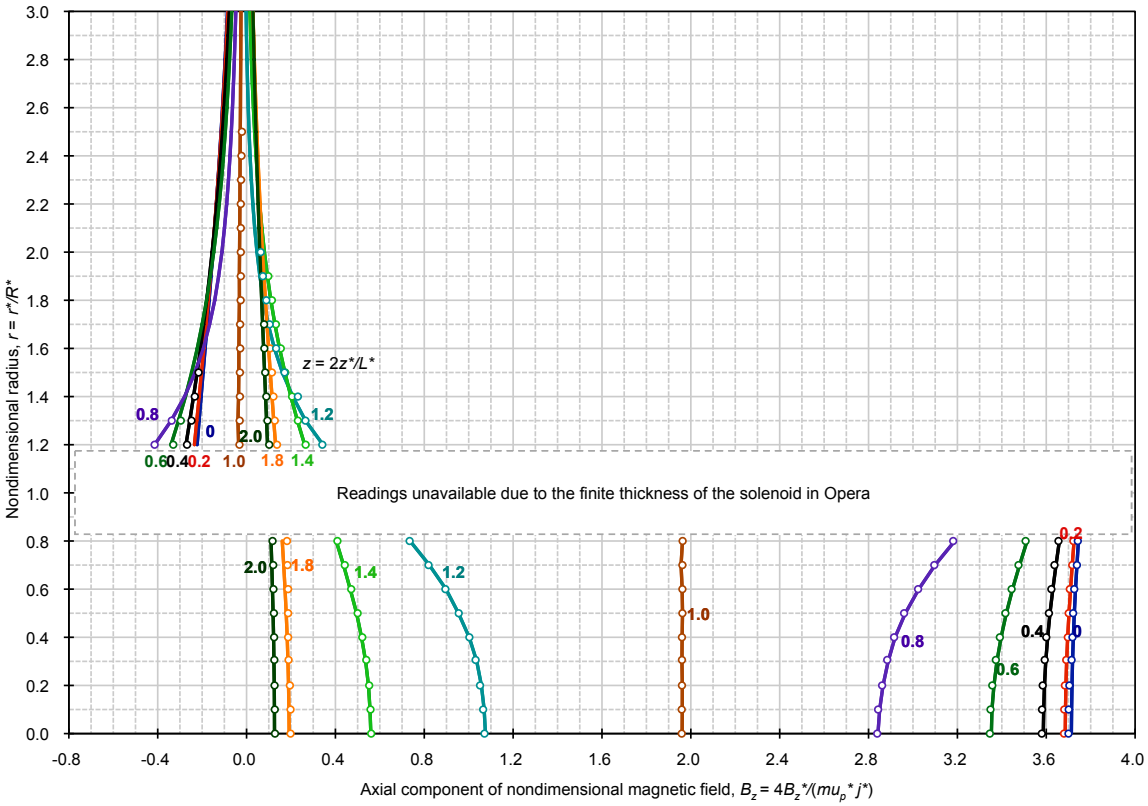

Figure B.3 : Axial magnetic flux density of a thin solenoid with finite length (Lines: simulation results in Opera, open circles: analytical solutions of an infinitely thin solenoid [Callaghan and Maslen, 1960]. Numeral labels are nondimensional axial position $z = 2z^*/L^*$, solenoid aspect ratio $L^*/R^* = 5$)

within $r \in [0, 3]$ and $z \in [0, 2]$. To read the B_z value at point (r, z), first find the curve for the z. Then, on this curve, locate the radial position r on the vertical axis. The value of B_z is then given by the horizontal axis. The B_z values within the radius of the solenoid ($r < 1$) are positive and generally taper off in strength when moving from outside to inside the solenoid. The region $z < 1$ and $r < 1$ is inside the solenoid cylinder, where B_z is strongest (curves in the lower right corners). Curves in the region $r > 1$ and $z > 1$ exhibit negative B_z values, which correspond to magnetic flux

density lines in the $-z$ direction outside of the solenoid, where the fields are weaker than inside the solenoid.

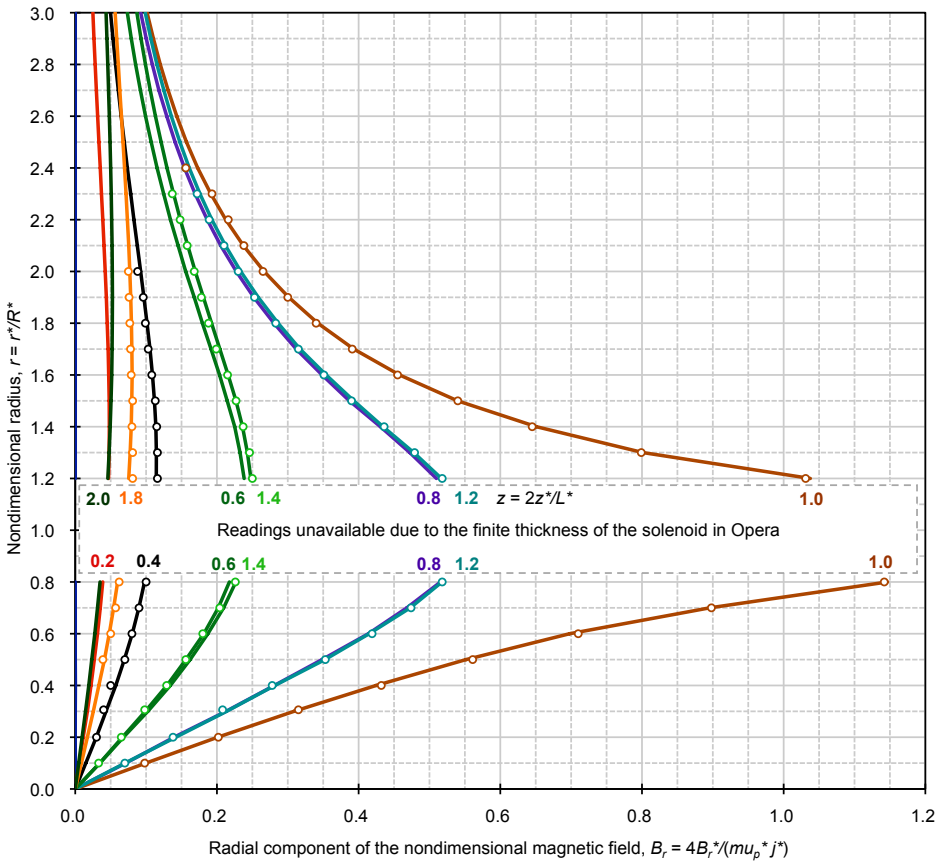

Figure B.4 : Radial magnetic flux density of a thin solenoid with finite length (Lines: simulation results in Opera, open circles: analytical solutions of an infinitely thin solenoid [Callaghan and Maslen, 1960]. Numeral labels are nondimensional axial position $z = 2z^*/L^*$, solenoid aspect ratio $L^*/R^* = 5$)

Figure B.4 summarizes the radial magnetic flux density B_r at some discrete locations within $r \in [0, 3]$ and $z \in [0, 2]$. B_r is strongest near the edge at the end of the solenoid ($r = 1$ and $z = 1$), and weakens when moving in any direction away from this edge. B_r is always positive (pointing outward). Agreement between the

computational simulations and analytical solutions is excellent for both B_r and B_z.

Finally, B_z on the axis ($r^* = 0$) is plotted in Figure B.5 to ensure that the "air conductor" (conductor with properties set to those of air) has no impact on the magnetic flux density. The B_z value in the "air conductor" (the green curve) agrees very well with the analytical solution in the air (open circles). In addition, no induced electric current is observed within the "air conductor" (not shown here). Therefore, the "air conductor" acts like air, which does not change the magnetic flux density as desired. In Chapter 4, "air conductors" are used to fill air space surrounding the actual conductor and control the finite element mesh arrangement.

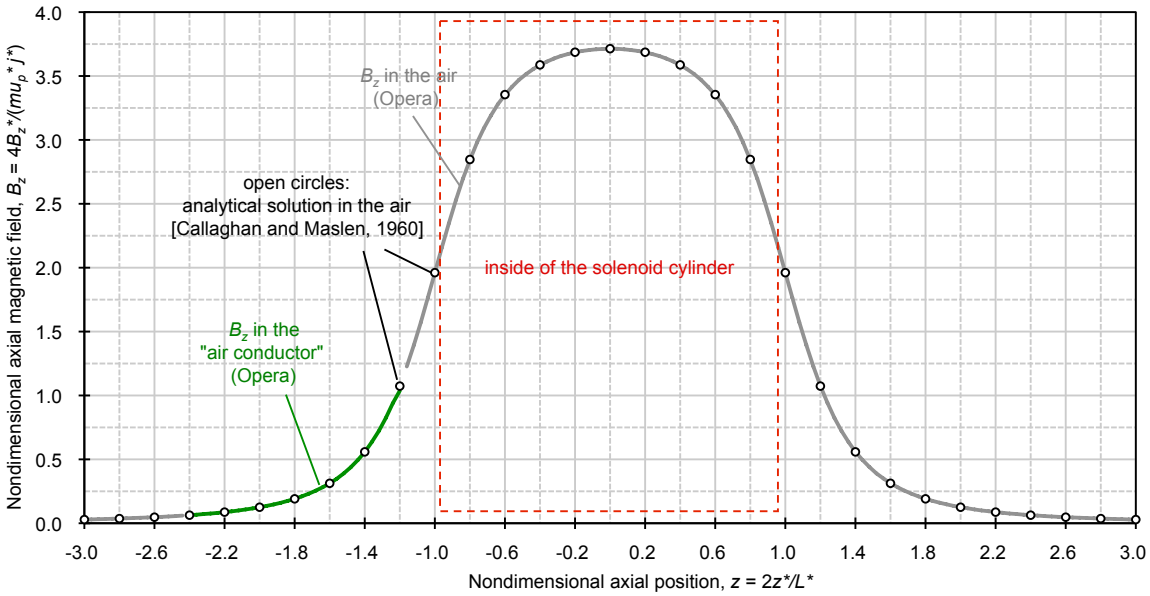

Figure B.5 : Axial magnetic flux density B_z on the axis ($r^* = 0$) of a thin solenoid with finite length (lines: simulation results in Opera, open circles: analytical solutions of an infinitely thin solenoid [Callaghan and Maslen, 1960], solenoid aspect ratio $L^*/R^* = 5$)

In summary, Opera simulations for a thin but finite solenoid demonstrate excellent agreement with analytical solutions for an infinitely-thin solenoid.

B.2 Magnetic Field of a Thick Solenoid with Finite Length

For solenoids with finite thickness, analytical solutions of their magnetic fields have been derived, for example, in [Brown et al., 1963]. This section compares the $\mathbf{B}^*$ field of a thick solenoid predicted in Opera (Figure B.6) and its analytical solution. If not specified explicitly, most discussions on a thin solenoid in Section B.1 apply to the thick solenoid in this section too.

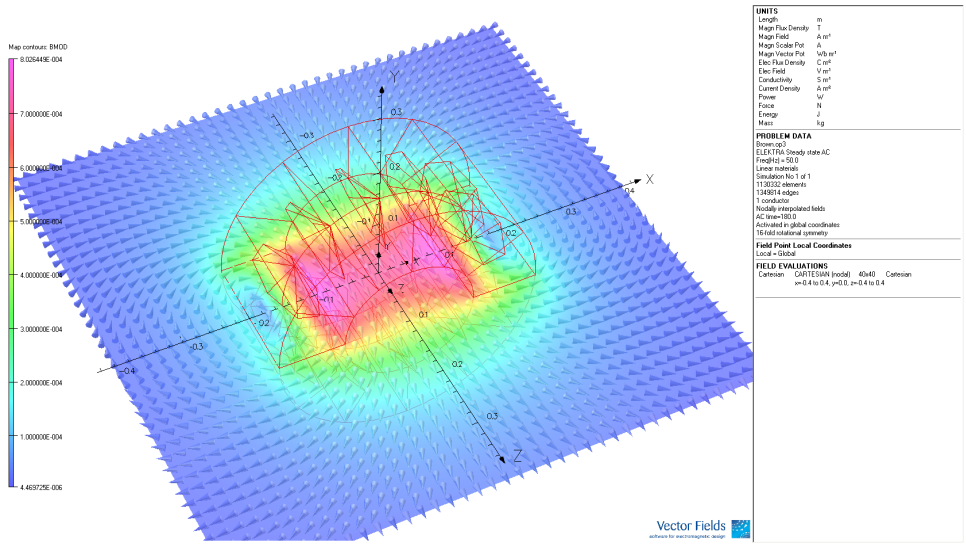

Figure B.6 : Magnetic field on a cutting plane generated by a thick solenoid with finite length simulated in Opera. The solenoid is shown as the red cylinder framework. The magnetic field $\mathbf{B}^*$ on the cutting plane is shown by vectors (direction) and colors maps (magnitude). The computational domain is larger than the cutting plane.

A short and thick solenoid is chosen for benchmark to differentiate it from the geometry in Section B.1. The length of the solenoid is $L^* = 0.2$ m. Inner and outer radii are $R^*_{\text{in}} = 0.1$ m and $R^*_{\text{out}} = 0.2$ m, respectively. The peak electric current density is $j^* = 10,000$ A/m^2 with the alternating frequency of 50 Hz. The surrounding media

is air. The entire computational domain is a $1/16^{\text{th}}$ wedge of a cylinder (radius 1 m and length 0.9 m).

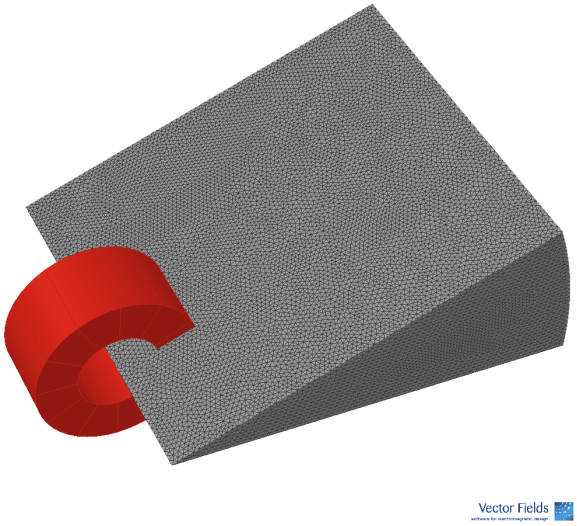

Figure B.7 : Model with finite element meshes of a thick solenoid with finite length in Opera (red ring: solenoid, large gray wedge: $1/16^{\text{th}}$ wedge of the air domain *i.e.* the computational domain)

B_z^* and B_r^* are nondimensionalized by dividing a B_0^* which is the magnetic flux density at the center $(r^*, z^*) = (0, 0)$ of the solenoid. The radial position r^* is nondimensionalized as $r = r^*/R_{\text{in}}^*$. The axial position z^* is nondimensionalized as $z = 2z^*/L^*$.

In the simulation, $B_0^* = 7.0668 \times 10^{-4}$ Tesla at the peak electric current density $j^* = 10,000$ A/m^2. It agrees well with the theoretical prediction of $B_0^* = 0.562261 \times \mu_p^* j^* R_{\text{in}}^* = 7.0656 \times 10^{-4}$ Tesla (Table V in [Brown et al., 1963]).

Figure B.8 summaries the axial magnetic field B_z at discretized locations within $r \in [0, 6]$ and $z \in [0, 2]$. Similar to the B_z of a thin solenoid, B_z is stronger inside of the solenoid than outside. B_z is strongest in the "mid-plane" of the solenoid, especially

close to the inner radius. It weakens when moving away from this "mid-plane" to larger z locations. Outside of the outer radius R^*_{out}, these negative B_z values correspond to magnetic flux lines circulating back in the opposite direction to form closed loops.

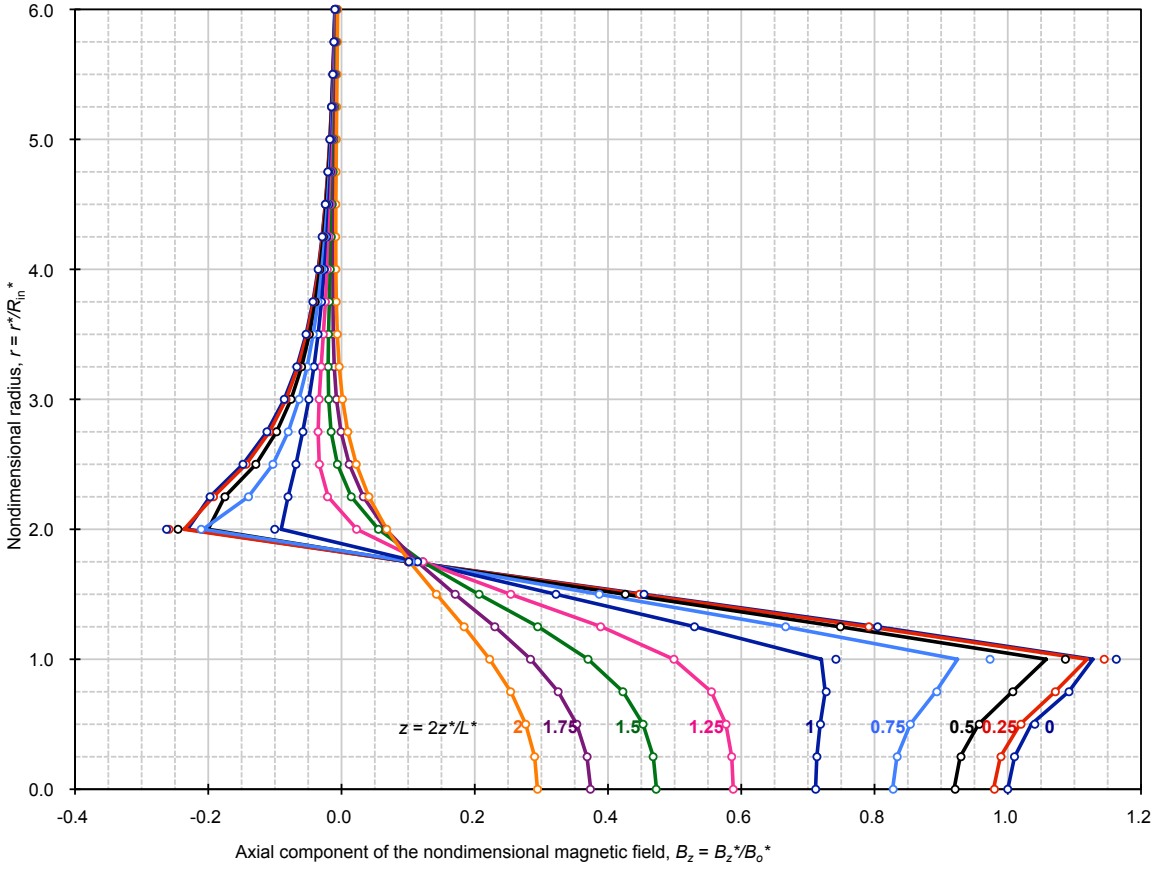

Figure B.8 : Axial magnetic field of a thick solenoid with finite length (Lines: simulation results in Opera, open circles: analytical solutions from [Brown et al., 1963]. Numeral labels are nondimensional axial position $z = 2z^*/L^*$.)

Figure B.9 summaries radial magnetic field B_r at discretized locations within $r \in [0, 6]$ and $z \in [0, 2]$. B_r is strongest near the end ($z = 1$) of the solenoid. It weakens if moving away in any direction. $B_r \equiv 0$ in the "mid-plane" ($z = 0$) of the solenoid.

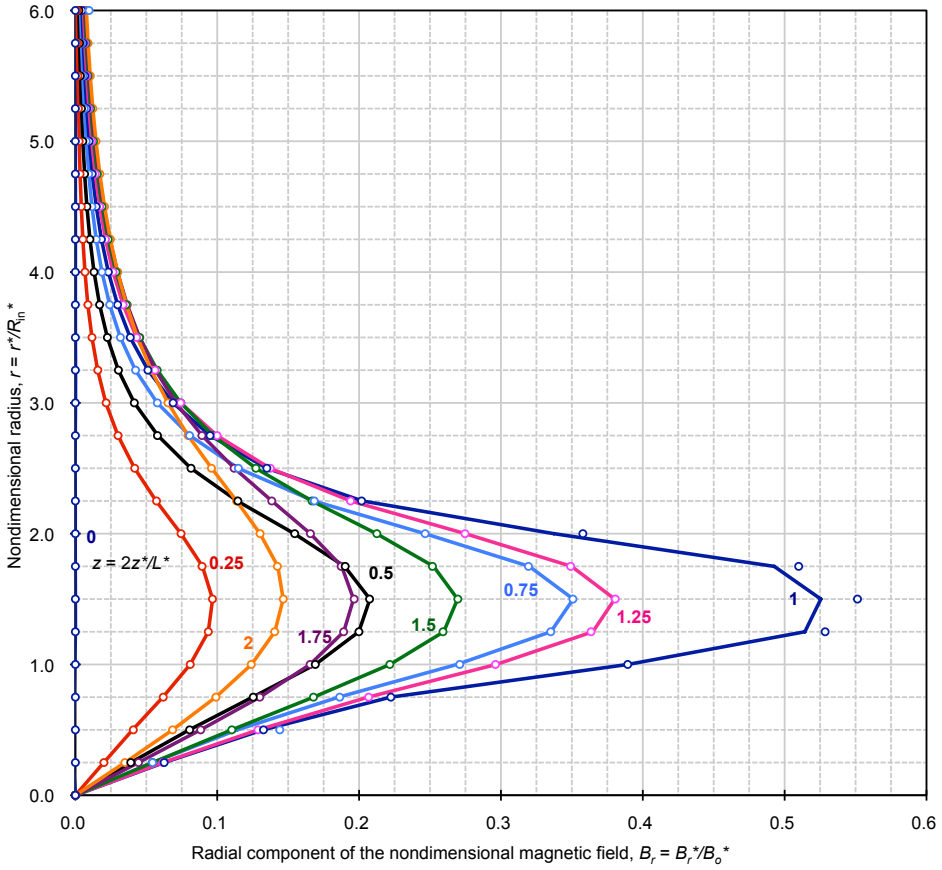

Figure B.9 : Radial magnetic field of a thick solenoid with finite length (Lines: simulation results in Opera, open circles: analytical solutions from [Brown et al., 1963]. Numeral labels are nondimensional axial position $z = 2z^*/L^*$.)

Please notice that the region $1 \leq r \leq 2$ and $z \leq 1$ is within the cross-sectional area of the solenoid. On the solenoid surface (*i.e.* $r = 1$, $r = 2$, and $z = 1$), several data points from Opera deviate noticeably from the analytical solution in Figure s B.8 and B.9. This may be due to the way Opera interprets values at the interface, or numerical error from meshing. However, this discrepancy is less of a concern in this work, because solenoids are only used to generate the desired magnetic field. The focus is not inside or on the surface of solenoids. Overall, Figures B.8 and B.9 show

that Opera predicts the magnetic field very well in the area surrounding the thick solenoid.

B.3 Magnetic Field of a Pair of Thick Solenoids with Finite Length

This section verifies superposition of magnetic fields generated by multiple solenoids. The $\mathbf{B}^*$ field of a pair of thick solenoids predicted in Opera (Figure B.10) is compared with its analytical solution calculated from [Brown et al., 1963].

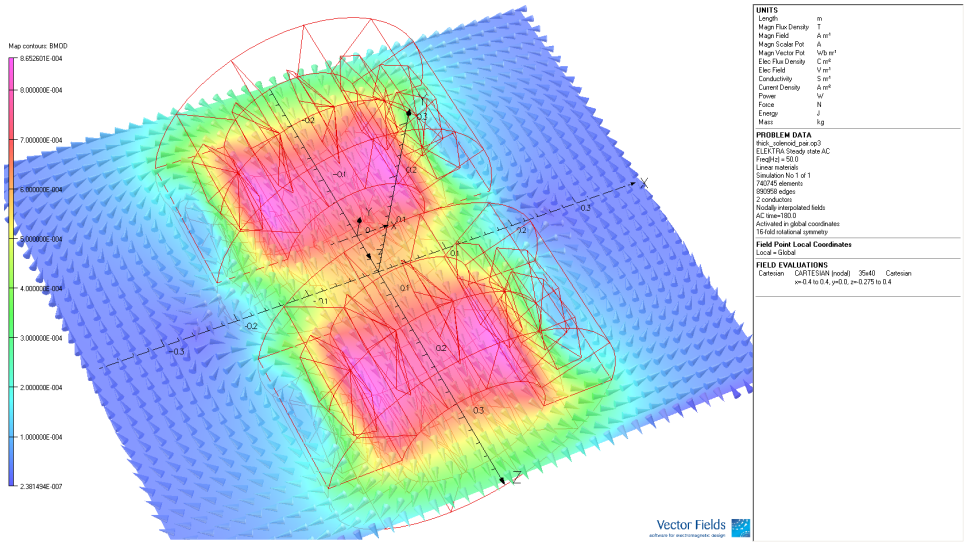

Figure B.10 : Magnetic field on a cutting plane generated by a pair of thick solenoids with finite length simulated in Opera. Solenoids are shown as red cylinder frameworks. The magnetic field $\mathbf{B}^*$ on the cutting plane is shown by vectors (direction) and colors maps (magnitude). The computational domain is larger than the cutting plane.

As shown in Figure B.10, a pair of solenoids identical to the one in Section B.2 is aligned by their axial axes and separated by a distance of 0.12 m. Their AC cycles

are synchronized (*i.e.* no phase shift). The length of each solenoid is $L^* = 0.2$ m. Inner and outer radii are $R^*_{\text{in}} = 0.1$ m and $R^*_{\text{out}} = 0.2$ m, respectively. The maximum electric current density is 10,000 A/m^2 with the alternating frequency of 50 Hz. The surrounding media is air. The entire computational domain is a 1/16$^{\text{th}}$ wedge of a cylinder (radius 0.7 m and length 1 m).

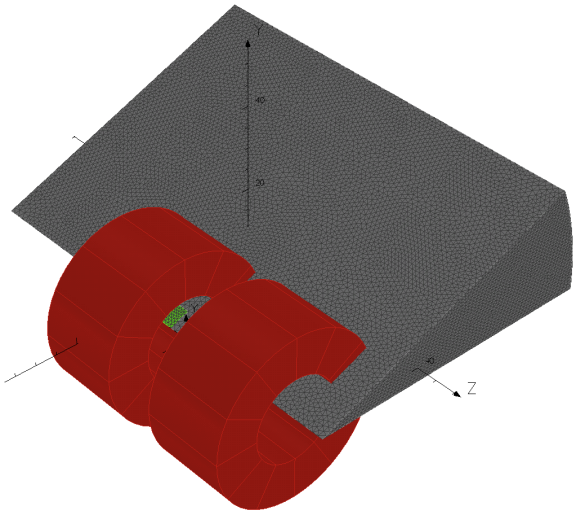

Figure B.11 : Model with finite element meshes of a pair of thick solenoids with finite length in Opera (red rings: solenoids, small red wedge: 1/16$^{\text{th}}$ wedge of the "air conductor", large gray wedge: 1/16$^{\text{th}}$ wedge of the air domain, *i.e.* the computational domain. The length unit is centimeter in this figure.)

B^*_z and B^*_r are nondimensionalized by dividing a B^*_0, which is the magnetic flux density at the center of one single solenoid (as if the other solenoid did not present) – same as B^*_0 in Section B.2. The origin of the cylindrical coordinate system is shown in Figure B.10 (at the end of one solenoid facing the other solenoid, and on the common axis of both solenoids). The radial position r^* is nondimensionalized as $r = r^*/R^*_{\text{in}}$. The axial position z^* is nondimensionalized as $z = 2z^*/L^*$.

Figure B.12 summaries the axial magnetic field B_z at discretized locations between two solenoids. The gap between two solenoids is 1.25 nondimensional unit length. $z = 0.25$ is at $1/5^{\text{th}}$ of the distance from one solenoid to the other. $z = 0.5$ is at $2/5^{\text{th}}$ of the distance from one solenoid to the other. Due to the symmetry, B_z at $z = 0.75$ is the same as B_z at $z = 0.5$, and B_z at $z = 1$ is the same as B_z at $z = 0.25$. B_z is strongest near the common axis (*i.e.* $r = 0$). It weakens quickly when moving away from the axis. Further away ($r > 2.5$), B_z is negative due to magnetic flux lines circulating back in the opposite direction to form closed loops. B_z is slightly stronger closer to the solenoid ($z = 0.25$) than closer to the middle of the gap between two solenoids ($z = 0.5$).

Figure B.13 summaries the radial magnetic field B_r at discretized locations between two solenoids. B_r is strongest between the inner and outer radius ($1 < r < 2$) of the solenoid. It weakens if moving away in any direction. B_r is stronger closer to the solenoid ($z = 0.25$) than closer to the middle of the gap between two solenoids ($z = 0.5$). Overall, Figures B.12 and B.13 show that Opera predicts the magnetic field very well in the area between the solenoid pair.

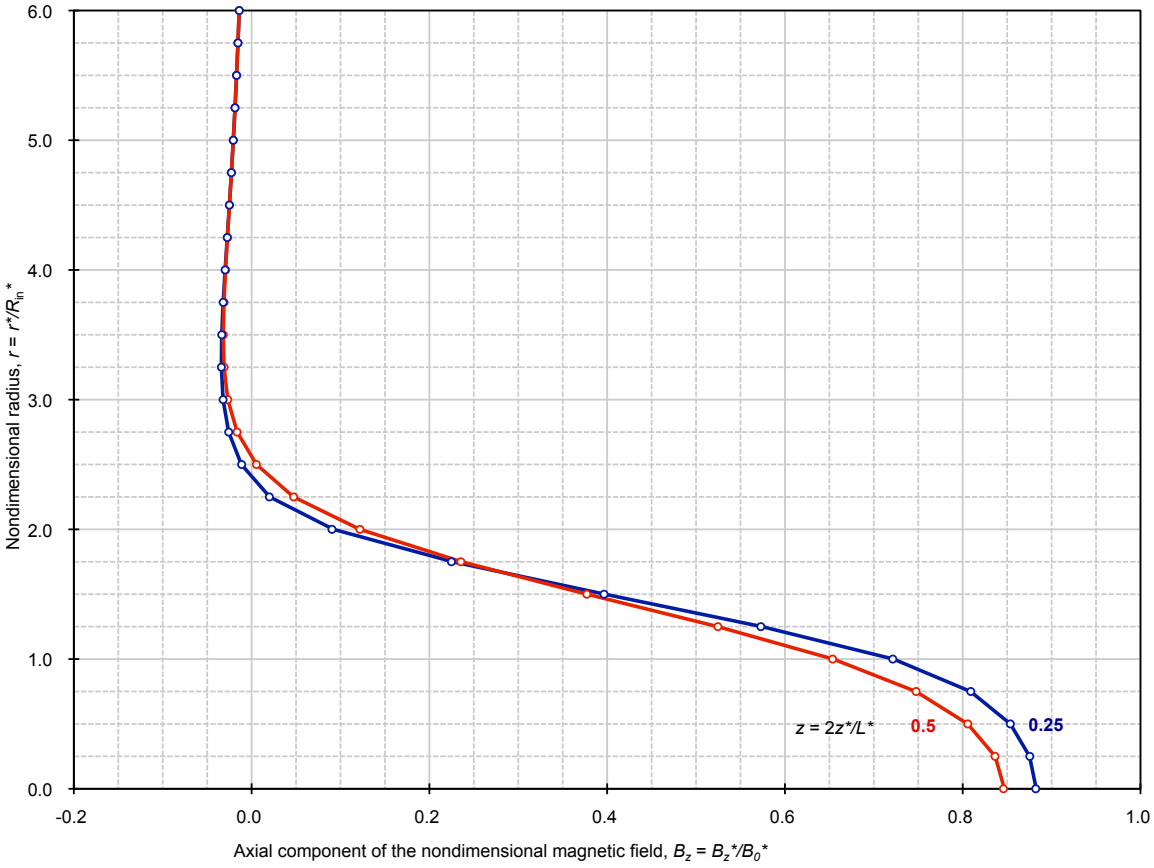

Figure B.12 : Axial magnetic field of a pair of thick solenoids with finite length (Lines: simulation results in Opera, open circles: analytical solutions calculated from [Brown et al., 1963]. Numeral labels are nondimensional axial position $z = 2z^*/L^*$.)

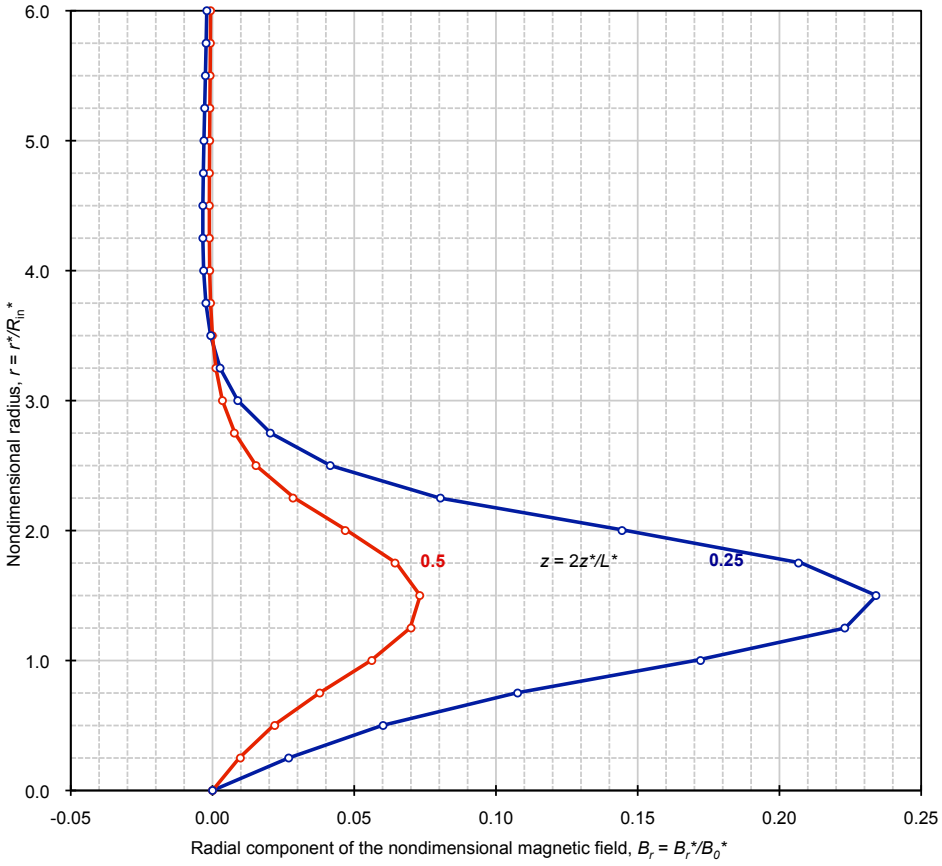

Figure B.13 : Radial magnetic field of a pair of thick solenoids with finite length (Lines: simulation results in Opera, open circles: analytical solutions calculated from [Brown et al., 1963]. Numeral labels are nondimensional axial position $z = 2z^*/L^*$.)

Nomenclature

* Quantities with an asterisk superscript are dimensional. Quantities without an asterisk superscript are nondimensional, page 24

α regularization coefficient in the regularization function $F(z)$, page 46

α^* thermal diffusivity, page 43

$\mathbf{B}^*$ magnetic flux density, page 24

$\mathbf{B}^*_{\text{ext}}$ external magnetic flux density, page 29

$\mathbf{F}^*_{\text{EM}}$ and $F^*_{\text{EM},r}$, $F^*_{\text{EM},\theta}$, $F^*_{\text{EM},z}$ electromagnetic body force, page 25

$\mathbf{j}$ electric current density, page 25

$\mathbf{v}$ and v_r, v_θ, v_z velocity, page 25

δ^*_m magnetic skin depth, page 31

γ^* surface tension, page 44

$\lambda = \lambda_r + i\lambda_i$ eigenvalue in normal mode linear stability analysis of liquid bridge, page 81

λ^* magnetic diffusivity, $\lambda^* = 1/(\mu^*_p \sigma^*)$, page 27

$\langle\ \rangle$ time-averaged value, page 123

$\mathcal{A}_{LM}, \mathcal{B}_{LM}, \mathcal{C}_{LM}, \mathcal{D}_{LM}$ Chebyshev polynomial coefficients for v_{r1}, v_{z1}, T_1 and ϕ_1, respectively, page 79

μ^* dynamic viscosity, page 35

μ_p^* magnetic permeability, page 25

ν^* kinematic viscosity, page 41

ω_{ext}^* angular frequency of the external alternating magnetic field, $\omega_{\text{ext}}^* = 2\pi f_{\text{ext}}^*$, page 29

ω_θ azimuthal vorticity, page 49

ϕ electric potential, page 42

ψ stream function, page 47

ψ_θ^* meridional flow stream function, page 134

ρ^* density, page 35

σ^* electrical conductivity, page 25

$\tau_{r\theta}$, τ_{rz} shear stresses, page 43

$_0$ Variables with subscript 0 are for base flow, page 74

$_1$ Variables with subscript 1 are for instabilities, page 74

A_{LM}, B_{LM}, C_{LM} Chebyshev polynomials coefficients for ψ, ω_θ and T_0, respectively, page 50

b aspect ratio of the melt, page 40

c_p^* specific heat, page 35

$F(z)$ regularization function (to remove vorticity singularity in the liquid bridge), page 46

f_{ext}^* AC frequency, *i.e.* the alternating frequency of the external magnetic field, $f_{\text{ext}}^* = f_{\text{ext}}^*/(2\pi)$, page 29

Ha Hartmann number, page 33

k^* thermal conductivity, page 35

m azimuthal wave number of perturbations, page 75

m_{cr} critical azimuthal wave number of perturbations, page 75

Ma Marangoni number, page 43

NR, NZ Gauss-Lobatto collocation grid points in linear stability analysis of liquid bridge, page 78

NRF, NZF, NRT, NZT Gauss-Lobatto collocation grid points for the base flow of liquid bridge, page 51

P pressure, page 31

Pr Prandtl number, page 43

q^* lateral maximum heat flux onto the liquid bridge, page 40

r, θ, z cylindrical coordinates, page 41

R^* radius of the melt, page 40

R_ω magnetic shielding parameter, page 29

R_m magnetic Reynolds number, page 27

Re_{classic} classic viscous Reynolds number based on the characteristic viscous velocity $V_0^* = \mu^*/(\rho^* L_0^*)$, page 32

Re_{viscous} viscous Reynolds number based on the maximum nondimensionalized flow velocity $v_{\max}$, page 67

$Re_{FZ,cr}$ critical thermocapillary Reynolds number for Full-Zone liquid bridge, page 82

Re_{FZ} thermocapillary Reynolds number in Full-Zone liquid bridge, page 43

Re_{HZ} thermocapillary Reynolds number in Half-Zone liquid bridge, page 91

T temperature, page 35

t time, page 25

T_0^* melting temperature of the crystal material, page 40

$T_n(x)$ Chebyshev function of the first kind, page 48

Ta_m magnetic Taylor number, page 35

$\hat{\mathbf{e}}_r, \hat{\mathbf{e}}_\theta, \hat{\mathbf{e}}_z$ cylindrical unit vectors, page 42